UNIVERSITY OF MISKOLC FACULTY OF MATERIALS AND CHEMICAL ENGINEERING

University of Miskolc

Faculty of Materials Science and Engineering

Institute of Physical Metallurgy, Metal Forming, and Nanotechnology

Antal Kerpely Doctoral School

Effect of Eutectic Front Velocity, Solid/Liquid front velocity, and Forced melt flow Induced by RMF on the Solidified Microstructure of Al-Si Alloys

Ph.D. Dissertation

Submitted by Dimah Zakaraia

Supervisor: Dr. Veres Zsolt

(Associate Professor)

2025

Declaration

The author hereby declares that this thesis has not been submitted, either in the same or in a different form, to this or to any other university for obtaining a PhD degree. The author confirms that the submitted work is her own and the appropriate credit has been given where reference has been addressed to the work of others.

Dimah Zakaraia

Acknowledgment

I am deeply grateful to Allah, whose countless blessings granted me the strength and perseverance to complete this work. I extend my sincere appreciation to my supervisors, Dr. Zsolt Veres and Prof. András Rősz, for their exceptional guidance, support, and insightful feedback. I am also thankful to Dr. Arnold Rőnafoldi for his valuable assistance during the experimental phase.

This thesis is dedicated to the soul of my beloved father, whose encouragement and belief in me were constant sources of motivation. His passing this year has left a great void, and I offer this work as a humble gift to his memory.

My deepest thanks go to my mother, whose love, strength, and sacrifices have been my foundation. Her prayers and unwavering support made this journey possible.

I am especially grateful to my husband, my greatest supporter and companion. His patience, encouragement, and steadfast presence helped me through every challenge. I also thank his family, especially his mother, for their kindness and support.

To my entire family, particularly my brothers and sisters, thank you for your love and belief in me. Your encouragement has meant so much.

A special thanks goes to my little son, whose smile and presence brought light and strength to my days. He has been a true inspiration throughout this journey.

Finally, I am thankful to all who contributed in any way to the completion of this work. Your support is deeply appreciated.

Table of contents

1. Introduction

Aluminium-silicon (Al-Si) alloys are widely used in various engineering applications due to their excellent properties, such as low density, good mechanical properties, high thermal conductivity, and good corrosion resistance [1]. Al-Si alloys containing more than 12.6wt% Si have hypereutectic microstructures composed of primary Si in an Al-Si eutectic matrix [2]. Hypereutectic Al-Si alloys have gained significant attention in the industrial sector due to their excellent combination of high strength, wear resistance, and thermal stability. However, their microstructure is complex, irregular, and heterogeneous, which affects their mechanical properties.

Hard primary Si particles and long eutectic Si lamellas give hypereutectic Al-Si alloys high strength and wear resistance. On the other hand, it leads to low ductility and poor machining qualities of these alloys, severely limiting their application in promising sectors [3]. In addition, the long eutectic Si lamellas and large primary Si blocks act as a stress concentration point for cracks, making these alloys suffer from brittleness and are easy to fracture [4]. The microstructure of these alloys strongly influences their mechanical properties, and thus, controlling their microstructure is essential for achieving the desired mechanical properties. One of the most common methods to improve the microstructure and properties of these alloys is to alter the solidification conditions, such as by controlling the eutectic front velocity and the solid/liquid (s/l) primary Si front velocity or applying melt conditioning methods, such as inducing the melt using a rotating magnetic field (RMF). This research dissertation will deal with the effect of forced melt flow by RMF, eutectic front velocity, and s/l front velocity on the microstructure of hypereutectic Al-18 wt.% Si alloy.

In hypereutectic Al-Si alloys, the growth of primary Si particles and eutectic lamellas with varied shapes, sizes, and orientations make the microstructure characterization and measurement of these alloys a big challenge in solidification. This thesis introduces innovative methods for accurately characterizing the length and morphology of primary Si particles. Furthermore, it presents the impact of forced melt flow using RMF and s/l front velocity on the length, morphology, and distribution of primary Si in hypereutectic Al-18 wt.% Si alloy. Additionally, the study presents the impact of RMF and eutectic front velocity on the length, interlamellar distances, and angular orientation of eutectic Si lamellas.

1.1. Scope

The main aims of this study are:

- Present a comprehensive characterization study of primary Si in hypereutectic Al-18 wt.% Si alloy. Our work sheds light on the size, distribution, and morphology of primary Si. This characterization study will enhance our comprehension of how RMF and s/l front velocity impact the microstructural scale.
- Investigate the effect of forced melt flow by an RMF and s/l front velocity on the size, morphology, and distribution of primary Si in a hypereutectic Al-18 wt.% Si alloy.
- Investigate the effect of forced melt flow by an RMF and eutectic front velocity on the length, orientation angles from the solidification direction, and interlamellar distances of eutectic Si lamellas in a hypereutectic Al-18 wt.% Si alloy.
- Investigate the macro-segregation patterns that develop during the unidirectional solidification of hypereutectic Al-18 wt.% Si alloy, considering the effects of RMF and s/l front velocity.

1.2. Outline of the Thesis

This dissertation is structured into nine chapters, each focusing on a specific aspect of the PhD research.

- **Chapter 1** introduces the research problem and defines the scope of the dissertation.
- **Chapter 2** provides a comprehensive literature review, covering background information on Al-Si alloys, particularly hypereutectic Al-Si alloys, their microstructural evolution, and the nucleation and growth of primary Si and eutectic structures. Additionally, it presents an overview about forced melt flow induced by a RMF and the effect of eutectic and s/l front velocities and RMF on solidification of alloys.
- **Chapter 3** details the experimental work conducted by our research group, including the solidification facility, alloy selection, experiment design, and sample preparation.
- **Chapter 4** describes the measurement and characterization methods used in the study.
- **Chapter 5** presents the results and provides an in-depth discussion of the underlying phenomena.

- **Chapter 6** highlights the dissertation's key contributions to the field and outlines its core claims.
- **Chapters 7, 8, and 9** include Author's Publications, references, and appendix.

2. Literature Review

2.1. Aluminium-Silicon (Al-Si) Alloys

Aluminium castings have become increasingly popular during the past decades, especially in the transportation and aerospace sectors [5]. Al-Si alloys are the most crucial among aluminium casting alloys due to their superior casting properties, high corrosion resistance, good weldability, and the fact that adding silicon as a main alloying element to aluminium improves the fluidity of the melt and reduces the coefficient of thermal expansion and reduces the melting temperature [6], [7]. The Al-Si binary alloy is a eutectic system, and its eutectic composition and temperature have been determined to be 12.6 wt % Si and 577 C, respectively (**Figure 1)**. The intersection of the eutectic temperature and the eutectic composition gives the eutectic point. When the molten Al-Si alloy begins to solidify, the primary phases, like primary aluminium or primary silicon, form first and grow in different shapes depending on the weight percentage of the silicon in the alloy and the solidification parameters. As solidification progresses to the eutectic temperature, the eutectic Al-Si forms, and the Si grows in a plate-like shape, which may change as a result of modification treatment [8]. At the eutectic temperature, silicon can be dissolved in fcc aluminium to a small but noticeable extent of up to 1.6 wt.% Si. In contrast, the solubility of aluminium in silicon is negligible. The industrial Al-Si alloys, in their as-cast form, can be categorized into the following classes [9]:

- Hypoeutectic alloys, the silicon content in these alloys is less than 12.6 wt.%. It is common for hypoeutectic alloys to have a soft and ductile primary aluminium phase and a hard eutectic silicon phase.
- Eutectic alloys, the silicon content in these alloys equals 12.6 wt.%. In these alloys, the eutectic phase is the dominant microstructural phase.
- Hypereutectic alloys, the silicon content in these alloys is higher than 12.6 wt.%. It is common for hypereutectic alloys to have coarse primary silicon particles in the eutectic matrix.

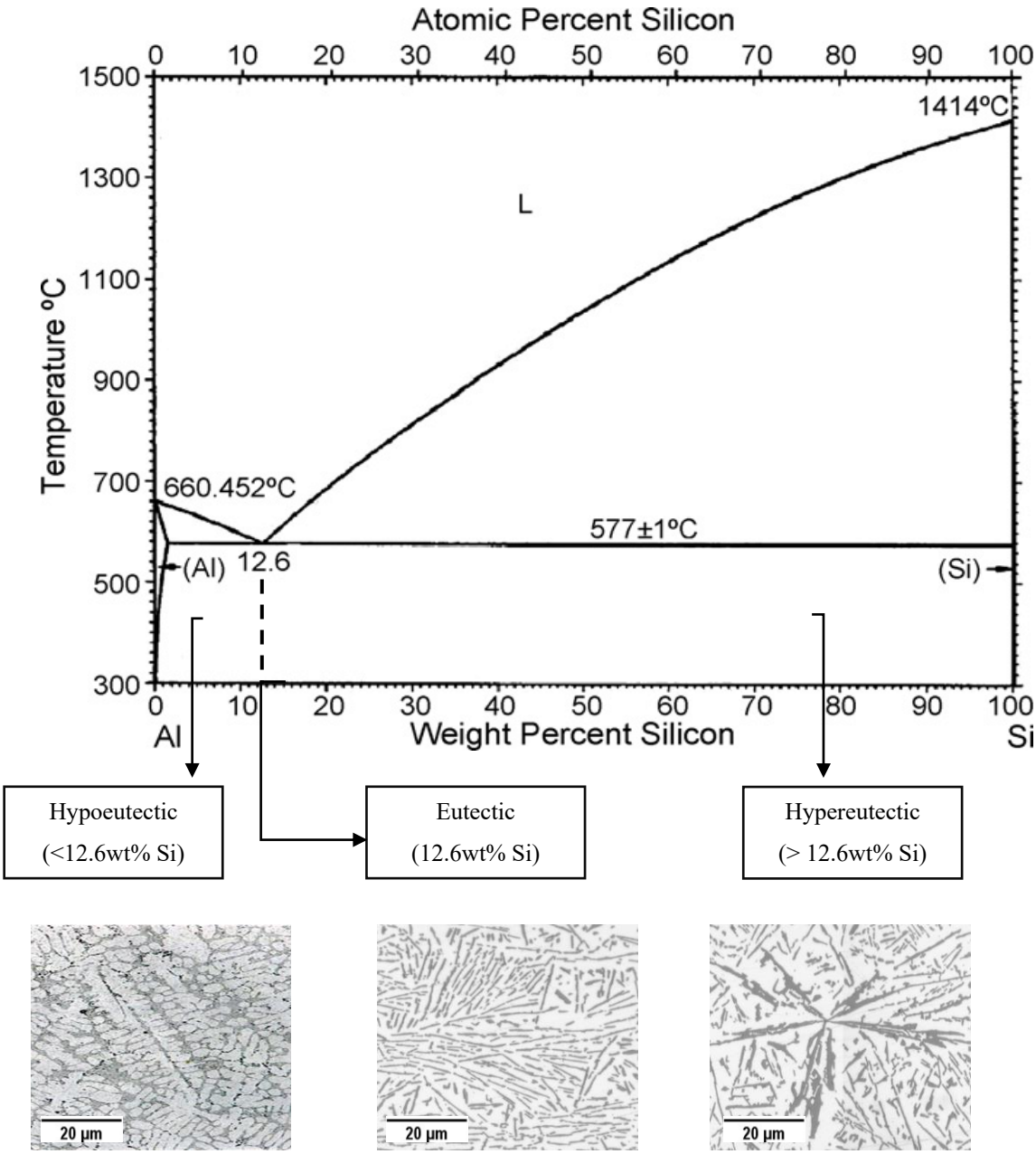

Figure 1. Phase diagram of Al-Si alloys and the microstructure of hypoeutectic, eutectic, and hypereutectic alloys.

2.2. Hypereutectic Al-Si Alloys

More than 50 years ago, hypereutectic Al-Si alloys were used to cast engines, compressors, pumps, pistons, cylinders, bearings, and other analogous wear applications and are still used increasingly for this purpose and several other applications until now [2], [10], [11].

Hypereutectic Al-Si alloys share excellent features. These include low thermal expansion, high wear and corrosion resistance, low specific gravity, lightweight, and high thermal conductivity. In addition, these alloys perform exceptionally well in high-temperature applications. Young's modulus of the hypereutectic alloy is higher than conventional aluminium casting alloys, its strength is higher, its coefficient of thermal expansion is lower, and its wear resistance is bigger [2]. These alloys are widely employed in aerospace, shipbuilding, automotive, and other industries [3]. The most common commercial Hypereutectic Al-Si alloys are [2]:

- B390 alloys: contain 16.0-18.0 % Si, and the typical applications for these alloys are engine blocks, pistons, pumps, and compressors.
- 391 (Mercasil) alloys: or as it is known, Mercury Marine's hypereutectic alloys; these alloys contain 18.0-20.0 % Si, and the typical application for these alloys is marine engine blocks.
- 393 (Vanasil) alloys: contain 21.0-23.0 % Si, and the typical application for these alloys is diesel pistons.

The microstructure of hypereutectic alloys contains hard primary Si particles in a eutectic matrix. Depending on the solidification conditions and the chemical composition, the primary Si in these alloys typically appears in different growth morphologies, including polyhedral, star-like, coarse plate, dendritic, fishbone-like, etc [12], [13]. Plate-like primary Si was developed by the action of twin boundaries that seem parallel to flat sides (TPRE), as reported by Fredriksson et al [14]. They hypothesized that the conditions under which polyhedral and star-like crystals typically develop are those in which a new atomic layer can begin to form in many different places on the {111} facets of the crystal. As the supersaturation or cooling rate increases, the growth favours the edges and corners, eventually taking on a dendritic shape. Other researchers mentioned different types of eutectic Si in hypereutectic Al-Si alloys, including flake-like, fibrous, Y-like, or called angular Si, and plate-like [5], [15], [16].

Hard primary Si particles and long eutectic Si lamellas give these alloys high strength and wear resistance. On the other hand, it leads to low ductility and poor machining qualities of these alloys, severely limiting their application in industrial sectors. Refinement of the microstructure of hypereutectic Al-Si alloys is an efficient method for overcoming these drawbacks [17]. Moreover, refining the hypereutectic alloys leads to enhancing the mechanical properties. According to

Tiwari [18], refining the hypereutectic alloys enhanced the hardness and strength and decreased the wear rate of these alloys. Tenekedjiev and Gruzleski reported in their review that changing the morphology, size, and distribution of the primary and eutectic Si leads to a change in the cast alloy's properties. Because of that, controlling them is so needed to produce castings of controlled properties [5].

Several techniques have been employed to refine primary Si, expanding the industrial potential of hypereutectic Al-Si alloys. There have been reports proving that adding elements such as phosphorus [19], strontium [20], scandium [21], and boron [22] during solidification can influence the size of the primary Siparticles. The magnetic field [23], [24], and ultrasonic vibrations [25] also have been shown to be beneficial for refining primary silicon particles. Most of these methods only affect the primary silicon size without affecting the eutectic silicon. Of all these methods, using the magnetic fields during solidification is the most important and effective method for controlling the microstructure of the Al-Si alloys. The machinery is straightforward and doable, even in a lab setting. As the progress of the trial, the melt flow rate and direction can be easily adjusted by adjusting the induction parameters (induction, frequency) [26].

2.3. Microstructural Evolution of Hypereutectic Al-Si Alloys

The microstructural evolution of hypereutectic Al-Si alloys, especially during solidification, is fundamentally influenced by the growth mechanisms of primary Si and the eutectic structure. Understanding these growth processes is essential for controlling the mechanical properties and performance of these alloys in applications. Here, I'll delve into the formation of primary Si and eutectic growth in hypereutectic Al-Si alloys. In hypereutectic Al-Si alloys, the solidification starts with the nucleation and growth of primary Si crystals before the formation of the eutectic structure.

2.3.1. Nucleation of Primary Si

The formation of primary silicon (Si) in hypereutectic Al–Si alloys begins with nucleation, a critical stage that significantly influences the final morphology and distribution of Si particles. Nucleation occurs when the liquid alloy reaches sufficient undercooling below the equilibrium liquidus temperature, allowing stable Si nuclei to form. The ease of nucleation depends on several factors, including the degree of undercooling, the presence of potent nucleating agents (e.g., AlP particles), and the alloy’s thermal history. Heterogeneous nucleation is the predominant

mechanism in Al–Si systems, where nucleation takes place on foreign substrates or container surfaces rather than spontaneously in the melt. Controlling the nucleation rate is vital, as it directly affects the number, size, and uniformity of primary Si particles. An increased nucleation rate typically results in finer and more evenly distributed Si particles, which is beneficial for improving the mechanical properties of the alloy. Once nucleated, these Si particles undergo growth, which is further influenced by the thermal gradient, growth velocity, and alloy composition [27].

2.3.2. Growth of Primary Si

During solidification, silicon particles grow into a wide range of shapes, influenced by the cooling rate and the degree of undercooling. The morphology of the primary Si particles is determined by their nucleation and growth behaviour throughout the solidification process. Unlike aluminium, which grows in a non-directional manner, silicon's growth is orderly due to its diamond cubic crystal structure, leading to a strong tendency to facet on {111} planes. Silicon grows through a mechanism known as the Twin Plane Re-entrant Edge (TPRE) mechanism, where a stable groove on the surface of a twinned crystal promotes rapid growth in the specific direction [112], with a {111} twin plane [6]. TPPRE mechanism means that silicon crystals often form twins (mirror images across planes like {111}), which create re-entrant edges—groove-like corners on the crystal surface. These edges serve as favorable sites for atom attachment, promoting faceted growth with well-defined crystal faces. The primary Si morphologies observed in the cast microstructures of hypereutectic Al-Si alloys are highly varied, and these morphologies change markedly with alterations in growth velocity and thermal gradient. The size and shape of primary Si particles vary based on solidification conditions like cooling rate, impurities present, and the ease of nucleation. This variation in silicon morphology is due to the complexities associated with foundry practices. Additionally, efforts are made to attain specific microstructures by adjusting casting parameters. Primary Si morphologies are classified into six shapes, influenced by casting conditions, including star-like, feathery, polyhedral, dendritic, spheroidal, and plate-like structures [28].

2.3.2.1. Star-like primary Si

Star-like primary Si, exhibiting a unique fivefold symmetry, is typically found in hypereutectic alloys subjected to slow solidification rates or untreated alloys [29]. **Figure 2** presents a representative microstructure of star-like primary Si. This morphology can be classified into three

subtypes: radial star, lamellar star, and solid star [5]. Radial stars have thick, evenly spaced arms radiating symmetrically from a central point. Lamellar stars feature thinner, plate-like arms that may overlap, giving a layered appearance. Solid stars are more compact and denser, with less visible branching, appearing as filled-in or polygonal shapes.

The fivefold star-like silicon particles form from a special type of nucleus called a decahedral nucleus, which consists of five silicon tetrahedra arranged in a twinned configuration. These tetrahedra share a common crystallographic direction—known as the ⟨110⟩ axis—which acts as the central line of symmetry.

As the crystal grows, each branch extends from this nucleus following the Twin Plane Reentrant Edge (TPRE) mechanism. This mechanism relies on a stable 141° groove formed between the twinned crystal planes. This groove acts as a favourable site for nucleation and atom attachment, guiding the growth of each branch and preserving the fivefold symmetry of the particle (**Figure 3a**).

Under perfect conditions, the branch grows until the grooves are completely filled, and growth naturally stops (Fig. 3b). However, in real conditions, the grooves do not fully close (Fig. 3c). Instead, to maintain growth, new re-entrant grooves form on the top surfaces of the growing branches. These grooves preserve the growth geometry and allow the silicon crystal to continue growing along the branch (axially) (Fig. 3d). As a result, fivefold silicon particles can grow in both radial (outward) and axial (along the branch) directions, maintaining their characteristic star-like shape [30].

The growth of these particles is highly dependent on undercooling and solidification rates. Research shows that star-like silicon is more likely to form at lower undercooling levels and transform into massive silicon crystals when undercooling increases beyond a critical value [31].

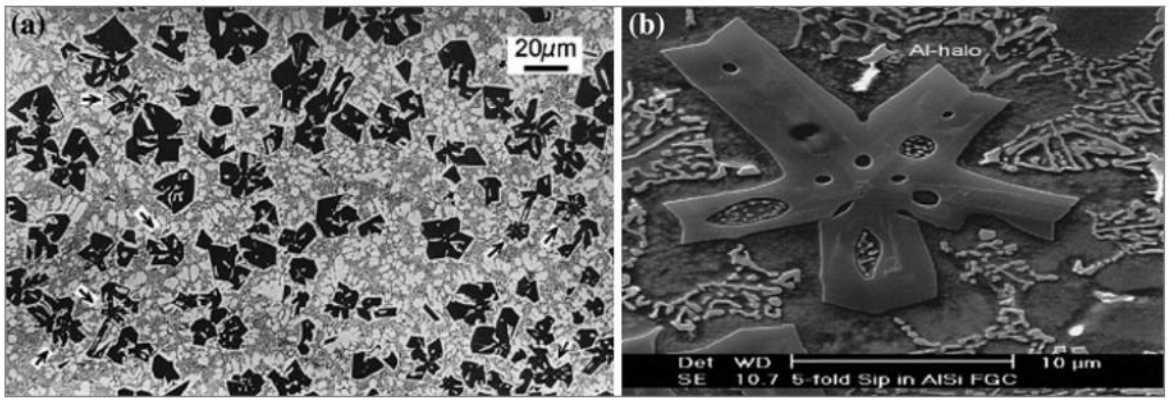

Figure 2. Micrographs displaying star-like primary Si particles [32].

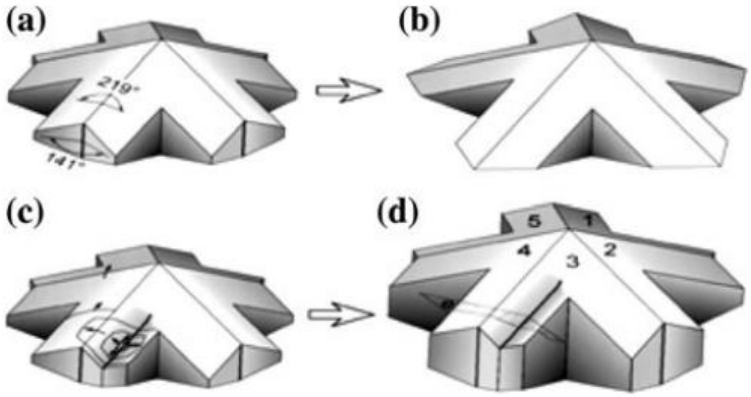

Figure 3. Schematic representation of the fivefold star-like primary Si [32].

2.3.2.2. Feathery primary Si

Figure 4 illustrates the microstructure of feathery-type primary Si observed in hypereutectic Al-Si alloy castings. Kang et al. [31] found that superheat temperature significantly affects the morphology of primary silicon. At temperatures above the liquidus, silicon tends to form clusters that rearrange into different morphologies during solidification, depending on the cooling rate. When the superheat exceeds 850 °C, it affects cluster formation and the solidification process, resulting in a complex morphology known as the "fishbone" or feathery structure. This was observed even in hypereutectic alloys processed by electromagnetic stirring or vibration. It was also found that treating the melt at 100 °C above liquidus promotes feathery Si, while lower superheat temperatures lead to more refined and regular primary Si particles [33].

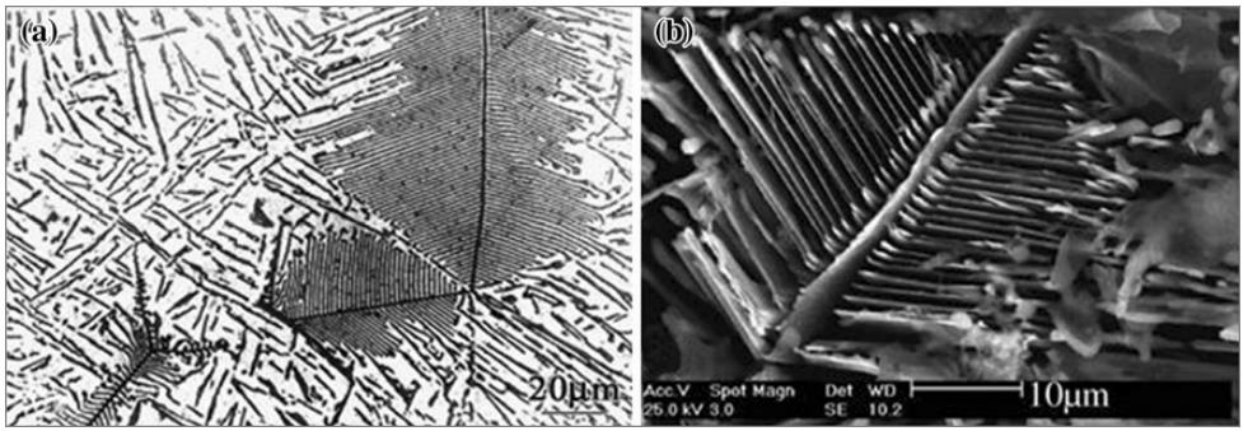

Figure 4. Micrographs display feathery Si in hypereutectic Al-Si alloy: (a) optical microscopy image; (b) SEM image of the etched sample [33].

2.3.2.3. Polyhedral primary Si

Polyhedral primary silicon commonly forms in hypereutectic Al–Si alloys, especially when inoculated with phosphorus [5]. **Figure 5** illustrates the microstructure of polyhedral primary Si. Studies by Liang et al. [34], show that phosphorus lowers the nucleation energy by satisfying the optimal contact angle (~30°) for heterogeneous nucleation, promoting uniform and regular silicon growth.

Xu and Jiang. [13] found that overheating the melt affects silicon morphology. At 1050 °C, silicon formed polygonal shapes, whereas at 850 °C, it was irregular. This change is linked to the size of Si–Si clusters—larger clusters promote star-like shapes, while smaller ones prefer octahedral growth.

The fundamental shape of polyhedral primary silicon is octahedral, although it may appear in various polygonal forms due to sample polishing (**Figure 6**). Growth starts as a sphere and transitions into an octahedron via branching along crystallographic directions ([100] and [110]). **Figure** 7 depicts the process of primary silicon nucleating and developing into an octahedral structure. The transition from sub-octahedral to perfect octahedral form depends on cooling rate, impurity rejection, and growth velocity.

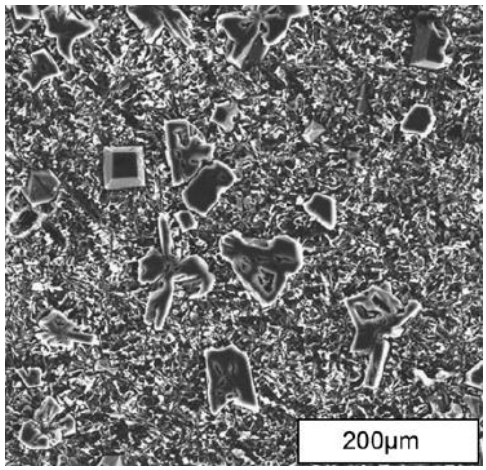

Figure 5. Micrograph displaying polyhedral primary silicon [35].

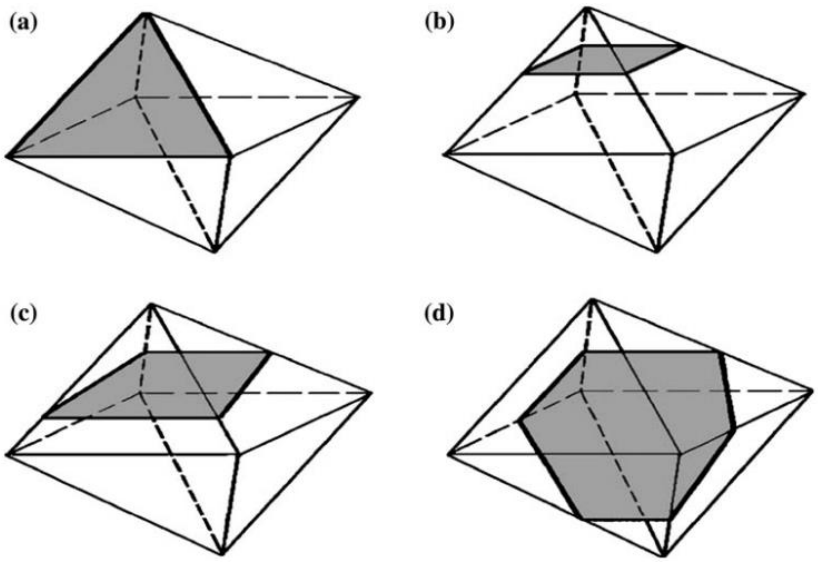

Figure 6. A schematic showing the polygonal outlines of octahedral primary silicon as observed in two-dimensional cross-sections: (a) triangular, (b) square, (c) trapezoidal, and (d) hexagonal shapes [35].

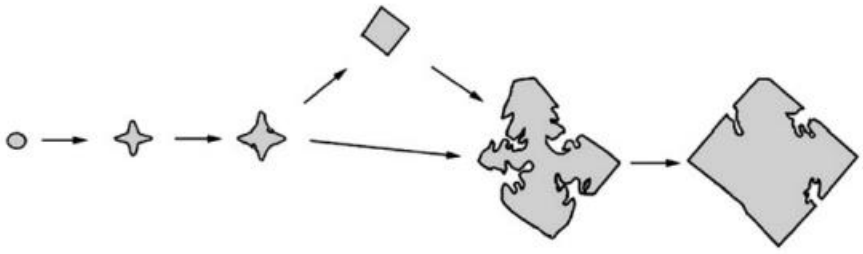

Figure 7. Diagram showing the various stages of octahedral primary silicon growth [35].

2.3.2.4. Dendritic primary Si

Dendritic primary Si forms in hypereutectic Al–Si alloys under low undercooling or when modified with strontium (Sr). **Figure 8** illustrates the microstructure of dendritic primary Si. Sr additions poison the TPRE growth, leading to branching and dendritic structures. This occurs as Sr accumulates at the growth front, lowering the growth temperature and suppressing the formation of {111} facets. Yilimaz et al. [20] show that at low growth rates, Sr accumulates at the silicon–liquid interface, blocking growth steps and causing the silicon to grow with multiple branches and facets.

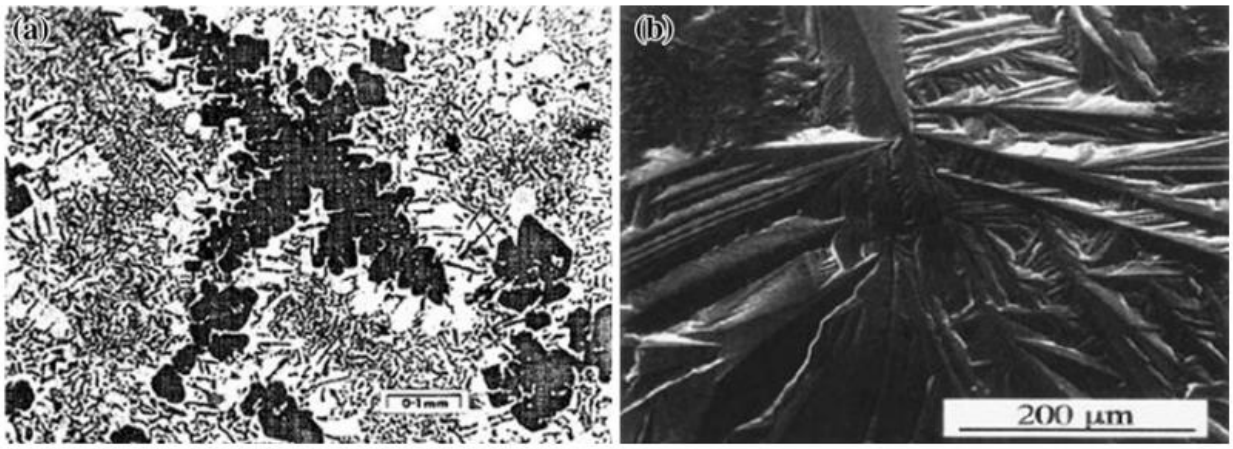

Figure 8. Micrograph displaying dendritic primary Si modified by strontium (a), alongside a SEM image showcasing the dendritic structure of silicon (b) [10], [20].

2.3.2.5. Plate-like primary Si

Plate-like silicon forms under low cooling rates and low undercooling conditions. These particles grow isotropically from the liquid, with more rapid attachment at certain lateral surface sites. Plate-like primary Si was developed by the action of twin boundaries that seem parallel to flat sides (TPRE), as reported by Fredriksson et al [14]. **Figure 9** depicts the microstructure of the plate-like primary Si morphology typically found in unmodified hypereutectic alloys.

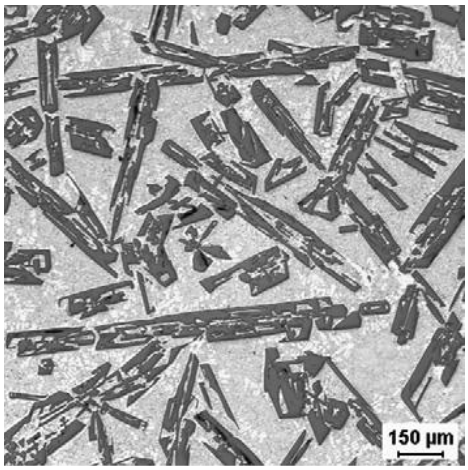

Figure 9. Micrograph displaying plate-like primary Si [12].

2.3.2.6. Spheroidal primary Si

Spheroidal primary Si is formed through sodium (Na) treatment of the hypereutectic alloy. These particles have fewer twins in the radial direction and consist of fewer interpenetrating twin crystals. Increasing Na content leads to higher twin density, forming structures known as "spherulites." **Figure 10** illustrates the microstructure of spheroidal primary Si.

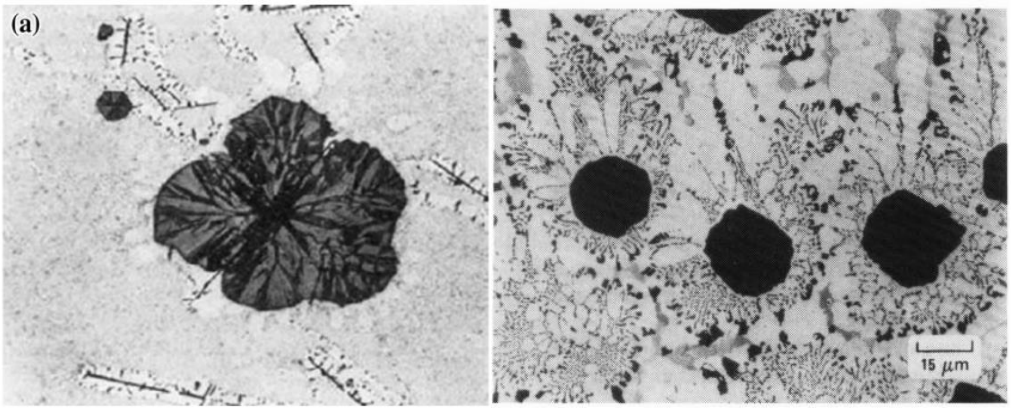

Figure 10. Micrographs displaying spheroidal primary Si in hypereutectic Al-Si alloys [5], [30].

2.3.3. Solidification of Eutectic

Following the formation of primary Si, the remaining liquid undergoes eutectic transformation at the eutectic temperature (577°C for the Al-Si system). In an Al–18 wt.% Si hypereutectic alloy, the equilibrium solidification results in approximately 6.7 vol.% primary silicon and 93.3 vol.% eutectic Al-Si structure. This transformation involves the simultaneous growth of Si and Al phases

in a lamellar structure. The eutectic growth in Al-Si alloys typically follows the cooperative growth theory, where alternating layers of Al and Si grow side by side. This layered growth helps accommodate the two phases' differing crystal structures and thermal expansions. Eutectic solidification theory generally involves the simultaneous growth of two or more solid phases from a liquid, described as $L \rightarrow \alpha + \beta$. These phases form in alternating patterns through a diffusion couple zone that efficiently transports solutes (**Figure 11**).

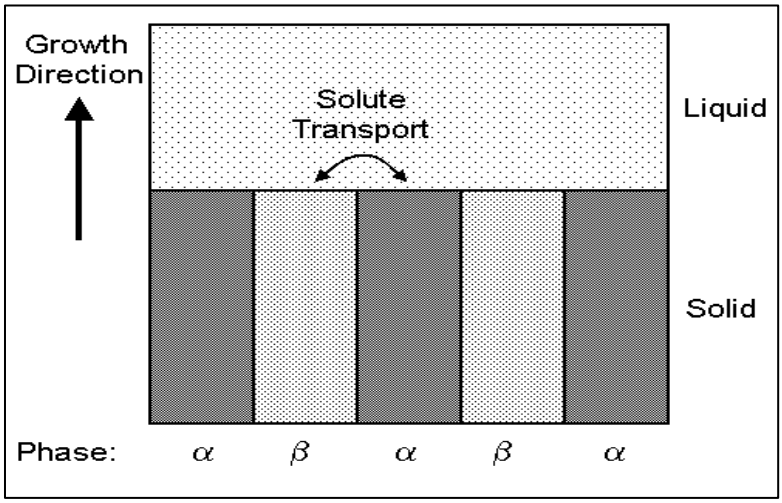

Figure 11. Schematic of eutectic solidification.

The morphology of eutectic structures can vary widely, influenced by the growth characteristics of the individual phases involved. These can be broadly classified into:

1. **Regular Eutectic:** Characterised by the solidification of two non-faceted phases, which typically exhibit isotropic bonding. This leads to rough interfaces at the microscopic level, including atomic-scale ledges and steps that facilitate the attachment of atoms from the liquid phase. The lack of a preferred growth direction in these structures is due to their isotropic nature, allowing for more random orientation during growth.
2. **Irregular Eutectic:** Occurs when at least one of the phases exhibits faceted growth, which is common in crystals with strong directional bonds. This type of growth results in smooth interfaces aligned along specific crystallographic directions, dictating a more ordered and directional growth pattern.

The concept is further enriched by Jackson's introduction of the dimensionless α parameter, which quantifies interface roughness based on the thermal and structural properties of the material [36].

$$\alpha = \frac{\eta}{\nu}\frac{\Delta H_f}{RT_m} = \xi\frac{\Delta S_f}{R} \qquad (5)$$

Where,

- η: number of nearest neighbours for the growth unit at the solid-liquid interface of the crystal.
- ν: is the coordination number for these neighbours.
- ξ: Orientation factor; defined as the ratio between η and ν.
- ΔH_f: latent heat of fusion.
- T_m: The melting temperature.
- R: The ideal gas constant
- $\Delta S_f/R$: the dimensionless entropy of fusion.

Values of α greater than 2 suggest faceted growth due to higher entropy of fusion, resulting in smooth interfaces, while α less than 2 indicates non-faceted growth with rough interfaces. In addition, eutectic morphology varies based on the volume fractions (Vf_α….) of the phases involved, influencing the microstructure's formation, whether rod-like, lamellar, or acicular (**Figure 12**).

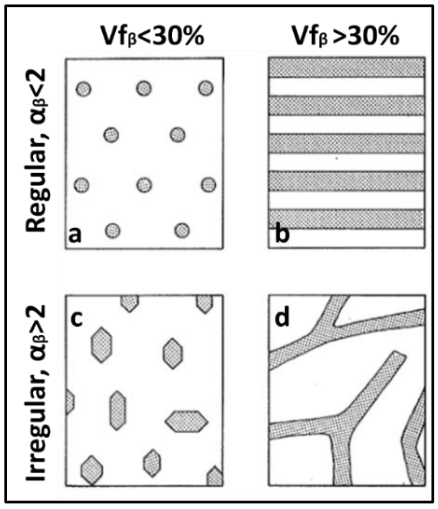

Figure 12. Classification of eutectic structures according to Jackson's factor, α, and volume fraction, Vf_β; featuring regular eutectic structures as (a) rod and (b) lamellar, and irregular eutectic structures as (c) fibrous and (d) lamellar [37].

The eutectic couple zone is the region where two phases grow simultaneously and cooperatively during eutectic solidification, with its symmetry and structure depending on the faceting nature of

the phases and solidification conditions. The eutectic couple zones for regular and irregular structures differ. In regular eutectic structures, two non-faceted phases grow under symmetric solidification conditions reflected in symmetric phase diagrams and eutectic couple zones. In contrast, irregular structures with both faceted and non-faceted phases solidify in an asymmetrical couple zone (**Figure 13**). The non-faceted phase, needing minimal undercooling, can grow faster than the faceted phase, allowing growth at the eutectic composition. Thus, a pure eutectic structure in irregular systems is typically achieved only in hypereutectic compositions.

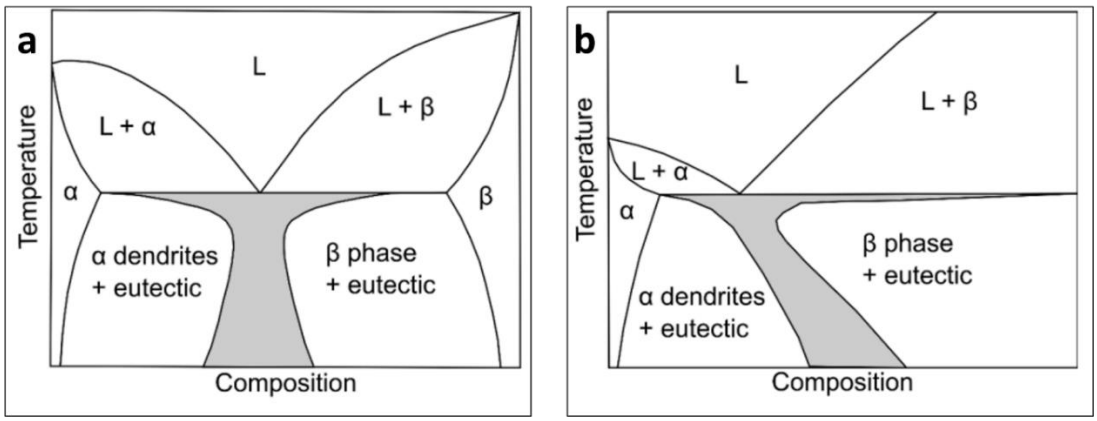

Figure 13. (a) Symmetric zone in non-faceted eutectic phases; (b) an asymmetric coupled zone in faceted-non-faceted phases [38].

The eutectic Al-Si system comprises non-faceted Al and faceted Si phases. The growth mechanism of the industrially unmodified Al-Si eutectic alloy follows an irregular plate-like structure. The eutectic structure consists of soft Al as the matrix and plate-like Si. The solidification of the irregular eutectic takes place in an asymmetric coupled zone. The eutectic solidification mechanism requires one phase to solidify first, known as the leading phase. In a hypereutectic Al–Si alloy, the leading phase is primary Si.

2.3.4. Growth of Eutectic

Eutectic growth involves the diffusion of atoms at the eutectic front, where A atoms are rejected from the β phase and B atoms from the α phase, leading to the diffusion boundary layer. This diffusion significantly influences the inter-lamellar distances (λ), with larger diffusion ranges causing greater distances.

The α, β, and L phases must maintain thermodynamic equilibrium, which can be achieved with a curved s/l front for each lamella. The curvature at the tri-junction points (α/β/L) affects the inter-lamellar distance, with smaller curvatures increasing it (**Figure 14**). Additionally, grain boundaries typically require a lower than equilibrium temperature to maintain thermodynamic stability due to their higher free energy.

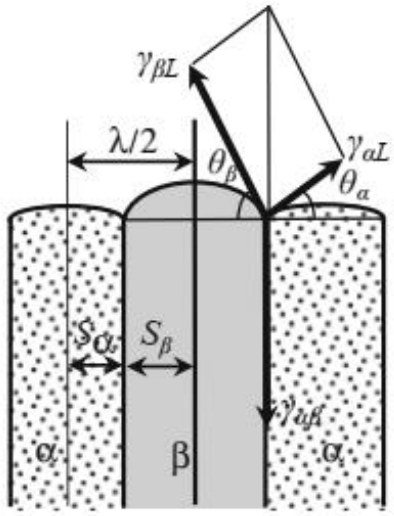

Figure 14: Morphology of the curvature s/l front with contact angle θ. The front is characterized by parallel grooves, which are lowered and aligned perpendicular to the direction of growth.

The driving force of solidification is recognized as undercooling (ΔT). The total undercooling at the s/l front can be expressed as:

$$\Delta T_{Tot} = \Delta T_{Diff} + \Delta T_{Cap} + \Delta T_K \quad (6)$$

where,

ΔT_{Diff}: Diffusive undercooling, also known as constitutional undercooling, arises from compositional changes between the eutectic and interface compositions. It is calculated by:

$$\Delta T_{Diff} = m\,(C_E - C(x)) \quad (7)$$

ΔT_{cap}: Capillary Undercooling, dependent on surface free energy and interfacial curvature, is given by:

$$\Delta T_{Cap} = \frac{\Gamma}{r(x)} \quad (8)$$

ΔT_K: Kinetic and thermal undercooling are typically negligible in non-faceted regular eutectics due to their rough interface allowing easier atom attachment.

Zener. [39] proposed that regular eutectic structures form only at the minimum undercooling. Later, in 1966, Jackson and Hunt. [40] developed a model that simplified eutectic growth by assuming a flat solidification front and equal undercooling for both solid phases. Their model linked growth rate, undercooling, temperature gradient, and microstructural features like lamellar spacing, successfully predicting regular eutectic formation and forming the basis for later studies.

In contrast to regular eutectics, predicting the growth behaviour of irregular eutectics presents additional complexities. A key difficulty arises from the presence of a faceted phase—such as silicon in the Al–Si eutectic system—which makes kinetic undercooling non-negligible. This deviates from the assumptions used in regular eutectic models, where undercooling is minimal and interfaces are rough. Moreover, the typical condition of minimum undercooling for cooperative growth does not apply here, as irregular eutectics exhibit a broad range of local spacings between silicon flakes.

2.4. Forced Melt Flow Induced by a Rotating Magnetic Field

Microstructure formation during solidification is significantly impacted by melt flow. There are two types of melt flow: natural and forced melt flows. There are several causes of natural melt flow, including the difference in density, temperature, and concentration distribution between the solid and liquid phases. This flow also happened due to the gravity effect during solidification. While forced melt flow happens in response to the imposition of external conditions such as the rotating magnetic field (RMF) or the traveling magnetic field (TMF) that can be applied during solidification [41].

Applying forced melt flow by RMF, or in other words, the magnetic stirring by RMF during solidification, is a good processing technique that has attracted great attention in the last few years. In addition, it has been proven to be an efficient method for enhancing the microstructure of alloys [42]. Due to the conductivity of the molten Al-Si alloys, they can be subjected to RMF to improve the internal metallurgical structure, control the shape, distribution, and size of the alloying phases, and ultimately increase the quality of the final product [24].

A rotating magnetic field (RMF) is a magnetic field generated by symmetrically placed coils supplied with polyphase currents. It can also be produced using a single-phase current with two field windings designed to create phase-shifted magnetic fields. An induction motor comprises a stator and a rotor. The stator contains stationary windings designed to produce a rotating magnetic field, with its angular velocity corresponding to the frequency of the alternating current. The rotor, or armature, features short-circuited coils embedded in slots, which generate a current when exposed to the changing magnetic flux from the stator's field poles. The interaction between the magnetic flux of the armature current and the field poles causes the armature to rotate in a specific direction.

A symmetric rotating magnetic field can be generated using just two polar-wound coils phased 90 degrees apart. However, using three sets of coils is more common, as this arrangement is compatible with a symmetric three-phase AC sine current system. In this setup, each coil set is phased 120 degrees relative to the others. For illustration purposes, the magnetic field is considered a linear function of the coil's current.

Combining three sine waves phased 120 degrees apart along the motor's axis produces a single rotating vector with a constant magnitude. The rotor maintains a stable magnetic field, causing its north pole to be drawn toward the stator's magnetic field's south pole, and vice versa. This magneto-mechanical attraction generates a force that compels the rotor to move in sync with the rotating magnetic field.

According to Faraday’s law, a rotating magnetic field generates potential differences in an electrically conductive melt, inducing eddy currents. The interaction between these eddy currents and the external magnetic field produces the Lorentz force, which acts on the melt volume. The resulting flow pattern is primarily determined by the distribution of this force.

The RMF induces two distinct flow types during solidification under earth conditions [43], [44]: i) A primary azimuthal flow driven by the Lorentz force, resulting from the interaction between the magnetic field and electric charges in the melt; The azimuthal velocity is zero at the centre and reaches its maximum near the vessel walls. Azimuthal flow is perpendicular to the axis of the solidification direction. (ii) A weaker secondary meridional flow (about ten times slower), caused by the imbalance between centrifugal force and radial pressure near the horizontal walls. This flow

forms two toroidal vortices in the radial–axial (r–z) plane, transporting alloying elements from the mushy zone to the liquid ahead of the solidification front (**Figure 15, a**). Azimuthal and axial flows can be beneficial for removing impurities, promoting the growth of defect-free crystals, and improving the quality of the resulting material. However, these flows can also lead to undesirable effects such as segregation and non-uniform growth [45]. As a result of the combination of the azimuthal and axial flows, the motion is spiral (**Figure 15,b**), which substantially influences the alloying element's distribution, concentration, and growth morphologies [42]. Both azimuthal and axial flows can be controlled and optimized by adjusting the parameters of the RMF. By harnessing the power of the RMF to control melt flow, researchers can improve the quality and performance of a wide range of materials, from metals and alloys to semiconductors and biomaterials.

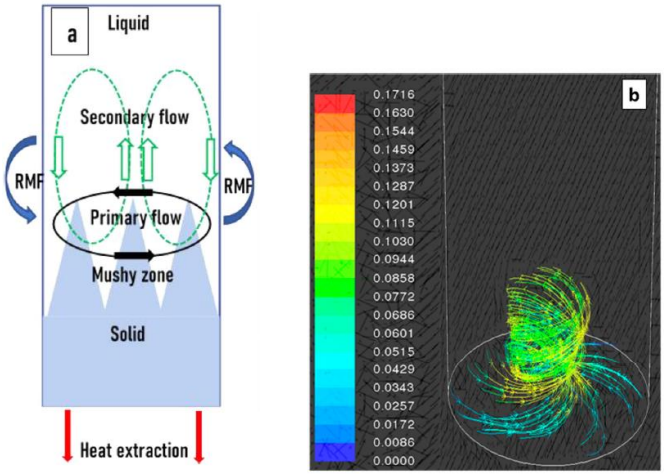

Figure 15. (a) The unidirectionally solidified sample's primary and secondary melt flow. (b) Simulated spiral flow in a liquid phase, with flow channels colored according to velocity [26], [45].

2.5. Effect of Eutectic and S/L Front Velocities and RMF on Solidification of Alloys.

2.5.1. Grain Refinement and Morphology

Several studies [26], [42], [46], [47] have investigated the effect of RMF on the microstructure of metallic alloys, with most finding that applying RMF during solidification leads to a more refined microstructure and improved mechanical properties. One study by Al-Omari et al. [42] presents an experimental investigation of the impact of forced melt flow on the microstructure of Al-12.6 wt.%-Si eutectic alloy. The samples were solidified with different magnetic induction at a eutectic front velocity of 0.1 mm/s and a 6 K/mm temperature gradient. The study shows that the forced flow of molten metal by RMF can significantly affect the size and distribution of the eutectic Si in

the solidified structure. Specifically, the authors observed a finer eutectic structure in the samples subjected to forced melt flow than those not.

Another study by Yan et al. [46] shows that RMF is a melt treatment method that generates a stirring effect that breaks up the dendritic network in CuNi10Fe1Mn alloy and promotes nucleation and growth of fine equiaxed grains. The researchers reported also that the application of RMF has been shown to improve the mechanical properties of the alloys.

Researcher Veres et al. [26] studied the impact of forced melt flow on the solidified microstructure and mesostructured of the Al-7wt.% Si hypoeutectic alloy by performing unidirectional solidification experiments utilizing RMF. Researchers noticed considerable macro segregation along the sample due to the secondary flow. The stirred part has three times as many grains as the non-stirred part, and the dendritic structure is more homogeneous after stirring [26].

In addition to applying RMF, controlling the eutectic front velocity during solidification is another method for refining the microstructure of metallic alloys. Several studies have investigated the effect of eutectic front velocity on the eutectic microstructure. Jackson and Hunt (J-H model) established a generic quantitative equation based on a diffusion problem at the eutectic front, which is $\lambda^2 v = \text{const}$, whereas λ is the eutectic interlamellar distance and v is the front velocity [40]. They concluded that the eutectic interlamellar distance is an important microstructural parameter for eutectic alloys and is affected by the front velocity. Zuo et al. [48] studied the effect of front velocity and external magnetic field on the microstructure and mechanical properties of Ag-Cu eutectic alloys and found that increasing front velocity led to a more refined microstructure and improved mechanical properties.

In a Bridgman furnace, Koçak et al. [49] unidirectionally solidified upwards Bi-Pb alloy at the eutectic composition at five different eutectic front velocities at constant temperature gradients to study how eutectic front velocities affect eutectic spacing and microhardness. Their research shows that for a given G, interlamellar distance reduces, and microhardness increases as the front velocity increases.

Several studies have investigated the effect of different solidification parameters on the primary Si of hypereutectic alloys. Xu and Jiang described the effect of cooling rate and melt overheating temperature on the hypereutectic structure by observing the morphologies and size changes of the

primary Si under different solidification conditions. With an increase in the temperature of melt overheating, they found that the morphologies of primary Si changed from star-like to octahedral shape, and the size of the particles decreased. As the cooling rate increases, the size of the primary Si gets smaller [13].

Ullah and colleagues. [12] examined the morphologies of primary Si crystals during solidification of Al-Si alloys that contain 17-38 wt.% Si. Their findings revealed that lower Si concentrations led to Si morphologies resembling fishbones or star-like shapes. However, as the Si content increased, the growth pattern shifted to larger plates that exhibited a propensity to grow in layers.

Yan and co-authors. [50] investigated the influence of the Sr-Modifier and the Serpentine Pouring Channel Process on primary Si in their study. Their analysis involved quantifying the size of primary Si particles by determining their equivalent diameter. The findings demonstrated that in the A390 alloy, employing both the water-cooled copper serpentine pouring channel and Sr-modifier in combination resulted in significant refinement of primary Si particles, reducing their size to a range of 25.2–28.5 μm.

Jie et al. [51] found that applying an RMF during solidification significantly influences the microstructure of the hypereutectic Al-Si alloy. The primary Si phase tends to separate and distribute uniformly along the radial direction of the sample, resulting in a more refined primary Si phase in the final microstructure. The researchers found that this phenomenon is attributed to the Lorentz force generated by the interaction between the RMF and the eddy currents induced in the melt, which induces a convective motion and promotes the separation of the primary Si phase from the melt.

These studies indicate that forced melt flow by RMF and controlling the solidification front velocity refines the microstructure of metallic alloys. However, further investigation is still needed into the RMF, eutectic front velocity, and s/l front velocity conditions for hypereutectic Al-18 wt.% Si alloys and their effect on the microstructure of these alloys. In addition, despite advances in understanding the solidification of primary Si in such alloys, a comprehensive investigation into the characteristics of primary Si in hypereutectic Al-Si alloys and the effect of solid/ liquid (s/l) front velocity and the application of an RMF during solidification on the primary Si is still lacking. This research focuses on how RMF and varying front velocities influence the microstructure, specifically, the eutectic lamellas and primary Si, in hypereutectic Al-18 wt.% Si alloy.

2.5.2. Macro-Segregation

Macro segregation is a pervasive issue in the casting of hypereutectic Al-Si alloys. This phenomenon manifests as the inhomogeneous distribution of solute elements on a macroscopic scale, severely impacting the cast components' mechanical properties and overall integrity. Al-Si hypereutectic alloys are particularly susceptible to macro segregation [2], [5]. The primary Si phase in these alloys tends to segregate, leading to regions with significantly different compositions and properties. Understanding and controlling macro segregation is thus crucial for optimizing the performance and reliability of components made from these materials. During the unidirectional solidification process, the distribution of solute elements, particularly Si, can change due to various dynamic factors. Among these factors, the solid/liquid (s/l) front velocity and forced melt flow induced by rotating magnetic fields (RMF) play pivotal roles in influencing the macro segregation patterns.

The solidification process of Al-Si hypereutectic alloys is significantly influenced by the velocity of the s/l front. The front velocity determines the cooling rate, which in turn affects the microstructure evolution, including the size, shape, and distribution of primary Si particles and eutectic lamellas [16]. Higher solidification rates typically lead to finer microstructures, which can enhance the mechanical properties of the alloy.

It has been recognized for many years that forced melt flow within a melt can have profound effects on the solidification structure. Whenever forced melt flow is artificially applied during the casting of alloys, some changes in the microstructure can be observed. One observation, for instance, is a transition from columnar to equiaxed microstructure [52], grain refinement [42], or macro segregation [45]. In the context of alloy solidification, the control of macro segregation has been a focal point of research. Numerous studies have established that forced flow within the mushy zone, the semi-solid region during solidification, plays a pivotal role in forming macro segregation patterns [53]–[55]. This forced flow can be externally driven by the application of magnetic fields, particularly the rotating magnetic field (RMF) and the travelling magnetic field (TMF), which have proven effective in influencing the alloy's internal flow dynamics during solidification [45], [51], [56]–[61].

For instance, Zimmermann et al. investigated the effect of RMF on directionally solidified AlSi7Mg0.6 alloy and observed that the forced flow led to axial macro segregation, resulting in Si

enrichment at the centre of the sample [56]. Similarly, Zaïdat et al. studied the impact of TMF on an Al-3.5wt%Ni alloy and reported the induction of freckled segregation during directional solidification [57]. These findings were further expanded upon by Noeppel et al., who provided a more detailed explanation of the macro segregation formation processes under the influence of both RMF and TMF in solidified alloys [58].

Advancements in controlling macro segregation have also been achieved. Willers et al. introduced a novel approach for modulating macro segregation in Al-Si alloys by varying the application timing of RMF, demonstrating a method to tailor segregation effects [59]. Jie et al. recently proposed a mechanism for macro segregation formation based on a series of Al-Si alloy solidification experiments with RMF [51]. Their investigation focused on the behaviour of the primary Si in a hypereutectic Al-30 wt.% Si alloy subjected to RMF during solidification. The findings revealed that RMF application caused the primary Si to accumulate at the inner wall of the crucible, resulting in the formation of a Si-rich surface layer.

Kassab and his colleagues [45] studied the impact of forced melt flow via an RMF on the macrostructure of an Al-12.6 wt.% Si eutectic alloy. Post-solidification, the structure revealed that RMF stirring introduced new phases, specifically primary aluminium and primary Si, which were absent before stirring. The Si concentration and area fractions of these phases were measured using Energy-Dispersive Spectroscopy (EDS) and advanced image processing. The results showed that RMF during solidification significantly alters the macrostructure of Al-Si eutectic alloys by inducing macro-segregation, reducing the eutectic structure, and modifying the Si concentration distribution.

Shaodong and colleagues [60], studied how static magnetic fields affect the segregation of primary Si in directionally solidified Al-Si alloys. Their experiments and simulations revealed that the intense melt flow in the Al-21 wt.% Si alloy under a magnetic field is the main cause of macro segregation. This flow pushes solute Si to cooler areas, promoting Si precipitation and forming a U-shaped interface, which transitions to a planar interface as the magnetic field intensity increases. This process enhances macro segregation and helps understand how forced flow alters alloy solidification structures under magnetic fields.

Qingchuan and his team [61], explored how temperature fields and electromagnetic stirring affect primary Si segregation in Al-Si melts. Their experiments showed that a temperature gradient is

crucial for Si separation, and electromagnetic stirring enhances this effect, creating a Si-rich layer (65-70 wt.% Si). The Si-rich layer forms from the continuous growth process of primary Si by absorbing Si atoms from the Al-Si melt, aided by electromagnetic stirring. This technique promises improved Al-Si composites and a cost-effective Si supply for photovoltaics.

Despite the recent research on the macro segregation of Al-Si alloys, further research is necessary to understand the effects of forced melt flow, specifically induced by RMF, on the macro segregation evolution during the solidification of hypereutectic Al-Si alloys. Additionally, there is a lack of studies examining the influence of s/l front velocity on macro segregation evolution in these hypereutectic alloys. One of the aims of this study is to investigate the effect of s/l front velocity and forced melt flow by RMF on the macro-segregation evolution during the unidirectional solidification of hypereutectic Al-18 wt.% Si alloy.

3. Experimental Work

This chapter will detail the solidification experiments, encompassing the alloy that was solidified, the solidification apparatus, the methodologies employed in the solidification experiments, and the process for preparing the samples. The samples I analysed were solidified by Dr. Arnold Rónaföldi as part of the MICAST project.

3.1. Alloy and Solidification Facility

Samples of Al-18 wt% Si hypereutectic alloy were utilized for the solidification experiments. The solidification process was conducted in a crystalliser equipped with a High Rotating Magnetic Field (CHRMF) [26], [45], [62]. Here are the main parts of a CHRMF (**Figure 16**):

1- Sample and Sample Holder: The sample was placed in an alumina capsule for its thermal stability and compatibility with high-temperature processes. The temperature distribution along the sample was measured at 10 different points using K-type thermocouples. These thermocouples were placed in grooves along the surface of the alumina capsule. The alumina capsule, along with the thermocouples, was encased in a quartz tube, providing a shield against the water. A copper cooling core was attached to the base of the quartz tube and connected to the alumina capsule to facilitate unidirectional heat dissipation (**Figure 17**) [52].

2- A vertical Bridgman-type tube furnace equipped with four independent heating zones: The furnace design features an inner diameter of 20 mm and a total length of 200 mm. A water-cooling system was integrated into the furnace's body to regulate the temperature and prevent overheating of the induction coils [52]. The furnace could reach a maximum temperature of 1000°C, with a temperature gradient capability of up to 10 K/mm. The sample moving velocity is adjustable between 0.002 mm/s and 1 mm/s.

3- A control unit: It is a unit that manages the movement of samples from the melting furnace to the direction of the cooling unit, and it utilises a step motor to regulate the velocity of the sample's movement. The step motor lets the control unit maintain a consistent and accurate speed during the transfer process.

4- The MagnetoHydroDynamic stirring (MHD) inductor: it is a device that generates a rotating magnetic field during solidification.

5- A water-cooling unit: the sample is cooled by immersing the copper block in the water.

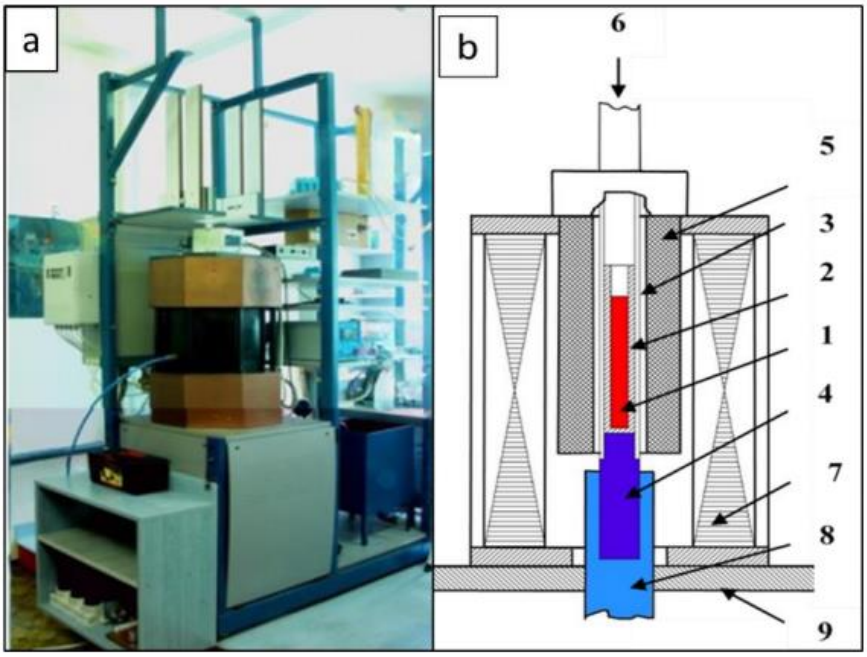

Figure 26. A schematic overview of the solidification facility, showing the following components: (1) Sample, (2) Alumina capsule, (3) Quartz tube, (4) Copper cooling core, (5) Furnace with four heating zones, (6) Step motor, (7) RMF inductor, (8) Water c cooling system, and (9) Basement [26], [45].

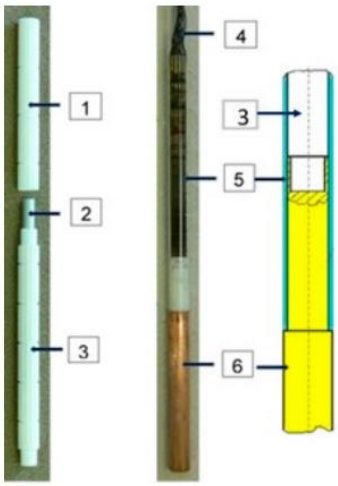

Figure 17. Illustration of the sample and its holder: 1 and 3, alumina capsule; 2, sample; 4, thermocouples; 5, quartz tube; 6, copper cooling core.

3.2 Solidification Experiments

Hypereutectic Al-18 wt.% Si alloy was produced by Hydro GmbH company using high-purity metals. Hypereutectic Al-18 wt.% Si alloy samples were prepared using a controlled unidirectional solidification process, using the vertical upward Bridgman method within the specified solidification facility. This process was achieved by vertically transitioning the sample from the furnace chamber to the cooling bath. The samples, cylindrical in shape, measured 8.1 mm in diameter and 90 mm in length.

The experimental setup involved solidifying five hypereutectic samples using different samples movement velocities (v_m) (**Table 1**). The average value of the average temperature gradient (G) was 8 K/mm. The initial half (45 mm in size) of each sample was solidified without the application of magnetic stirring. The subsequent half of each sample was solidified under the influence of an RMF with an intensity of B = 7.2 mT.

Table 1. The experimental parameters.

Name of sample	v_m [mm/s]	v_{SL} [mm/s]	v_e [mm/s]	B [mT]	G [K/mm]
A	0.02	0.02	0.02	0__7.2	8
B	0.05	0.04	0.05	0__7.2	8
C	0.10	0.08	0.09	0__7.2	8
D	0.20	0.20	0.20	0__7.2	8
E	0.50	0.40	0.40	0__7.2	8

The thermal parameters (solid/liquid (S/L) and eutectic front velocities ($v_{SL} and\ v_e$)) and temperature gradient (G) were calculated from the *"*Temperature-Time*"* function developing along the length of samples during the solidification process. The procedure for calculating the solid/liquid front and eutectic front velocities in hypereutectic Al-18 Si alloy during solidification begins by determining key solidification temperatures (The liquidus and the eutectic temperature) using Differential Scanning Calorimetry (DSC). The liquidus temperature is approximately 638°C , while the eutectic temperature is about 577°C.

Then, thermocouples recorded temperature data over time at various positions along the sample (3.2, 8.7, 16.8, 26.3, 35.3, 43.9, 54, 63.5, 73.5, and 82 mm from the bottom of the sample). For each thermocouple, critical times were noted:

- The time when the temperature first falls below 638°C at the given thermocouple (or at the first thermocouple) indicates the passage of the S/L front for primary Si.
- The time when the temperature reaches and stabilises at 557°C at the given thermocouple (or at the first thermocouple) indicates the eutectic front formation.

The velocities of these fronts were calculated from measured data using the formula: Velocity = $\frac{\Delta x}{\Delta t}$, where:

- Δx is the distance between consecutive thermocouples.
- Δt is the time difference between the fronts reaching these thermocouples.

Finally, the front velocity was plotted against the positions of thermocouples (**Figure 18**).

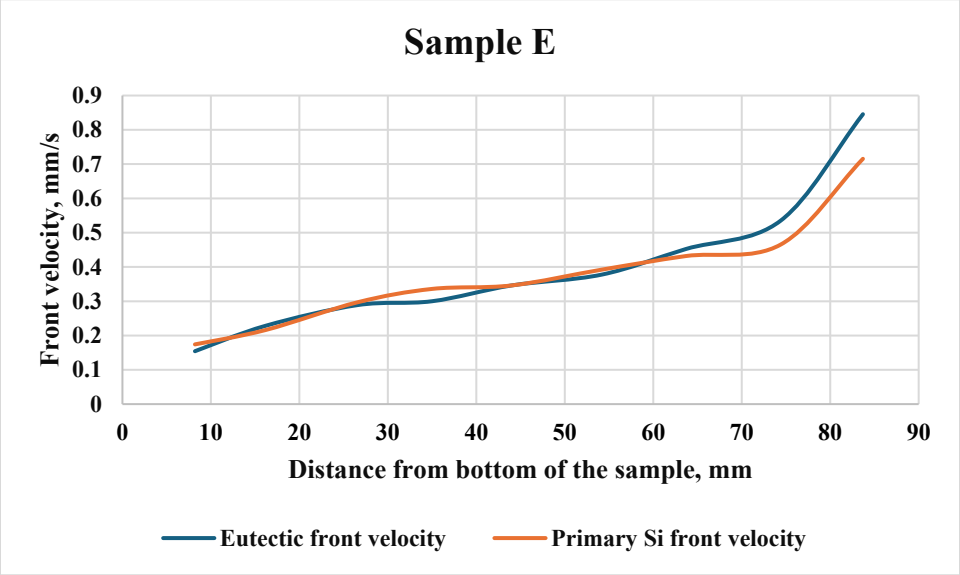

Figure 18. The velocities of solid/liquid and eutectic fronts as a function of distance from the bottom of the sample with s/l front velocity of 0.40 mm/s.

The temperature gradient in a hypereutectic Al-18 Si alloy during the solidification process was calculated using a "Temperature-Time" function. Temperature data were collected from various points along the sample length at consistent time intervals, with thermocouples strategically placed to monitor changes. Differences in temperature (ΔT) between adjacent thermocouples were recorded at each time point to determine the change over the distance (Δx) between them.

The distances between each pair of adjacent thermocouples were measured, providing the necessary Δx for calculations. Using the formula Temperature Gradient = $\frac{\Delta T}{\Delta x}$, the temperature gradient was computed for each segment along the sample. This process was repeated at different intervals during the solidification to capture the evolution of the temperature gradient over time.

3.3. Sample Preparation

The solidified samples were prepared for analysis following standard metallographic procedures. Longitudinal sections were cut and then subjected to grinding, polishing, and etching using an aqueous hydrofluoric acid (HF) solution.

4. Measurement Methods

This chapter examines micro and macro-scale solidified samples to assess the impact of RMF, eutectic front velocity, and s/l front velocity on the solidified structure. In this chapter, the parameters characterized at each scale and the measurement techniques used were described.

4.1. Characterisation of the Eutectic Structure

Quantitative measurements of the average eutectic Si lamella length, the angle between the axis of the eutectic Si lamella and the direction of solidification movement, as well as the average eutectic inter-lamellar distance (λ), were considered in our attempt to characterize the irregular eutectic structure in the Al-18 wt.% Si hypereutectic samples. **Figure 19** shows the studied alloy's characterization method of eutectic lamellas. These microstructural characteristics were obtained from images captured with a C. Zeiss Axiovert 40 MAT-type microscope (light microscope). The images were processed using a mosaic acquisition system to analyse extensive regions of the sample. This mosaic image was constructed from a sequence of smaller, systematically arranged images taken across the sample.

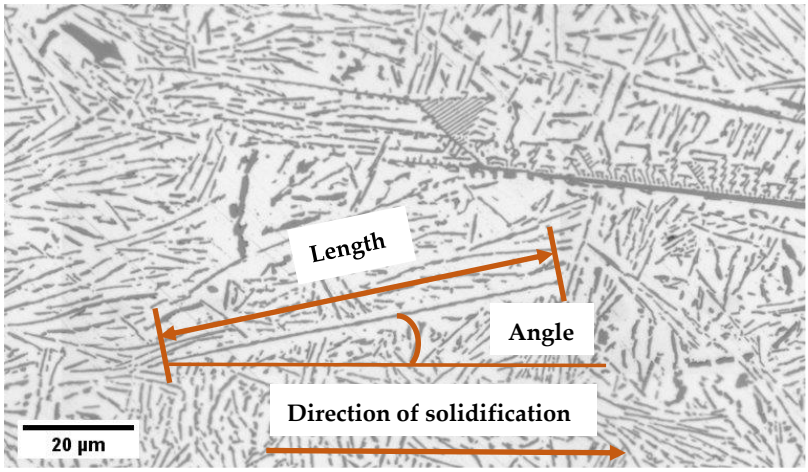

Figure 19. Characterization of the eutectic part in the Al-Si hypereutectic alloy with different characteristics.

Measurements of the lengths, angles, and interlamellar distances of the eutectic lamellas were performed in three regions in the non-stirred part and three different regions in the stirred part (**Figure 20**). The average value from these three locations was taken into account. The microscopic images were then analysedanalysed using the image analysis software ImageJ (Image J 1.52a, National Institutes of Health, LOCI, USA).

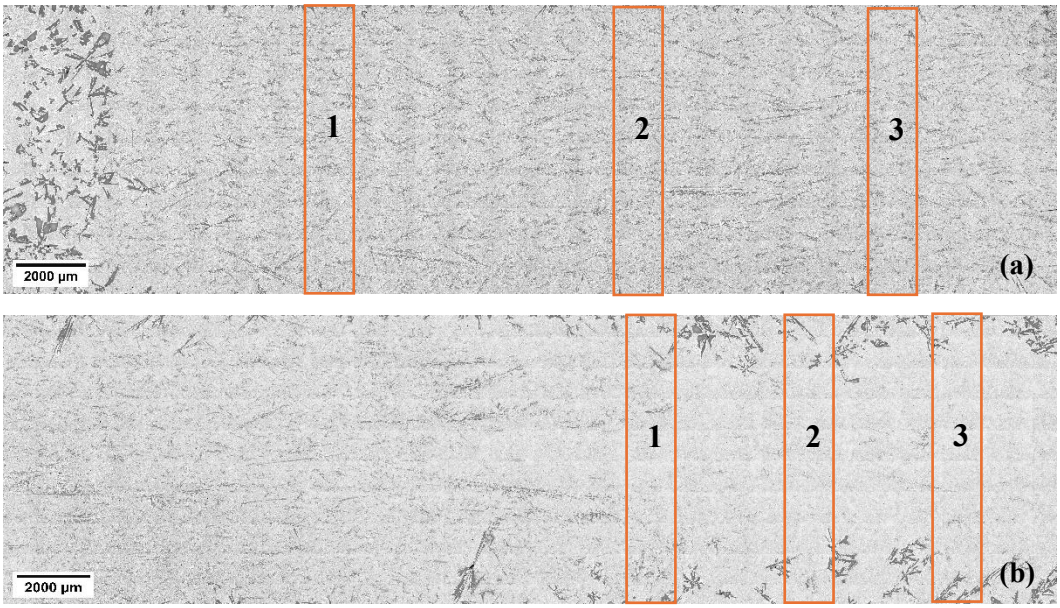

Figure 20: Locations of microstructure measurements of the lengths, angles, and interlamellar distances of the eutectic lamellas: (a) non-stirred parts. (b) stirred parts.

4.1.1. The Length of the Eutectic Lamellas

The length of the eutectic Si lamellas was measured using the maximum Feret diameter of each eutectic Si lamella. The length measurements were analysed for over 200,000 lamellas per sample by classifying the eutectic Si lamella's length into different ranges, ranging from (0–10) to (90–100) µm. For example, lamellas whose lengths fell between 0 and 10 µm were categorized into one group, those between 10 and 20 µm into another group, and so on, until reaching lamellas whose lengths ranged from 90 to 100 µm. For further analysis, the eutectic Si lamellas were categorized into two groups: fine lamellas, with lengths less than 10 µm, and coarse lamellas, with lengths greater than 10 µm. This procedure was applied to both the stirred and non-stirred sections of the five samples.

4.1.2. The Angle of the Eutectic Lamellas

The angle between the axis of the eutectic Si lamellas and the direction of solidification movement was measured as a Feret angle [41]. To study the effect of eutectic front velocity and RMF on the eutectic Si lamellas' angles, the measurements were analysed using a method developed by our research group [9,10]. (i) The lengths of the Si lamellas were categorized into four groups: (0–2), (2–5), (5–50), and (>50) µm. (ii) The orientation of each Si lamella in each length category was measured using the ImageJ software. (iii) The percentage of Si lamellas with the same angle was

then calculated for both the stirred and non-stirred sections (iv) Finally, an angle distribution curve was plotted for each length category for both the stirred and non-stirred parts of the samples.

4.1.3. The Eutectic Inter-Lamellar Distance

The eutectic inter-lamellar distance (λ) was measured by the 'Specific Perimeter Method (SPM),' developed by our research team. They created an equation that determined the derived mean distance between lamellas and proved its validity [41]. The inter-lamellar distance (λ) is given by Equation (1).

$$\lambda = 2 \times \frac{A_p \times (1 - A_f)}{N \times P_0} \qquad (9)$$

where,

P_0: average perimeter of the eutectic Si lamella in the investigated optical microscope images (μm).
N: Number of eutectic lamellas.

A_p: Area of the picture – area of the primary Si (μm^2).

A_f: Area fraction of the eutectic lamellas in the hypereutectic structure.

4.2. Characterisation of the Primary Si

Image J analysis software was employed to process the acquired micrographs. This involves segmenting the particles from the background matrix using a thresholding algorithm. The software distinguishes between primary Si particles and the surrounding aluminium matrix. Following this, primary Si particles were analysed, and particle size measurements were extracted, including area and perimeter. Shape factors, such as circularity and roundness, were also computed to assess the morphology of the primary Si particles.

4.2.1. Size Factor

This study evaluated the size of primary Si as an equivalent diameter. The equivalent diameter represents the diameter of a hypothetical circle with the same area as the particle's actual shape. The equivalent diameter (D_{eq}) is calculated using the following formula [63]:

$$D_{eq} = 2\sqrt{\frac{A}{\pi}} \qquad (10)$$

Where A is the area of a primary Si particle. The measurements were analysed by classifying the primary Si equivalent diameters into different ranges, ranging from (0-200) to (800-1000) µm. For example, particles whose equivalent diameter fell between 0 and 200 µm were categorized into one group, those between 200 and 400 µm into another group, and so on, until reaching particles whose equivalent diameter ranged from 800 to 1000 µm. For further analysis, the primary Si particles were categorized into two groups: fine particles, with an equivalent diameter of less than 200 µm, and coarse particles, with an equivalent diameter greater than 200 µm. This procedure was followed in stirred and non-stirred parts of five samples.

4.2.2. Shape Factors

This section introduced two crucial quantitative measures for characterizing the morphology of primary Si particles in hypereutectic alloys: circularity and roundness. These dimensionless shape factors are defined as follows:

4.2.2.1. Circularity

Circularity is a dimensionless shape factor that evaluates how close a particle is to a perfect circle, considering its overall roundness and the smoothness or irregularities of its perimeter. Particles with jagged or irregular boundaries will have lower circularity values, indicating a greater deviation from a smooth, circular form. The circularity (C) of each primary Si particle is calculated using the following formula [64]:

$$C = \sqrt{\frac{4\pi * (A)}{(P\text{^}2)}} \quad (11)$$

Where A represents the area of a primary Si particle, and P denotes its perimeter. The circularity value ranges from 0 to 1 (perfect circles). As the value approaches 0.0, it indicates an increasingly elongated and irregular shape.

4.2.2.2. Roundness

Roundness (R) measures how closely an object's shape resembles a perfect circle, focusing on its overall form rather than edge details. Mathematically, it can be expressed as:

$$R = \frac{4 \times [A]}{(\pi \times [Major\ axis]\text{^}2)} \quad (12)\ [64]$$

Where A is the area of a primary Si particle, and the "Major axis" refers to the length of its major axis. Roundness is related to crystal geometry, and its value ranges from 0 (elongated particle) to 1 (perfect circle). As the value approaches 0.0, it indicates an increasingly elongated shape.

4.3. Average Area Fraction of Primary Si and Eutectic Structure

The average area fraction of the primary Si phase was measured using ImageJ software. Based on macroscopic images, this analysis was conducted for both the stirred and non-stirred parts. The measurement process was carried out as follows:

1. The structure consists of primary Si, and eutectic structure. The primary Si is identified and isolated using ImageJ analysis software, and its area fraction is calculated.
2. The total area fraction of all identified structural components in the microscopic image sums to 100%. Consequently, the area fraction of the eutectic structure can be determined using the equation: $A_{f(eutectic)}$= 100 - $A_{f(primary\ Si)}$. (13)

4.4. Analyse the Distribution of the Primary Si Particles and Eutectic Structure

Two parameters were evaluated to analyse the distribution of the solidified phase to assess the macro-segregation: the distribution of Si concentration by EDS, and the area fractions of the primary Si and eutectic structure along the samples.

4.4.1. Si Concentration Distribution

The distribution of Si concentration was evaluated using a Scanning Electron Microscope (SEM) equipped with an Energy-Dispersive Spectroscope (EDS). The analysis of average Si concentrations was conducted along the sample's axis of the non-stirred parts, and the sample axis was divided into 30 sections, each measuring 1 mm × 1 mm along the axis. In the transition zone between non-stirred and stirred parts, the analysis was conducted along the sample's radius at different places; it was divided into five sections of the same size along the radius. The EDS measurements were applied in stirred parts at two locations, each measuring 4 mm × 3 mm along the axis (**Figure 21**).

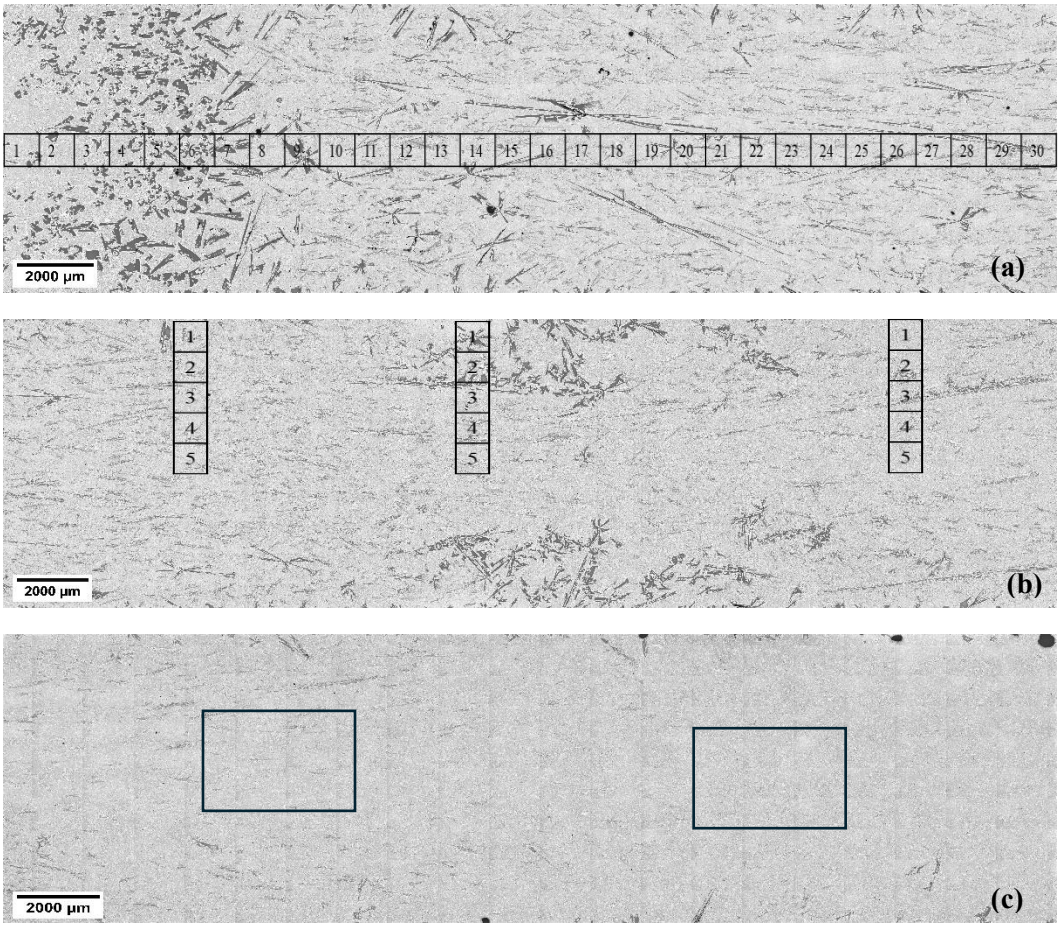

Figure 21. The macrostructure of a) the non-stirred part, b) the area of starting to stir, and c) the stirred part of the sample with s/l front velocity of 0.20 mm/s. The rectangles are the places where the EDS measurements are taken.

4.4.2. Area Fraction Measurements of Primary Si and the Eutectic Structure Along the Samples

The distribution of primary Si and the eutectic structure within the microstructure was quantified using ImageJ analysis software. To assess macro segregation, the area fractions of primary Si and the eutectic structure were measured across the samples. The micrographs of each sample were divided into different sections, covering ranges from 0–3.5 mm to 31.5–35 mm. For each section, the area fractions of primary Si and the eutectic structure were determined. This procedure was applied to both the stirred and non-stirred parts across the five samples. **Figure 22** displays the evolution of the primary Si's distribution pattern along the non-stirred and stirred parts with a growth length of 0-3.5 mm, 3.5-7 mm, 7-10.5 mm, 10.5-14 mm, 14-17.5 mm, 17.5-21 mm, 21-

24.5 mm, 24.5-28 mm, 28-31.5 mm, 31.5-35 mm respectively for the sample with s/l front velocity of 0.20 mm/s. The same procedure was applied to other samples with higher velocities.

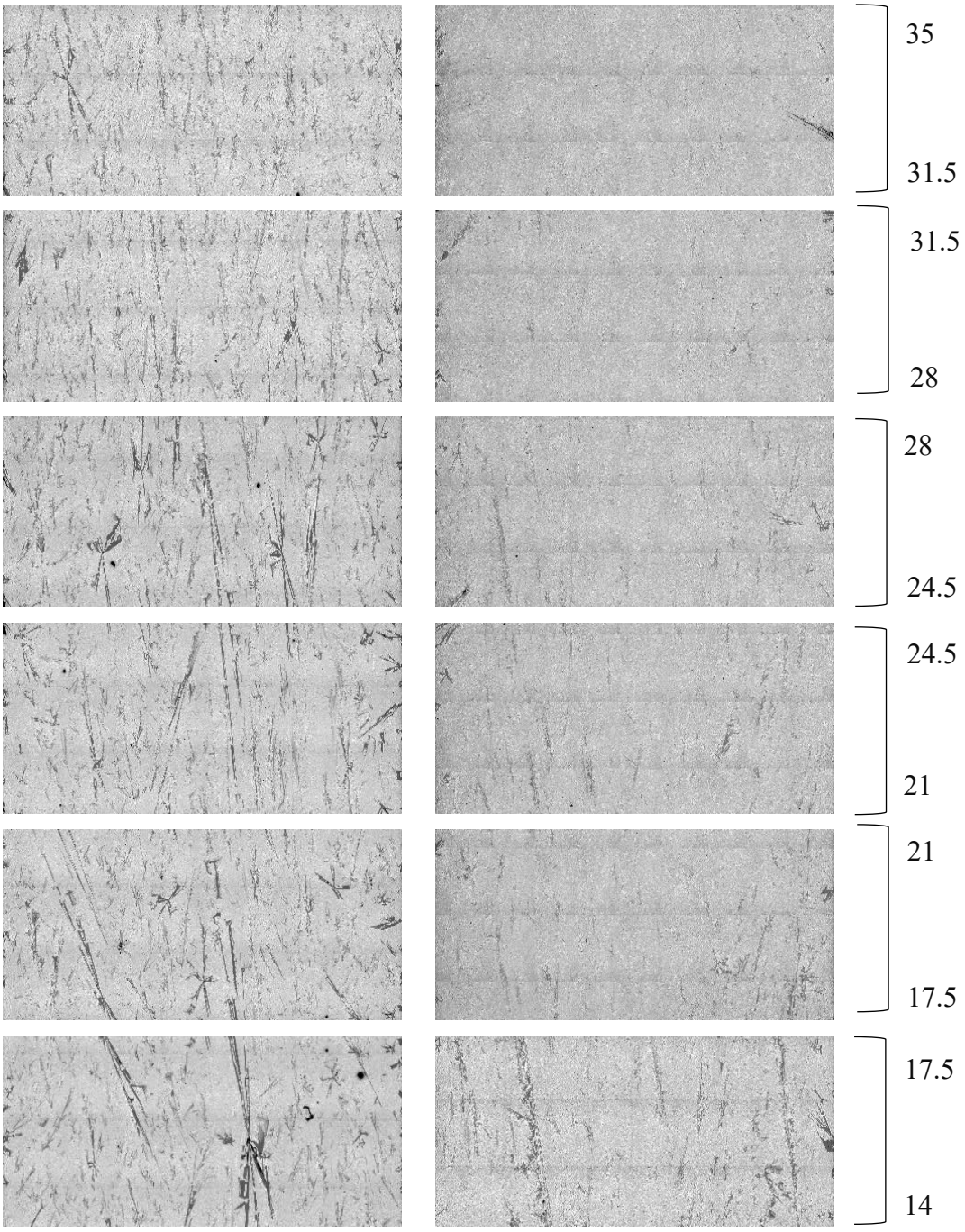

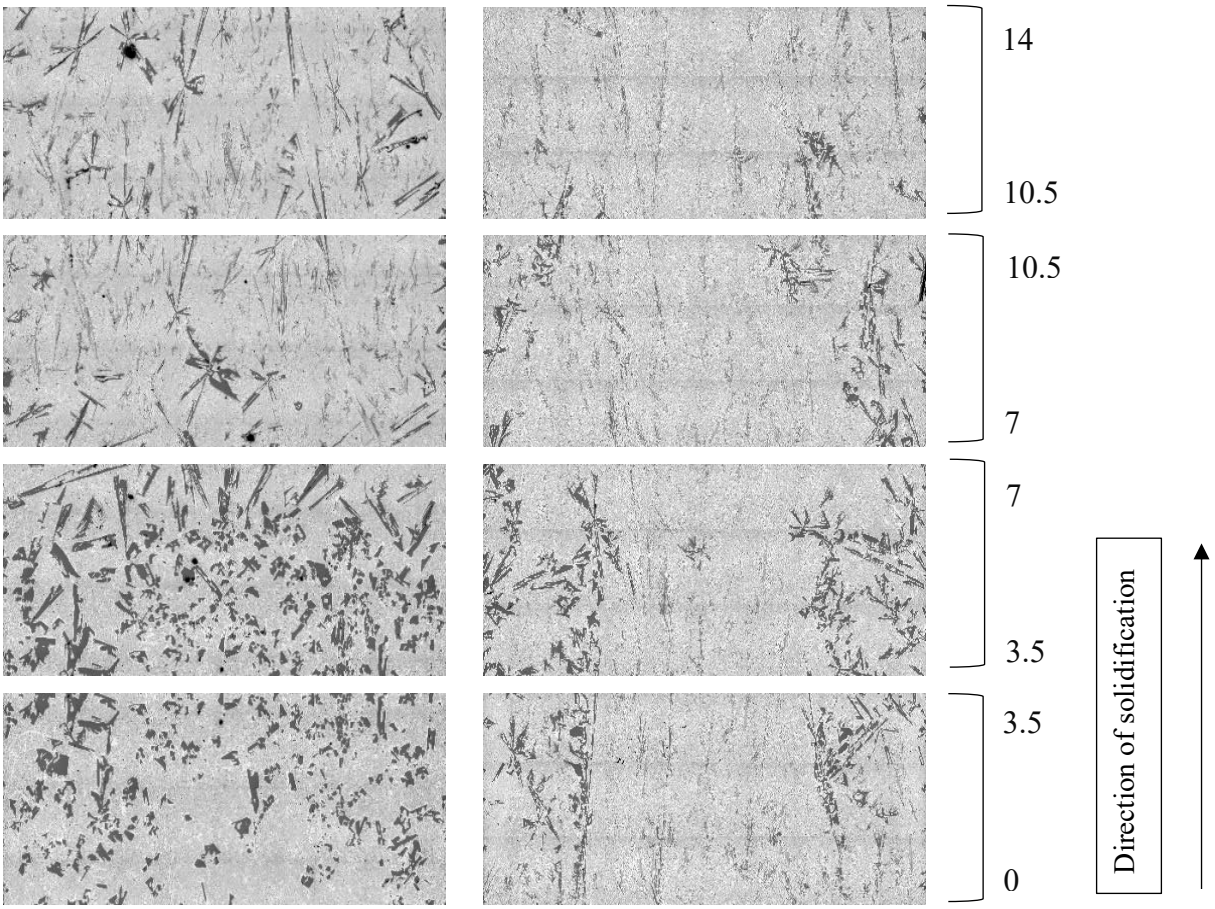

Figure 22. Evolution of the primary Si distribution along the sample with a s/l front velocity of 0.20: (a) without stirring, (b) with stirring.

5. Results and Discussion

5.1. Qualitative Analysis of Solidified Samples

The solidification of the hypereutectic Al-Si alloy starts with primary Si and finishes with Al-Si eutectic, then the solidified samples contain primary Si and Al-Si eutectic. The volume percentage of primary silicon in the Al-18wt%Si alloy is approximately 6.98%. The impact of forced melt flow induced by RMF and the s/l front velocity on the distribution evolution of primary Si was examined in Al-18 wt.% Si alloy during unidirectional solidification. **Figures 23, 24, and 25** show the longitudinal structures of the non-stirred parts, the transition zone between non-stirred and stirred parts, and the stirred parts at different front velocities. The primary Si is not uniformly distributed in the eutectic structure in all samples' stirred and non-stirred parts. This analysis unveiled an intriguing phenomenon known as macro-segregation. For non-stirred parts:

- The images show large, distinct primary Si particles scattered throughout the eutectic structure. At 0.02 mm/s, the primary Si particles are particularly prominent, indicating significant growth time and reduced cooling rates. As the velocity increases to 0.04 mm/s, the particles become slightly smaller and more evenly distributed.
- At 0.08 mm/s, the primary Si particles are noticeably smaller and more numerous than at lower velocities, suggesting increased nucleation rates due to faster cooling. By 0.20 mm/s, the particles are further refined, and the distribution becomes more homogeneous.
- The microstructure at 0.40 mm/s features very fine primary Si particles, reflecting the rapid cooling rate that limits growth and promotes a more uniform structure.

The variation in the size and distribution of primary Si particles in non-stirred parts of the samples suggests macro-segregation effects. At lower velocities, larger primary Si particles indicate regions of slower cooling and potentially higher solute concentration, while the finer particles at higher velocities suggest more uniform solute distribution due to rapid solidification. The s/l front velocity significantly affects macro-segregation. Slower velocities allow for greater solute segregation due to prolonged solidification times, while higher velocities limit this effect by promoting quicker solidification and reduced time for solute movement. At the beginning of each sample, where the first part of solidification was carried out, more primary Si were present than in the later solidified parts. It is visible that the higher the sample movement velocity, the less volume

there is and the smaller the size of the primary Si. During the solidification, a mushy zone was built up in which the concentration of Si at the s/l front was almost 18%, and it decreased toward the bottom of the mushy zone, where the eutectic was solidifying. Because of this concentration gradient, a Si diffusion occurred from the upper part of the sample to the bottom of the sample. The transferred Si atoms at the lower and colder part of the mushy zone were solidified at the existing solid Si phases. Because of this phenomenon, the concentration gradient in the mushy zone was almost constant in time, and the Si particles were growing until the eutectic front enriched them.

By the slower sample movement velocities and so by the slower v_{SL}, the diffusion had more time to perform the above-described macrosegregation, so more and bigger Si particles were observed at the bottom of the samples solidified with lower v_{SL}.

For stirred parts, the magnetic stirring induced by RMF resulted in the redistribution of primary Si particles, moving most of them away from the central axis of the sample and toward the edges. This resulted in a macrostructure where most of the primary Si solidified at the edges, while most of the eutectic matrix solidified in the central region. The RMF induces two distinct types of melt flow during solidification: azimuthal and axial flows [43], [44]. Azimuthal flow is perpendicular to the axis of the solidification direction, while axial flow runs parallel to it. These flows redistribute the primary Si particles from the central axis toward the borders of the sample [45]. As a result of the combination of the azimuthal and axial flows, the motion becomes spiral. The velocity of the melt's spiral flow is close to zero at the sample's centre channel area, and the Si concentration in the liquid doesn't reach the critical value that allows the primary Si solidification. Close to the edges of the samples, the melt flow velocity is high, which means more transported Si atoms and a higher Si concentration in the liquid, therefore, solidifying the primary Si in distinct segregation patterns (**Figure 26**). In other words, the structure of the stirred parts is likely a result of the rotating spiral flow, which moves the primary solid parts to the edges where they can swim up and melt or get stuck and grow. The stuck ones can be seen in the microstructure.

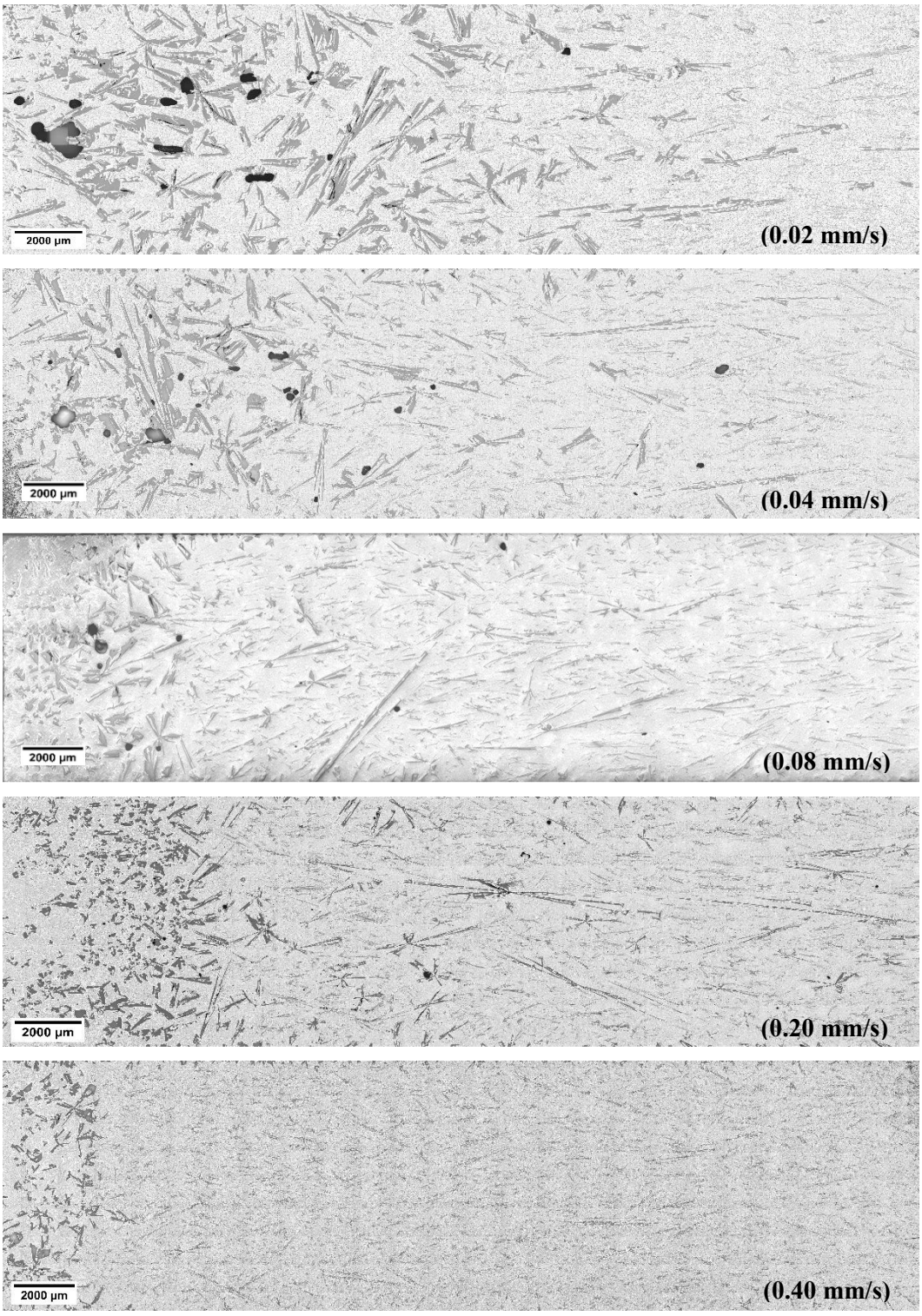

Figure 23. The macrostructure of the non-stirred parts of the Al-18 wt.% Si hypereutectic samples at different s/l front velocities: a) 0.02 mm/s, b) 0.04 mm/s, c) 0.08 mm/s, d) 0.20 mm/s and e) 0.40 mm/s.

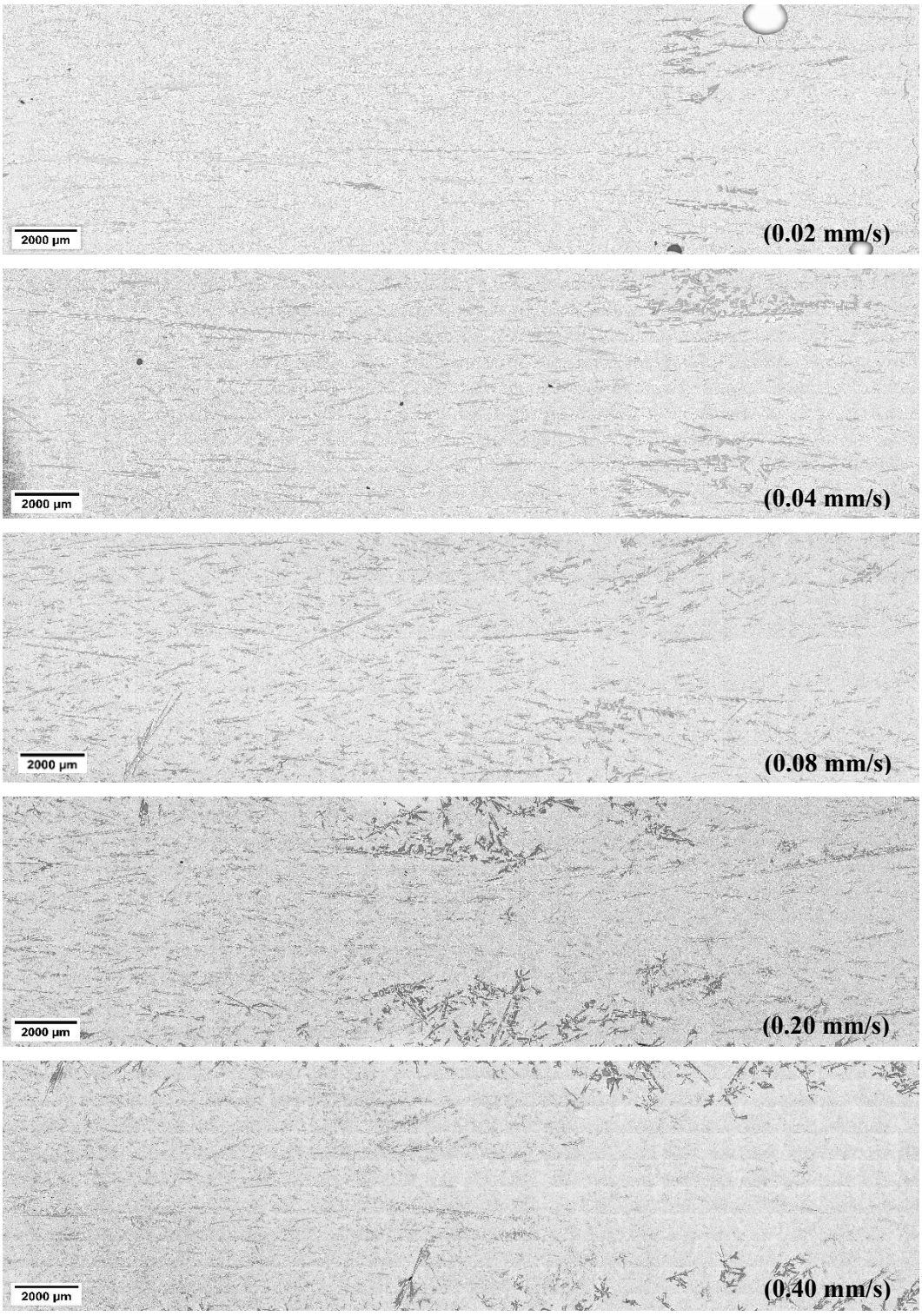

Figure 24. The macrostructure of the area of starting to stir of the Al-18 wt.% Si hypereutectic samples at different s/l front velocities: a) 0.02 mm/s, b) 0.04 mm/s, c) 0.08 mm/s, d) 0.20 mm/s and e) 0.40 mm/s.

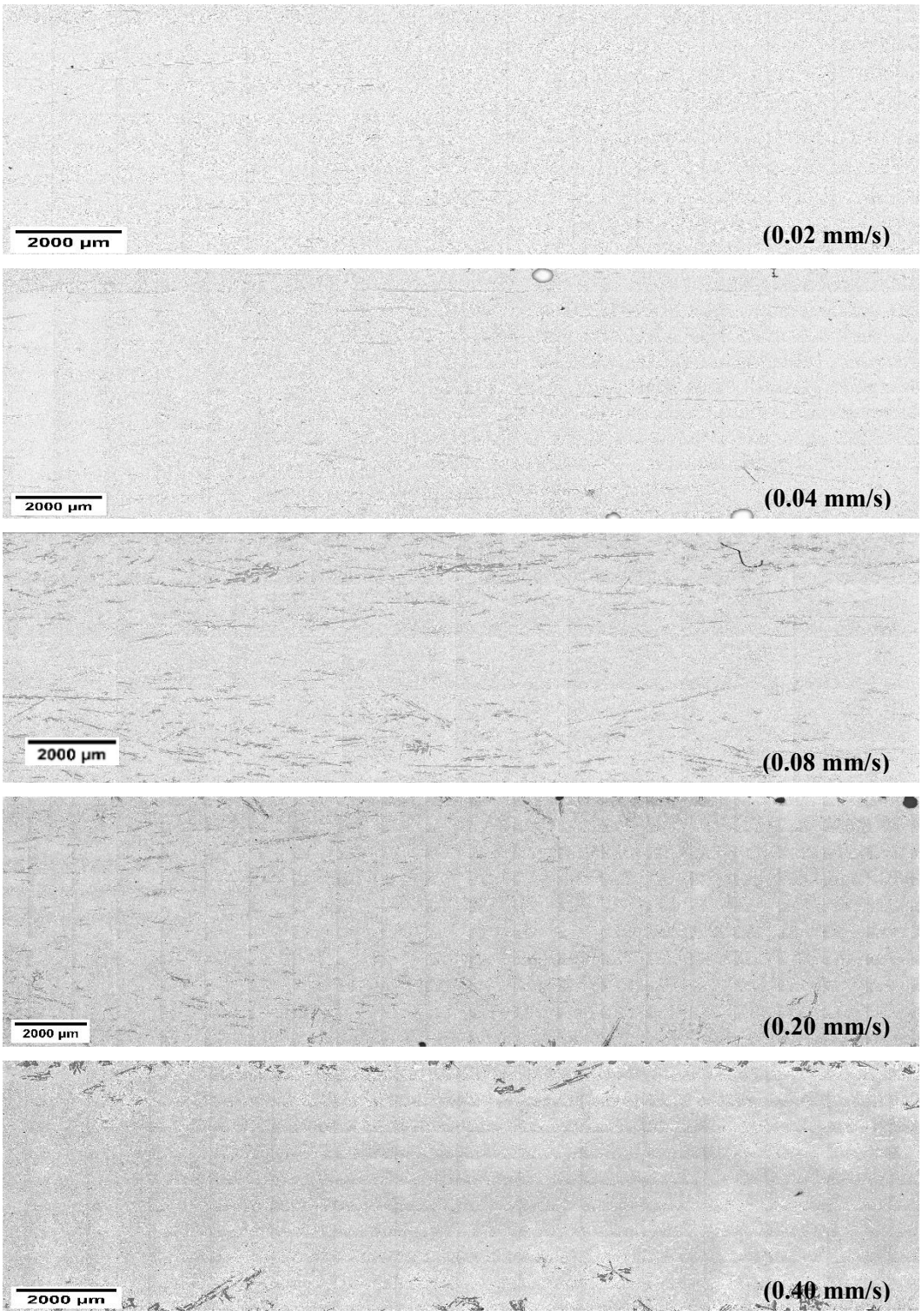

Figure 25. The macrostructure of the stirred parts of the samples at different s/l front velocities: a) 0.02 mm/s, b) 0.04 mm/s, c) 0.08 mm/s, d) 0.20 mm/s and e) 0.40 mm/s.

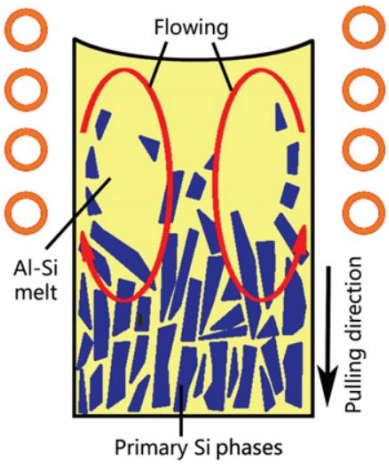

Figure 26. Schematic of the electromagnetic stirring system [65].

The samples' stirred and non-stirred parts show primary and eutectic Si particles with various shapes and sizes. Eutectic Si lamellas are depicted as plate-like structures, while primary Si particles exhibit diverse morphologies, including dendritic, polyhedral, and star-like configurations (**Figure 27)**.

- **Star-like**: This structure exhibits five arms or branches, suggesting growth along five axes (planes) originating from a common nucleus (**Figure 27. a**).
- **Polyhedral**: Polyhedral structures have multiple flat faces, indicating the presence of well-defined crystal planes during growth. This morphology appears under two subtypes: equiaxed polyhedral morphology (**Figure 27. b**) and elongated polyhedral or, as known in the literature, coarse plate-like (**Figure 27. c**).
- **Dendritic**: Dendritic structures are characterised by branching, tree-like patterns. The dendritic morphology appears under two subtypes: equiaxed dendritic shape (**Figure 27. d**) and elongated dendritic shape (feathery) (**Figure 27. e**). Feather-like configurations imply delicate, elongated structures resembling feathers.

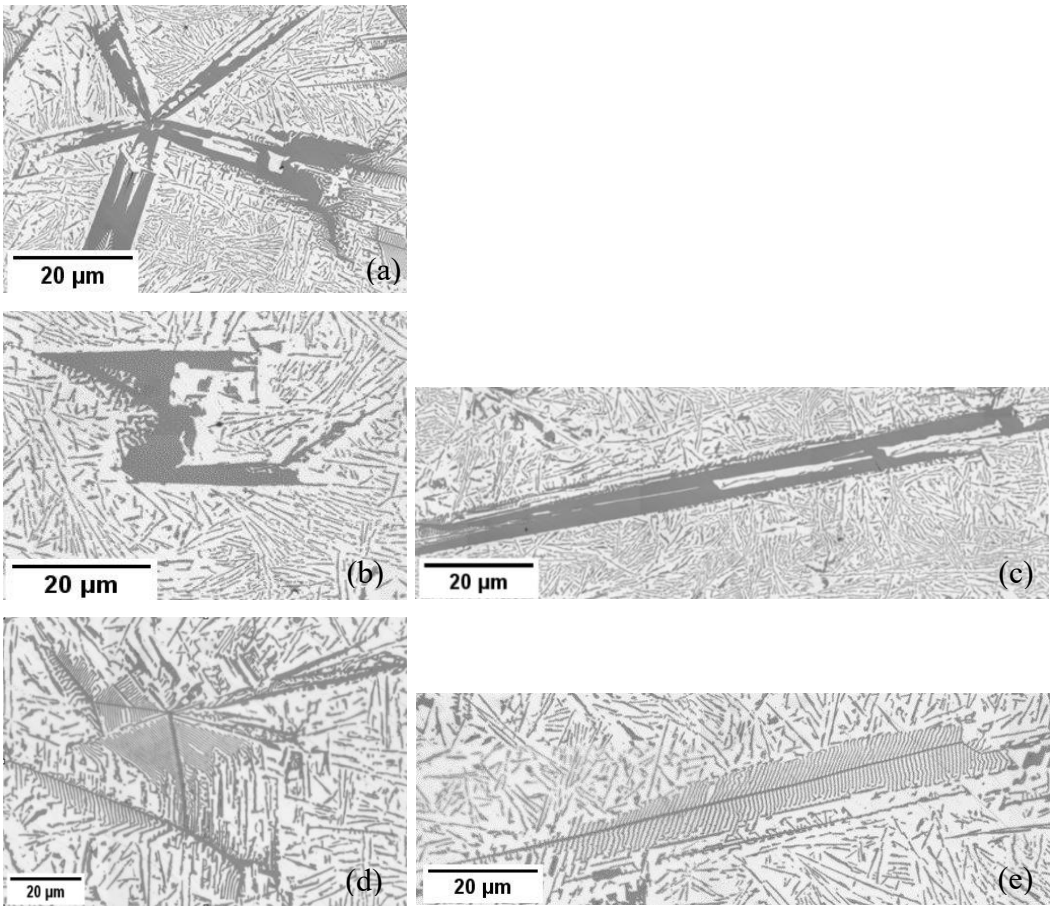

Figure 27. The morphologies of primary Si in the studied hypereutectic alloy: (a) solid star-like structure, (b) polyhedral structure, (c) elongated polyhedral structure (plate-like), (d) equiaxed dendritic structure, (e) elongated dendritic structure (feather-like).

Despite qualitative observations, accurately describing differences in morphology, size, and distribution of primary Si in stirred and non-stirred parts remains challenging due to their irregular shape. Image analysis techniques would be beneficial for more precisely characterizing these differences.

5.2. Quantitative Analysis of Solidified Samples

5.2.1. Length of Eutectic Lamellas

Length measurements were applied by measuring the Ferret diameter of each Si eutectic lamella projection as outlined in the measurement method chapter, heading (5.1.1. The length of the eutectic lamellas). The lengths of eutectic Si lamellas were determined by categorizing their lengths into ranges from (0-10) to (90-100) µm. **Figure 28** shows the percentages of the eutectic lamellas in both the stirred and non-stirred parts of the sample solidified at the eutectic front

velocity of 0.02 mm/s. Although only this sample was displayed, the trend is consistent across all samples (Appendix 9.2). The results indicate that at the velocity of 0.02 mm/s, the percentage of eutectic Si lamellas decreases as the lamella length increases in both the stirred and non-stirred parts**.** The same trend was observed at other applied eutectic front velocities.

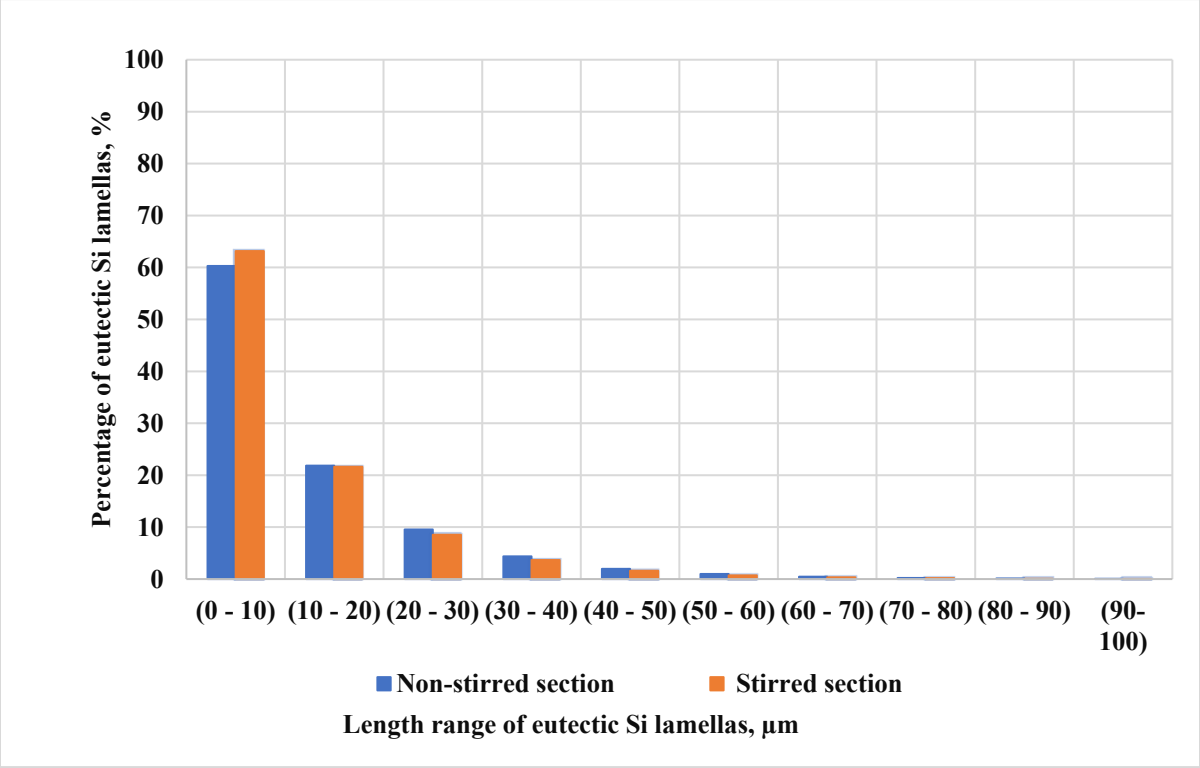

Figure 28. The percentage of the eutectic Si lamellas as a function of their length range in the stirred and non-stirred parts of the sample that solidify at v_e = 0.02 mm/s.

The eutectic Si lamellas were categorized into two groups: fine lamellas, with lengths less than 10 µm, and coarse lamellas, with lengths greater than 10 µm. This classification was applied to both the stirred and non-stirred parts of all samples. **Figure 29** illustrates the percentage of the eutectic Si lamellas as a function of eutectic front velocity in both parts**.** The microstructure of the hypereutectic Al-Si alloys was strongly affected by increasing eutectic front velocity and the application of RMF. The results show that for all eutectic front velocities, the percentage of fine eutectic Si lamellas was higher than that of coarse lamellas in both stirred and non-stirred parts. Furthermore, increasing the eutectic front velocity from 0.02 mm/s to 0.40 mm/s led to a higher percentage of fine lamellas and a lower percentage of coarse lamellas in both parts. This is attributed to the shorter solidification time at higher eutectic front velocities, which results in a

finer microstructure. In the non-stirred parts, the percentage of fine eutectic lamellas increases from 60.3% to 86.4%, following the expression (Lamellas % = 1126.8v_e^3 - 978.57v_e^2 + 288.33v_e + 55.577), while in the stirred parts it rises from 63.2% to 87.9%, described by (Lamellas % = 1108.2v_e^3 - 938.42v_e^2 + 269.53v_e + 59.299), where v_e denotes the eutectic front velocity. Correspondingly, coarse lamellas decrease from 39.7% to 13.6% in non-stirred parts, fitting (Lamellas % = -9.024ln (v_e) + 4.0997), and from 36.8% to 12.1% in stirred parts, following (Lamellas % = -1108.2v_e^3 + 938.42v_e^2 - 269.53v_e + 40.701).

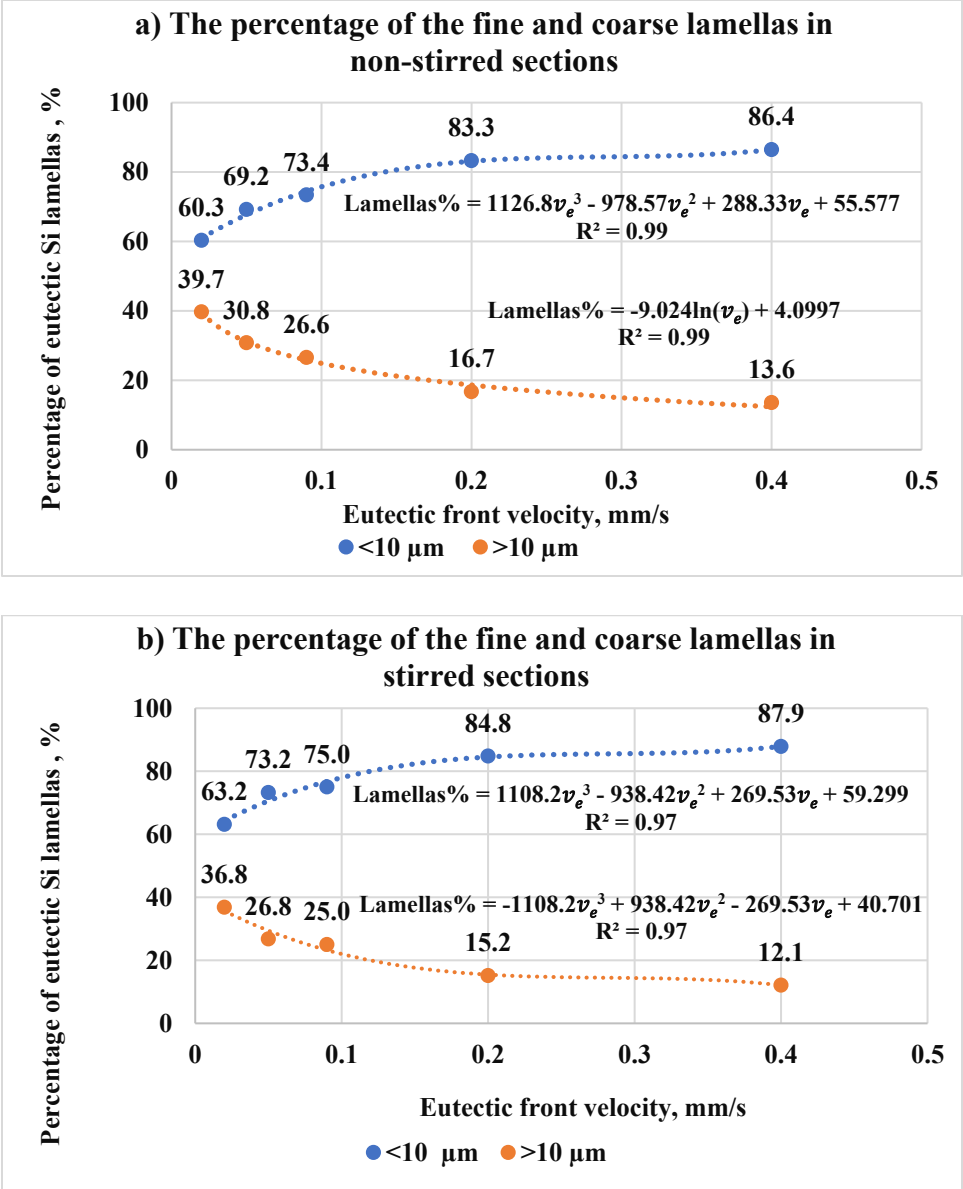

Figure 29. the percentages of the eutectic Si lamellas as a function of front velocity in both a) non-stirred and b) stirred parts of the five samples.

It has also been found that stirring the melt by RMF increased the percentage of fine lamellas and decreased the percentage of coarse lamellas compared to the non-stirred parts. This confirms that RMF leads to the refinement of the length of eutectic lamellas in Al-18wt% Si samples.

The combination of increasing eutectic front velocities and the use of RMF during unidirectional solidification has been shown to synergistically affect the refinement of the eutectic structure in hypereutectic alloys. Increasing the eutectic front velocities and using RMF promote the formation of a fine eutectic structure due to the limited diffusion of the solute atoms, resulting in a higher density of nucleation sites for the eutectic structure, resulting in a highly refined microstructure.

The size refinement may also be linked to the increased solidification rate, driven by the transport of cooled liquid from the cold regions to hotter regions through RMF-induced fluid flows. It is well established that finer structures form under higher undercooling conditions [66].

5.2.2. The angle of the Eutectic Lamellas

The angles of the eutectic lamellas with the solidification direction were determined as the Ferret angle. **Figure 30** shows the angle distribution of all eutectic Si lamellas as a function of eutectic front velocity in the hypereutectic alloy for both stirred and non-stirred parts.

The analysis highlights the impact of eutectic front velocity on the angle distribution. As the front velocity increases, there is a noticeable decrease in the percentage of eutectic Si lamellas with angles less than 25°. Conversely, there is an increase in lamellas with angles greater than 25°. This suggests that higher velocities cause a shift toward greater angles, indicating a more varied orientation distribution.

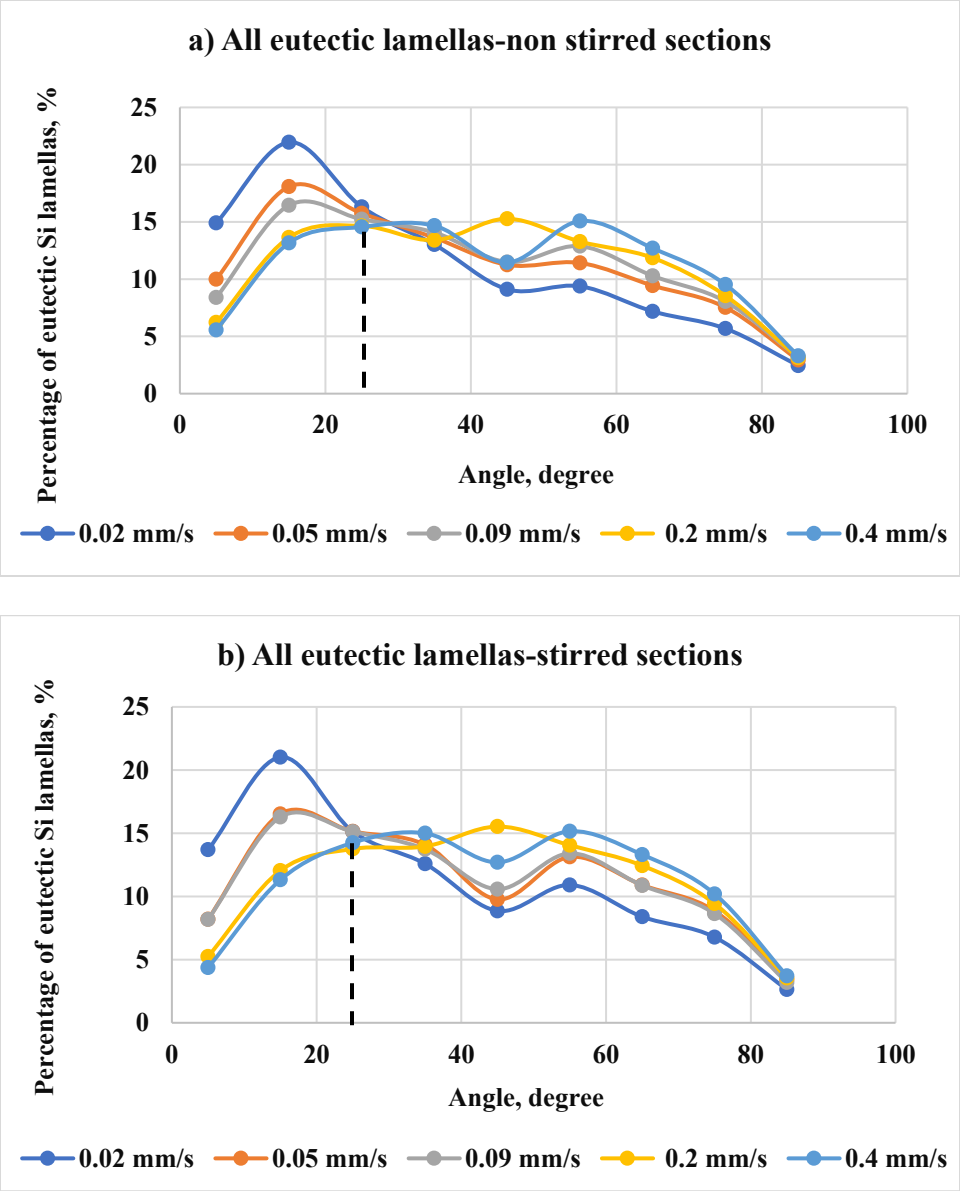

Figure 30. The angle distribution of all the eutectic Si lamellas as a function of eutectic front velocity in the hypereutectic alloy for the a) non-stirred parts and b) stirred parts.

The front velocity plays a crucial role in the solidification process. It determines the rate at which the eutectic lamellas grow and influences their angle. The orientation of the eutectic lamellas was determined by categorizing Si lamellas lengths into four groups: 0–2 μm, 2–5 μm, 5–50 μm, and >50 μm, followed by computing the angle distribution as mentioned in the measurement method chapter, heading (5.1.2. The angle of the eutectic lamellas**)**. **Figure 31** shows the angle distribution of the eutectic Si lamellas with lengths 0-2 μm as a function of eutectic front velocity in stirred and non-stirred parts of the samples. The results show that the highest percentage of eutectic lamellas measuring 0–2 μm in length tends to align at a 45º angle to the direction of solidification across all the eutectic front velocity values in the stirred and non-stirred parts. As the front velocity increases, the percentage of the eutectic lamellas whose length is between (0–2 μm) decreases at its preferred angle in both stirred and non-stirred parts.

On the other hand, RMF has been shown to affect the orientation of the eutectic lamellas significantly. RMF can induce a rotating flow in the melt, which can modify the solidification front and, consequently, affect the orientation of the eutectic lamellas. Comparing between non stirred and stirred parts, it has been observed that when RMF is applied, the eutectic lamellas' maximum percentage (0–2 μm) at its preferred angle (45º) decreases. The rest of the lamellas in this length category are oriented at various angles. The trend was observed for all values of eutectic front velocity.

Inducing melt flow by RMF with increasing the front velocity during solidification decreases the lamellas' maximum percentage (0–2 μm) at its preferred angle (45°). It increases the angles' diversity more compared to the non-stirred sections. This means that applying RMF with increasing the front velocity during solidification improves the angle distribution of the eutectic Si lamellas compared to the non-stirred parts.

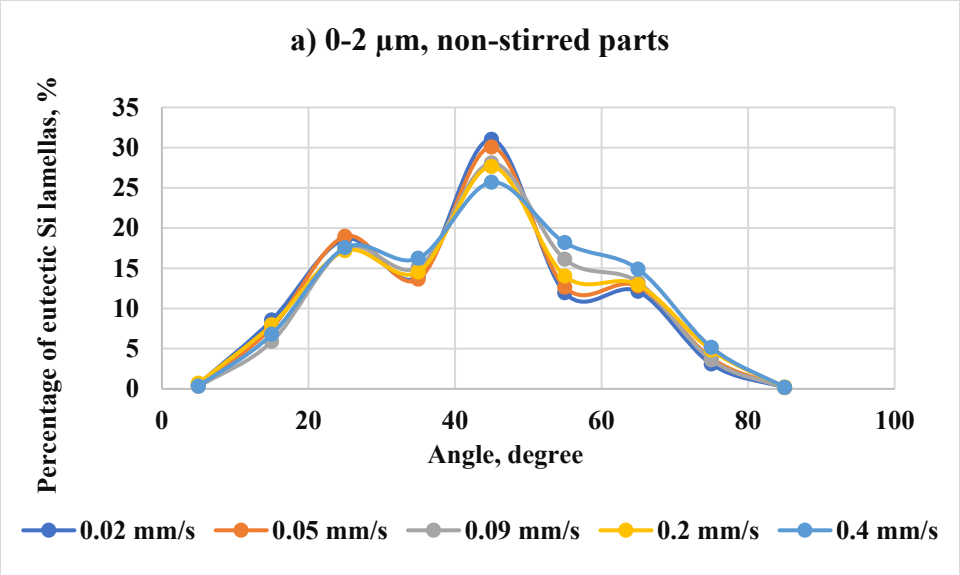

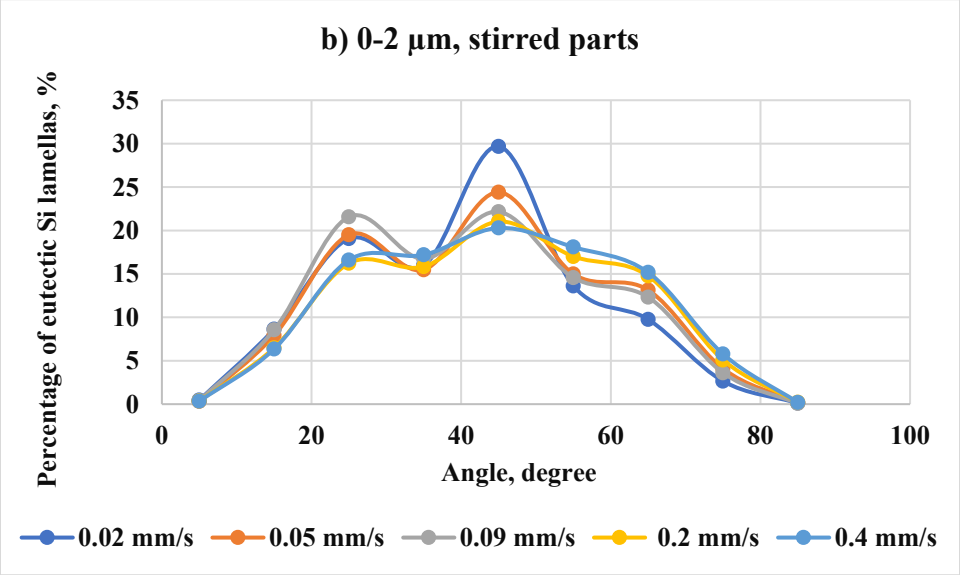

Figure 31. The angle distribution of the eutectic Si lamellas with length 0-2 µm as a function of eutectic front velocity in both stirred and non-stirred parts of the samples.

As previously noted, the preferred angle orientation for eutectic lamellas (0–2 µm) is 45°. Through the same measurement approach, we evaluated the preferred angles across the other different size categories. Notably, we observed that for eutectic lamellas (2–5 µm), (5–50 µm), and for lamellas with lengths greater than 50 µm, the preferred angle orientation is 15, 15, and 5, respectively, at all the applied values of the eutectic front velocity in the stirred and non-stirred parts. The same happened with these categories (2–5 µm), (5–50 µm), and >50 µm; also, increasing the eutectic

front velocity and applying RMF during solidification did not alter the preferred angle of the lamellas, but it did reduce the maximum percentage of lamellas at these preferred angles (**Figure 32**). This reduction is accompanied by an increase in the percentage of lamellas at other angles.

As the eutectic front velocity increases, solidification becomes faster, which reduces the time available for individual eutectic Si lamellas to grow. This prevents many lamellas from maintaining their preferred growth direction before being cut off or blocked by surrounding features or the moving front. Additionally, higher front velocity promotes more nucleation sites, causing the newly formed eutectic lamellas to orient variably and increasing the overall angular diversity.

Based on these findings, it was observed that eutectic lamellas that are more parallel to the direction of solidification have a higher likelihood of growing to a greater length (**Figure 33**).

The RMF primarily influences Si lamellar angle distribution through induced fluid flows during solidification. The primary azimuthal flow involves fluid rotation around the sample axis. The secondary meridional flow features two toroidal vortices forming in the r–z plane. Radial flow occurs as Taylor–Grotler vortices meet the mushy zone, leading to fluid moving radially. These flows cause the Si lamellas to orient variably, increasing angle diversity.

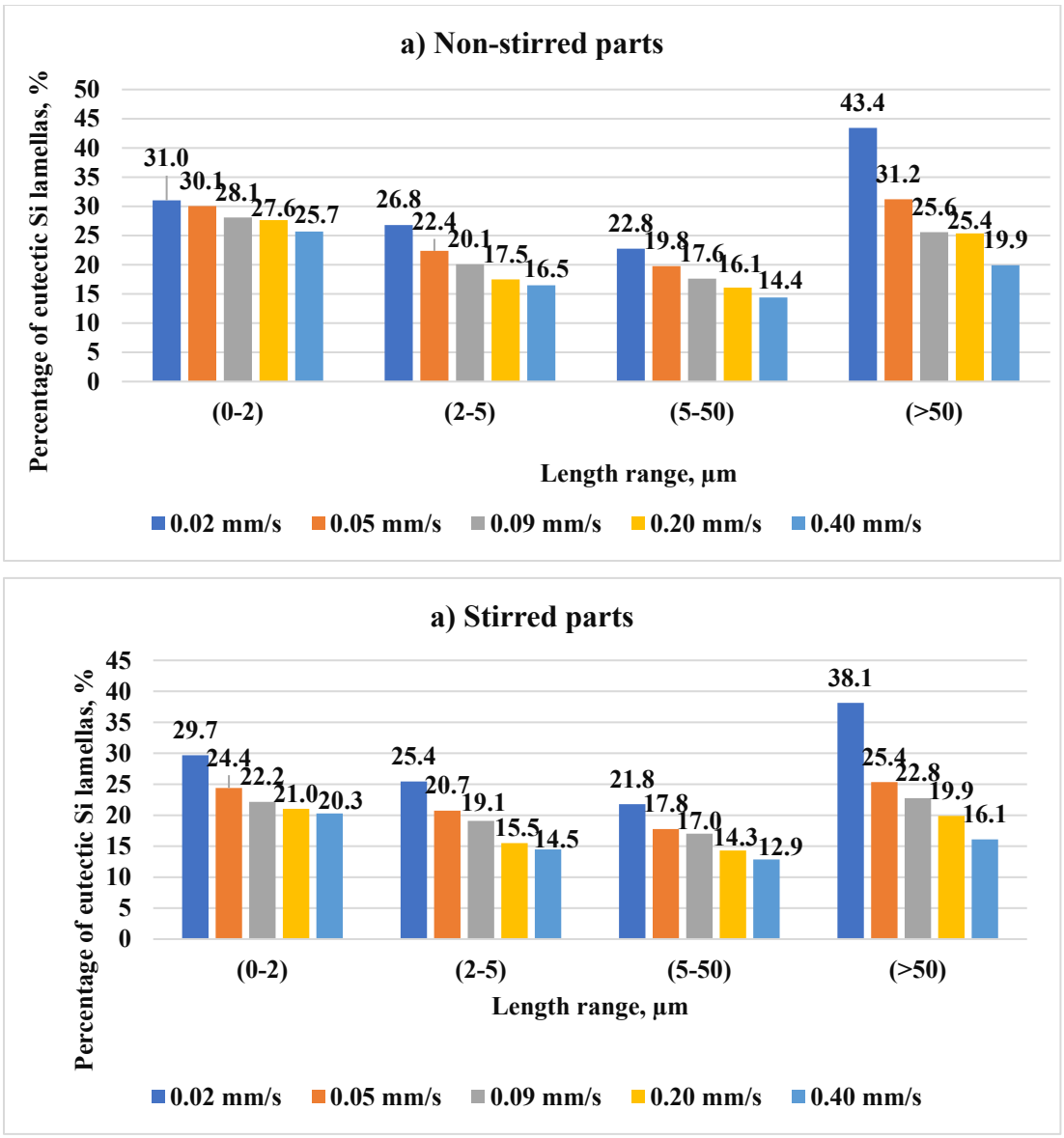

Figure 32. The highest percentages of lamellas oriented at the preferred angle for different length ranges, 0-2 µm, 2-5 µm, 5-50 µm, and > 50 µm at different front velocities: 0.02, 0.05, 0.09, 0.2, and 0.4 mm/s in the a) non-stirred parts and b) stirred parts of the samples.

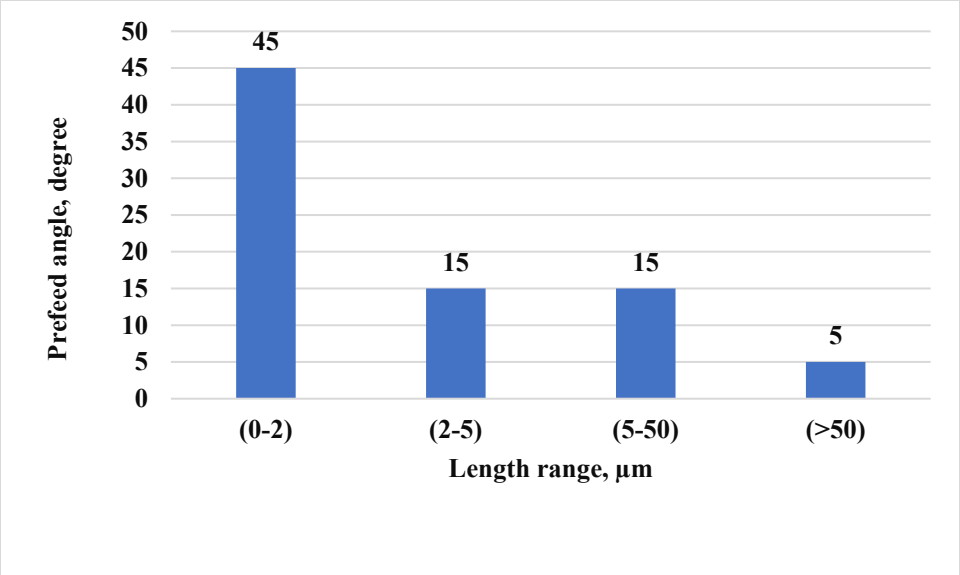

Figure 33. The preferred angle of the eutectic Si lamellas in the hypereutectic alloy for different length ranges.

5.2.3. Eutectic Inter-lamellar Distances (λ)

The results of this study provide important insights into the effects of eutectic front velocity and RMF on the eutectic interlamellar distances in hypereutectic Al - 18 wt.% Si alloy. As noted in the measurement method chapter, heading (5.1.3. The eutectic inter-lamellar distance**)**, the interlamellar distances were measured using the specific perimeter method. **Figure 34** shows the measured eutectic interlamellar distances as a function of eutectic front velocity in both the stirred and non-stirred parts. The study found that increasing eutectic front velocity decreased the distance between the eutectic lamellas in both parts.

Additionally, applying RMF during solidification further reduced the eutectic interlamellar distance compared to the non-stirred parts. These findings confirm the refinement effect of RMF on the length of eutectic Si lamellas in Al-18wt% Si hypereutectic alloy samples. The combination of increasing the eutectic front velocities and using RMF during unidirectional solidification has been shown to have a synergistic effect on decreasing the eutectic interlamellar distance and refinement of the eutectic structure in hypereutectic alloys.

These results have significant implications for materials science and engineering, as the distance between eutectic lamellas is a key microstructural parameter that can impact the mechanical properties of alloys. A smaller lamellar distance is associated with improved mechanical

properties, such as increased strength and microhardness. These results agree with the results obtained by researcher Koçak and his colleagues [49], reinforcing the understanding of the relationship between front velocity and interlamellar distances in metallic alloys.

The data in **Figure 34** provide the following equations:

- For non-stirred parts: $\lambda = 14.1v^{-0.31}$ (for constant G)
- For stirred parts: $\lambda = 12v^{-0.31}$ (for constant G)

The λ value exhibits an exponential dependence on front velocity, with an exponent of -0.31. This exponent is higher than the predicted value of -0.50 according to the J-H eutectic theory [40]. It is also smaller than the values of -0.49 and -0.51 obtained by Koçak. [49] for Bi-Pb eutectic alloy, and Kaya and his colleagues. [67] for Al-Ni eutectic alloy. These differences could be attributed to the variations in solidification conditions and compositions. Furthermore, these differences may arise from structural discrepancies, where the hypereutectic Al-18 wt.% Si alloys exhibit an irregular eutectic structure compared to other alloys.

Eutectic growth at the eutectic front features atom diffusion, where A atoms are expelled from the β phase and B atoms from the α phase, creating a diffusion boundary layer. This process directly affects the inter-lamellar distances (λ), with larger diffusion ranges resulting in greater distances. Increasing the velocity of the eutectic front reduces the time available for atom diffusion, which in turn decreases the eutectic interlamellar distance.

Li [68] noted in his research that solute convection is weak during eutectic unidirectional solidification. He proposed a new mechanism to explain the impact of a high magnetic field on the diffusion coefficient in the Al-Si eutectic alloy. The alloy consists of α-Al and Si phases in a lamellar structure, where Al atoms are expelled by the growing Si phase and Si atoms by the growing α-Al phase. This results in a concentration gradient of Si in front of the α-Al phase and depletion in front of the Si lamellae. Due to the magnetic properties of Si (diamagnetic) and Al (paramagnetic), a gradient magnetic field forms in these layers, exerting a magnetic force on solutes at the solid/liquid interface, thus inhibiting Si and Al interdiffusion. Consequently, this magnetic influence slows atomic diffusion, reducing the diffusion coefficient (D) and the average inter-lamellar distance λ.

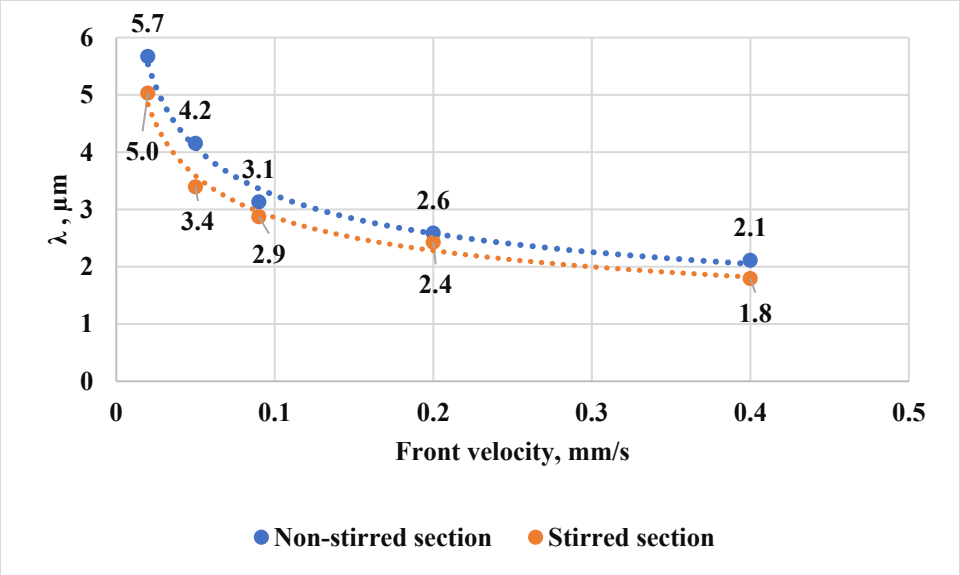

Figure 34. Distance between the eutectic Si lamellas (λ) as a function of front velocity in the stirred and non-stirred parts of the samples.

The results of the eutectic structure agree with the results of Al-Omari [42]. Their experimental research shows that the microstructure of Al–12.6-wt%-Si eutectic alloys changes noticeably when RMF is applied during solidification. Specifically, RMF improves the eutectic structure by decreasing the length of the eutectic Si lamellas, decreasing interlamellar distances, and increasing the variety of orientations of the Si lamellas angle.

The observed effects of eutectic front velocity and RMF on eutectic structure can be explained by their influence on the growth process during solidification, where increasing velocity or applying RMF during solidification lead to accelerated arms growth and competition with each other for space, enhanced natural convection, and limited solute diffusion in front of the eutectic interface, resulting in a refined microstructure with closer eutectic lamellas and increased lamellas diversity.

5.2.4. Size of Primary Si Particles

As noted in the measurement method chapter, heading (5.2.1. Size factor), ImageJ analysis software was used to quantify the size and distribution of the primary Si in the microstructure. The equivalent diameter of each primary Si particle was used to measure the size of primary Si. The measurements were analysed by classifying the primary Si equivalent diameters into ranges from (0-200) to (800-1000) µm. **Figure 35** shows the percentages of the primary Si in stirred and non-stirred parts of the sample that solidified at the s/l front velocity of 0.02 mm/s. While only one

sample is shown, trends are consistent across all (Appendix 9.4). Results show that at 0.02 mm/s velocity, the primary Si percentage decreased with increasing size in both stirred and non-stirred regions**.** The same trend was observed at higher velocities.

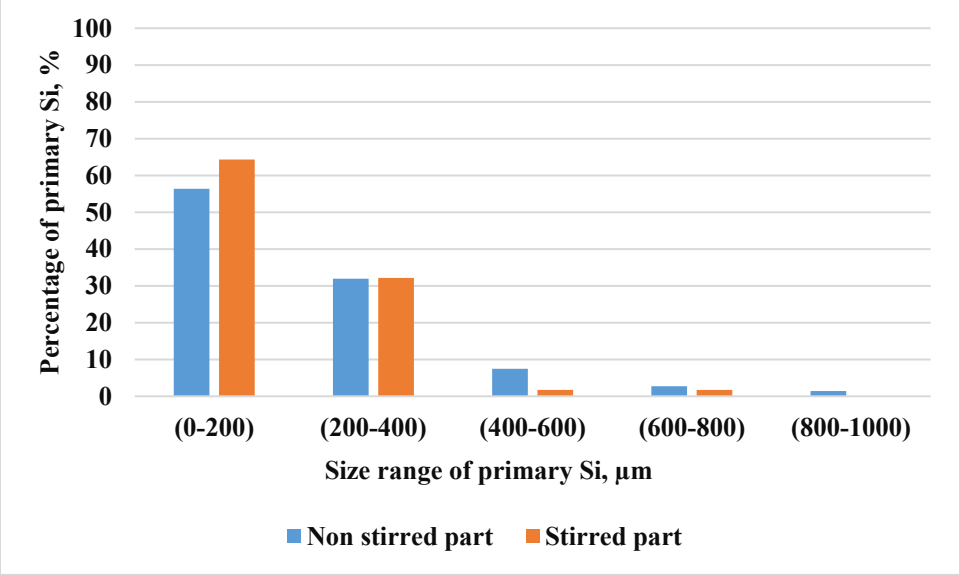

Figure 35. The percentage of primary Si as a function of their size range in the stirred and non-stirred parts of the sample that solidify at v_{SL}=0.02 mm/s.

For deeper insight, the primary Si particles were classified into two categories: fine primary Si measuring less than 200 µm and coarse primary Si exceeding 200 µm in size. The threshold of 200 µm was chosen based on the observed average equivalent diameter of primary Si particles at various s/l front velocities. This classification was applied to both stirred and non-stirred parts across all samples. **Figure 36** illustrates the distribution of primary Si relative to s/l front velocity, showcasing a notable trend: as velocity increases, the percentage of fine primary Si rises while that of coarse primary Si diminishes in both stirred and non-stirred parts, indicating the refinement of primary Si with heightened s/l front velocity in stirred and non-stirred parts. This phenomenon arises from the shortened solidification time at higher velocities, facilitating a finer microstructure.

Increasing the s/l front velocity generally leads to a higher cooling rate. Typically, the growth of primary Si occurs as silicon atoms attach to the surfaces of existing primary Si. Thus, the diffusion of silicon atoms is crucial for growing primary Si. As the cooling rate increases, it becomes more difficult for silicon atoms to diffuse, which substantially restricts the growth of primary Si. Consequently, with an increase in the cooling rate, the size of the primary Si is reduced.

In the non-stirred parts, the percentage of fine primary Si increases from 56.4% to 82.2%, following the expression (Primary Si% = 7.5578ln(v_{SL}) + 84.552), while in the stirred parts it rises from 64.3% to 69.4%, described by (Primary Si% = 1.8517ln(v_{SL}) + 71.791), where v_{SL} is the s/l front velocity. Correspondingly, coarse primary Si decrease from 43.6 to 17.7% in non-stirred parts, following (Primary Si% = -7.584ln(x) + 15.364), and from 35.7% to 30.6% in stirred parts, following (Primary Si% = -1.852ln(v_{SL}) + 28.209).

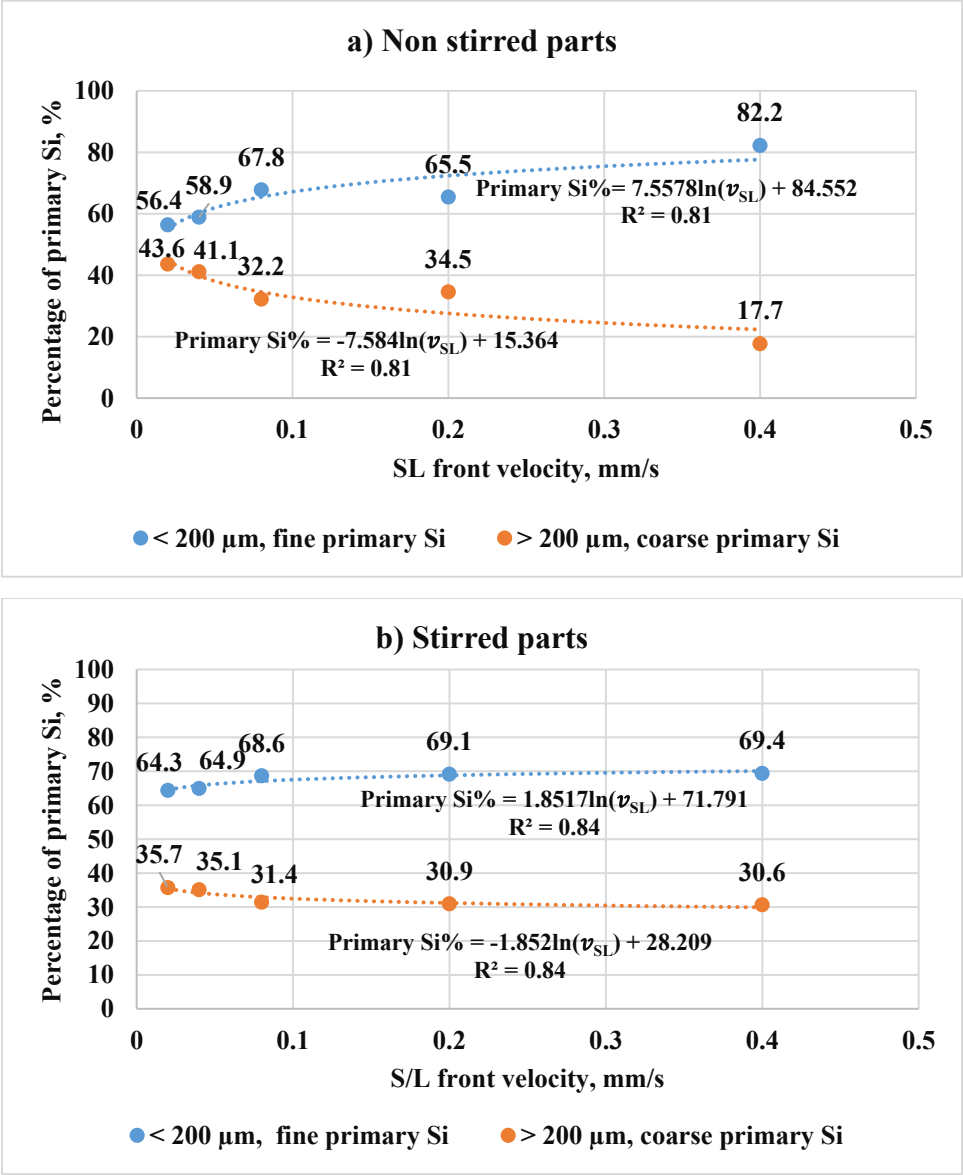

Figure 36. The percentages of the primary Si in terms of their size as a function of s/l front velocity in both the a) non-stirred and b) stirred parts of the five samples.

5.2.5. Shape of Primary Si

The shape factors, including circularity and roundness, were assessed for ten particles of each primary Si shape, including polyhedral, plate-like star-like, equiaxed dendritic, and elongated dendritic shape, followed by the calculation of their respective averages and standard deviation (**Table 2**).

Table 2. Dimensionless shape factors of various shapes of primary Si.

Shape Description	Shape Description	Average of circularity	Standard deviation	Average of roundness	Standard deviation
Polyhedral	Equiaxed polyhedral	0.59	0.1	0.58	0.2
	Elongated polyhedral (Plate like)	0.22	0.1	0.07	0.0
Dendritic	Equiaxed dendritic	0.08	0.0	0.33	0.1
	Elongated dendritic (Feathery)	0.05	0.0	0.07	0.0
Star like	Star like	0.12	0.0	0.43	0.2

Numerous trends can be identified from the data in Table 2. These trends will be analysed individually based on each shape descriptor.

5.2.5.1. Classification and Evolution of Primary Si Morphologies by Circularity

Circularity, expressed by Equation 11, hinges on the particle's perimeter; increasing the perimeter reduces circularity and enhances roughness. Consequently, as a shape becomes smoother and more rounded, circularity tends towards one, exemplified by polygon shapes with a circularity greater than 0.2, and to a lesser extent, star shapes exhibit circularity between 0.1 and 0.2. Conversely, as a shape becomes less round or smoother, circularity approaches zero, demonstrated by dendritic shapes with the highest perimeter with circularity below 0.1 (**Table 2**).

For the analysis, primary Si particles were categorized into three groups based on their circularity: dendritic particles (circularity < 0.1) representing the roughest; star-like particles (0.1 < circularity < 0.2) less rough; and polyhedral particles (circularity > 0.2), the smoothest. These categories were analysed across stirred and non-stirred parts of all samples. **Figure 37** illustrates the variation in the percentages of these primary Si types as a function of front velocity in stirred and non-stirred

parts. Observations indicate that an increase in front velocity from 0.02 to 0.4 mm/s decreases the percentages of dendritic primary Si particles from 51.4% to 15.7% while increasing the percentage of star-like particles from 34.6% to 73.5% in non-stirred parts. The percentage of polyhedral seems almost constant and it is around 12 ± 2. The percentages of dendritic, star-like, and polyhedral Si in the stirred parts appear relatively constant across varying front velocities, except at the highest velocity. Minor fluctuations are observed, but the overall trend indicates stability in the distribution of primary Si shapes.

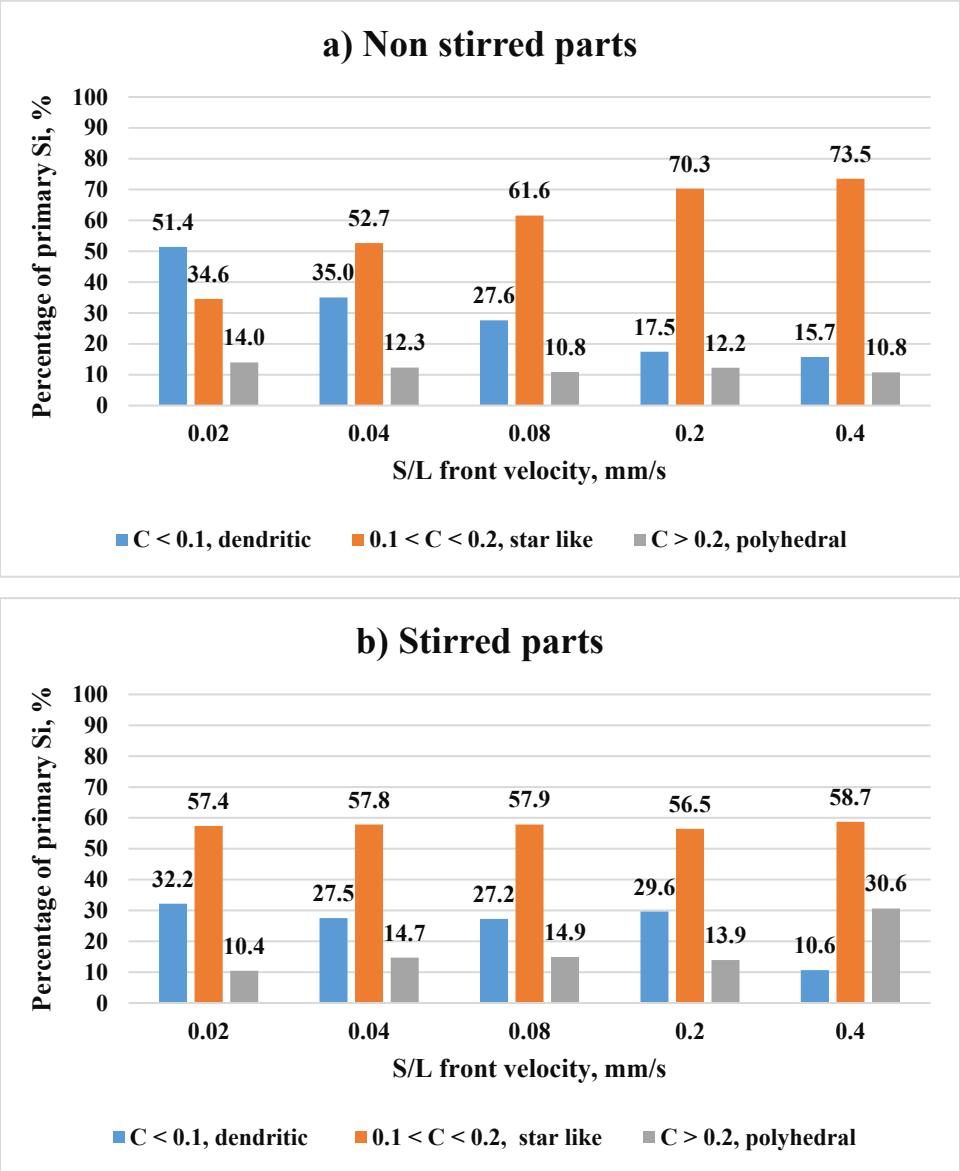

Figure 37. The percentages of the primary Si in terms of their circularity as a function of s/l front velocity in both the a) non-stirred and b) stirred parts of the five samples.

As the front velocity increases, the cooling rate change, affecting the way Si particles form. Higher velocities promote rapid solidification, which can suppress the growth of dendritic structures while favouring the formation of star-like particles. Dendritic growth requires a slower cooling, which is disrupted at higher front velocities, leading to a reduction in dendritic Si.

Researchers Xu and Jiang [13] suggest that the size of Si–Si clusters influences the formation of primary silicon morphologies. Larger Si–Si clusters promote the nucleation of irregular primary Si, while smaller clusters favour the formation of more regular primary Si nuclei. Based on the present investigation, it can be reasonably concluded that larger Si–Si clusters are favourable for forming dendritic primary Si, whereas smaller Si–Si clusters are more conducive to forming star-like primary silicon nuclei. An increase in the solid/liquid (s/l) front velocity decreased the percentage of larger Si–Si clusters, resulting in a reduced proportion of dendritic primary silicon. Conversely, the percentage of smaller Si–Si clusters increased, leading to a higher proportion of star-like primary silicon.

Based on the present results, an increase in the solid/liquid (s/l) front velocity in the stirred regions does not appear to affect the morphologies of primary silicon in the investigated range. The distribution of different primary silicon morphologies remains nearly unchanged. It is suggested that the morphology of primary silicon in the solid state is closely linked to the nucleation process in the liquid melt. During solidification, regardless of variations in front velocity, a consistent liquid structure leads to the formation of similar primary silicon nuclei in the melt, resulting in minimal morphological differences. Therefore, it can indicate that different s/l front velocities in the stirred parts have hardly any effect on the nucleation of different morphologies of primary Si from the liquid melt. In other words, increasing front velocity in stirred parts have hardly effect on the morphologies of primary Si in the solid state.

5.2.5.2. Classification and Evolution of Primary Si Morphologies by Roundness

As expressed by Equation 12, roundness hinges on the particle's maximum diameter. As an object becomes more elongated or less circular, its roundness value tends toward zero. This is exemplified by elongated polyhedral (plate-like) shapes and elongated dendritic (feathery) shapes, which exhibit roundness values < 0.1. Conversely, objects with highly rounded forms approach a roundness value of one. This is illustrated by equiaxed polyhedral, star, and equiaxed dendritic shapes with roundness values > 0.1 (**Table 2**).

The values of roundness help us to distinguish the elongated dendritic particles ($C < 0.1 + R < 0.1$) from the equiaxed dendritic particles ($C < 0.1 + R > 0.1$) and the elongated polyhedral particles ($C > 0.2 + R < 0.1$) from the equiaxed polyhedral ($C > 0.2 + R > 0.1$). This categorization was applied to stirred and non-stirred parts across all samples (**Table 2**). **Figure 38** shows how the percentage of elongated and equiaxed shapes in dendritic primary Si changes with s/l front velocity in both stirred and non-stirred sections. Similarly, **Figure 39** displays these variations for polyhedral primary Si.

An increase in s/l front velocity leads to a reduction in elongated dendritic primary Si and a rise in equiaxed dendritic primary Si. Similarly, higher s/l front velocity decreases the percentage of elongated polyhedral primary Si and increases the percentage of equiaxed polyhedral primary Si in stirred and non-stirred parts. This can be attributed to the fact that increasing s/l front velocity leads to an increase in the cooling rate, leading to an increase in the percentage of equiaxed particles and decreasing the percentage of elongated particles.

This agrees with the results of the researcher Korojy and his colleague, who mentioned that increasing the cooling rate altered the primary Si morphology from large, plate-like structures to smaller, equiaxed plate-like particles [69]. The front velocity influenced the morphology of primary silicon. It has been suggested that the precipitation of primary silicon could be affected by changes in the melt structure due to the increasing front velocity.

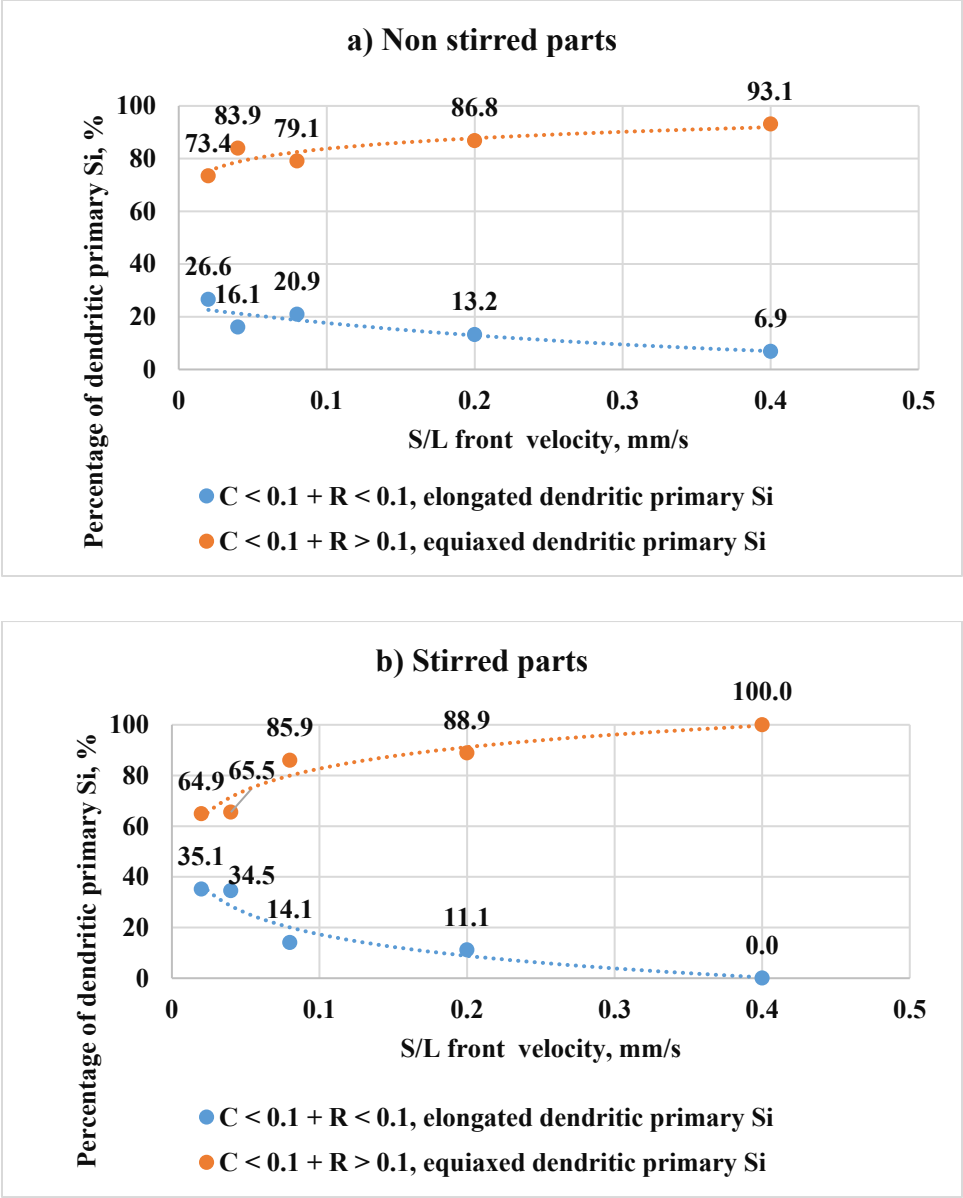

Figure 38. The percentages of the elongated and equiaxed dendritic primary Si as a function of s/l front velocity in a) non-stirred and b) stirred parts of the five samples.

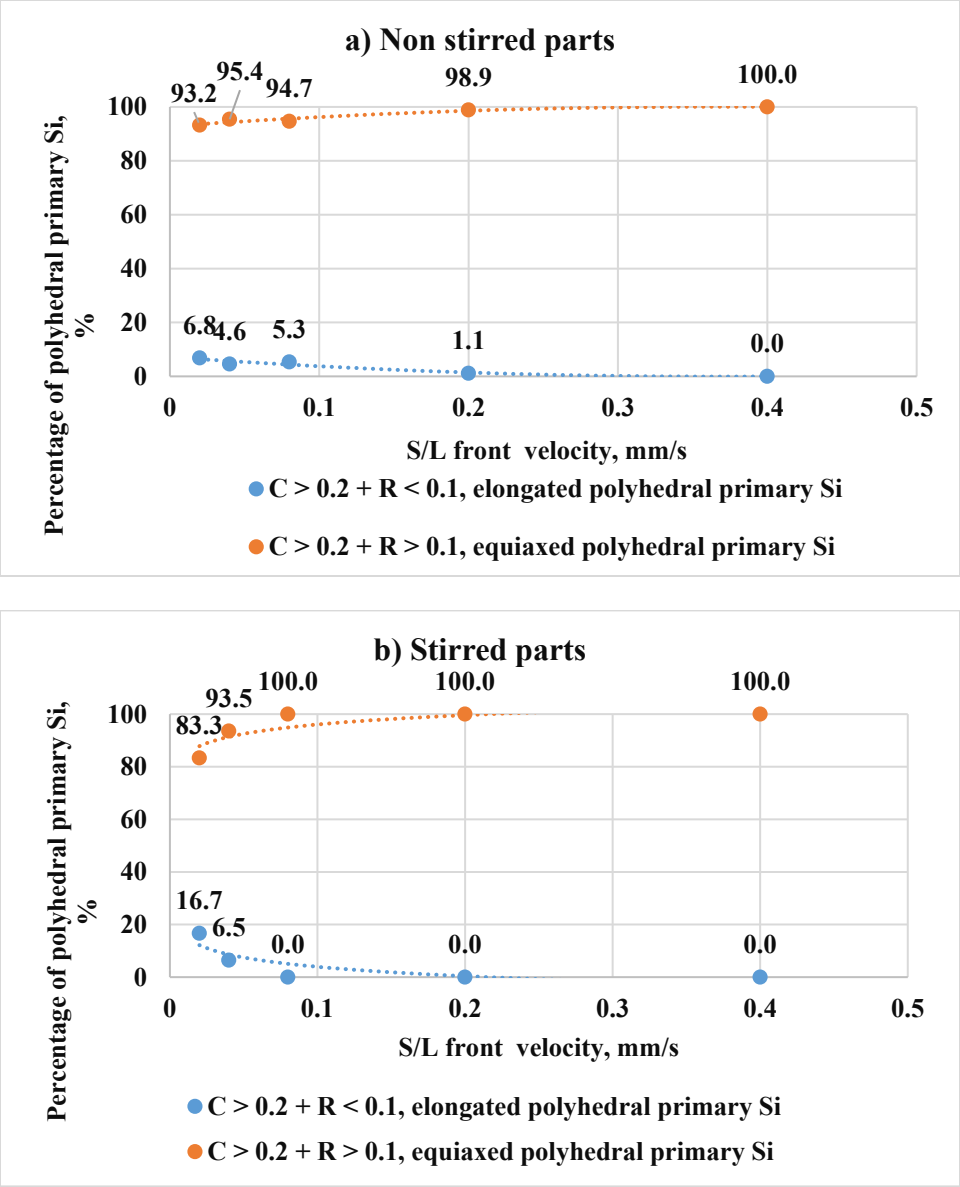

Figure 39. The percentages of the elongated and equiaxed polyhedral primary Si as a function of s/l front velocity in a) non-stirred and b) stirred parts of the five samples.

5.2.6. Area Fractions of the Eutectic Structure and the Primary Si Phase

The area fractions of the eutectic structure and the primary phase were measured using ImageJ software as mentioned in the measurement method chapter. **Figure 40, a.** displays the area fraction of the eutectic structure and the primary Si phase as a function of s/l front velocity in the non-stirred parts of the samples. The results indicate that the area fraction of the primary phase decreased with increasing s/l front velocity. Consequently, the amount of eutectic structure increases. As the solidification rate increases, the system has less time for primary phases to

nucleate and grow, which reduces the volume fraction of primary phases and favors eutectic solidification. Also, It has been demonstrated that silicon atoms form tetrahedral clusters within the melt [70]. Tetrahedral Si clusters in the melt can make nucleation of primary Si more difficult, especially under rapid solidification conditions.

Korojy and his colleague. [69] mentioned in their results that in the Al15Si and Al18Si alloys, the area fraction of primary Si decreased as the cooling rate increased. Wang et al. [71] investigated how cooling rate impacts the atomic structure of liquid in Al16Si alloy, using X-ray intensity to identify a pre-peak associated with cluster formation above 850°C. They found that clusters can rearrange during slow cooling; however, at high cooling rates, the clusters are preserved until solidification begins. Consequently, the process of solidification may be influenced by the formation of clusters due to the cooling rate. This is evidenced by the current microstructure evaluation, where an increase in the s/l front velocity enhances the cooling rate, reducing the area fraction of primary Si.

Figure 40,b presents the area fraction data for the stirred parts of the samples. In the stirred parts, the trend is opposite to that of the non-stirred parts: the area fraction of the primary phase increased with increasing s/l front velocity, and the amount of eutectic structure decreased. However, the primary Si area fraction in the stirred parts is generally lower, and the eutectic structure amount is higher, compared to the non-stirred parts for corresponding s/l front velocities. Because of the macro segregation, the concentration of Si is different.

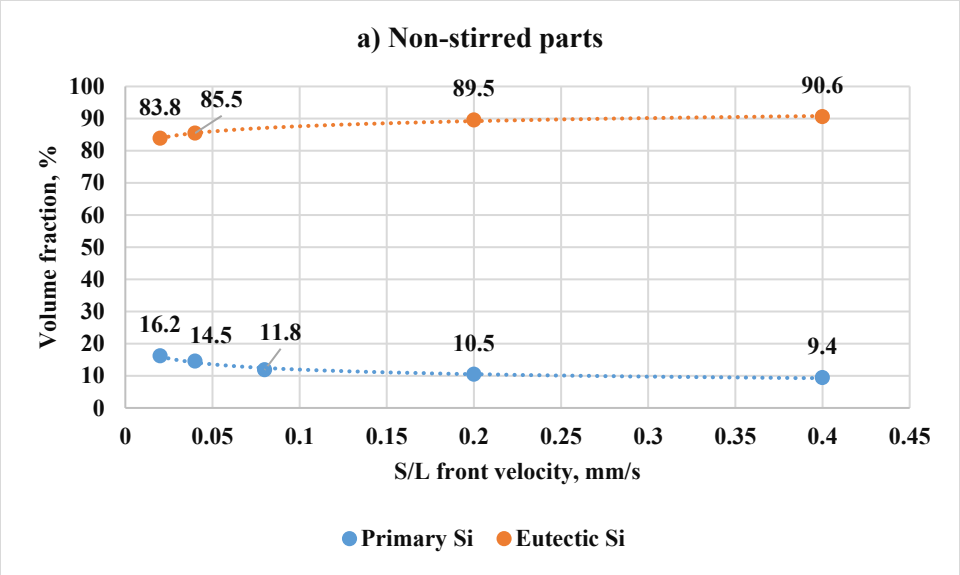

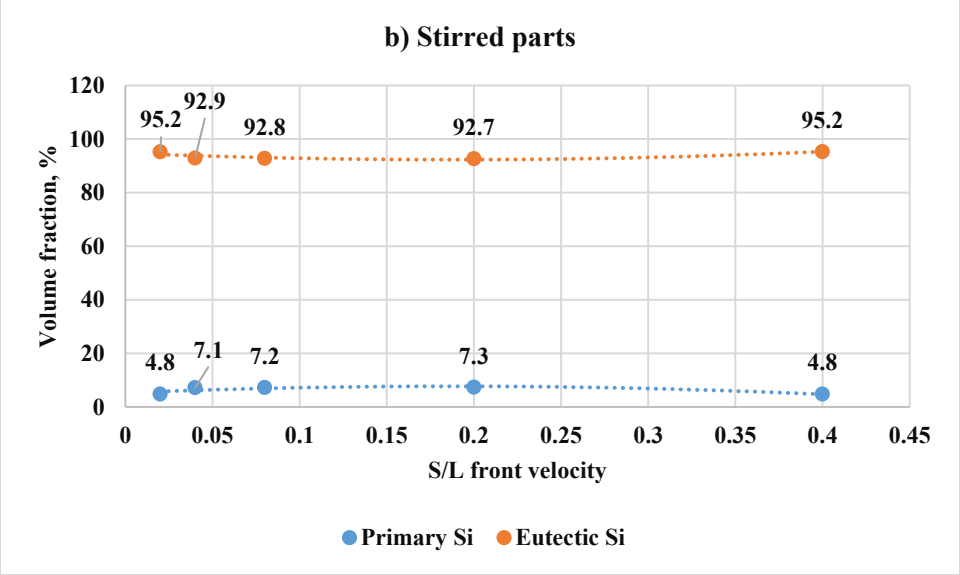

Figure 40. The area fraction of the eutectic structure and primary Si phase as a function of s/l front velocity in the a) non-stirred and b) stirred parts of the five samples.

5.2.7. Macro-Segregation

Two methods were used to analyse the distribution of the primary Si phase and eutectic structure to evaluate macro-segregation: measuring the Si concentration distribution using EDS and measuring the area fractions of primary Si and eutectic structure along the samples using ImageJ software.

5.2.7.1. The Si concentration distribution

- **The Si concentration distribution in non-stirred parts**

As mentioned in the measurement method chapter, the Si concentration distribution was measured using SEM and EDS analysis. **Figure 41** shows the Si concentration distribution along the length of the non-stirred parts of the samples whose s/l front velocities are 0.02, 0.04, 0.20, and 0.40. The graphs show a downward trend in the average Si concentration as the velocity increases. This suggests that higher velocities may lead to a more even distribution of Si within the alloy.

At lower velocities (0.02 and 0.04 mm/s), there are higher peaks and more variability in Si concentration. This variability decreases with higher velocities (0.2 and 0.4 mm/s), indicating a more uniform distribution of Si particles as velocity increases. The peaks indicate that the concentration in certain areas of the sample exceeds 18%, signifying the presence of macro-segregation. As velocity increases, these peaks diminish, suggesting a reduction in macro-segregation. The figure also shows that the Si concentration is lower at the top of the sample than at the bottom.

In other words, as mentioned in the qualitative analysis, at the beginning of each sample, where the first part of solidification was carried out, it contained a higher amount of primary Si than the later solidified parts. It is visible that the higher the sample movement velocity, the less the volume and the smaller the size of the primary Si.

1.8 mm

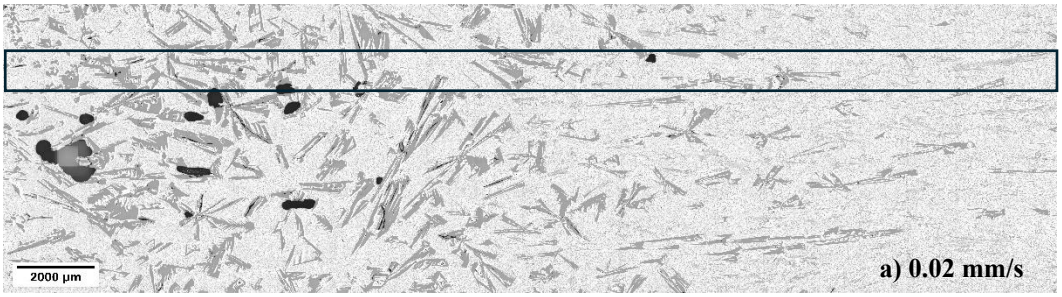
2000 µm
a) 0.02 mm/s

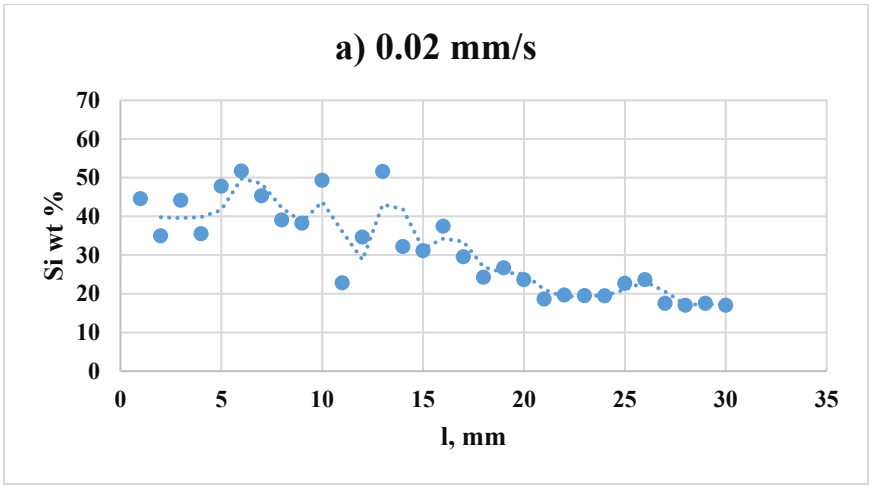
a) 0.02 mm/s
Si wt %
70
60
50
40
30
20
10
0
0
5
10
15
20
25
30
35
l, mm

3.5 mm

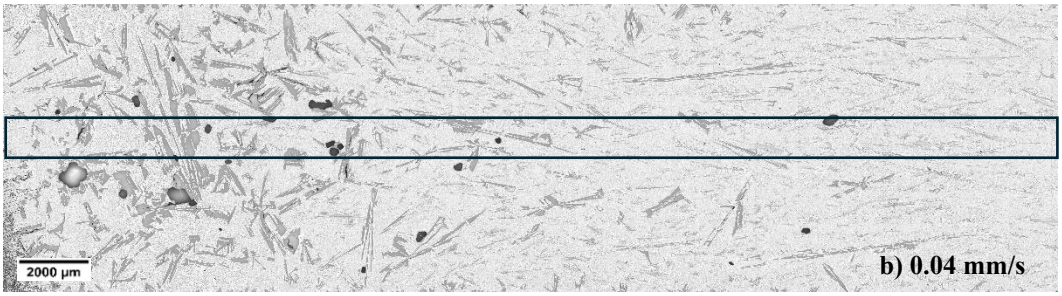
2000 µm
b) 0.04 mm/s

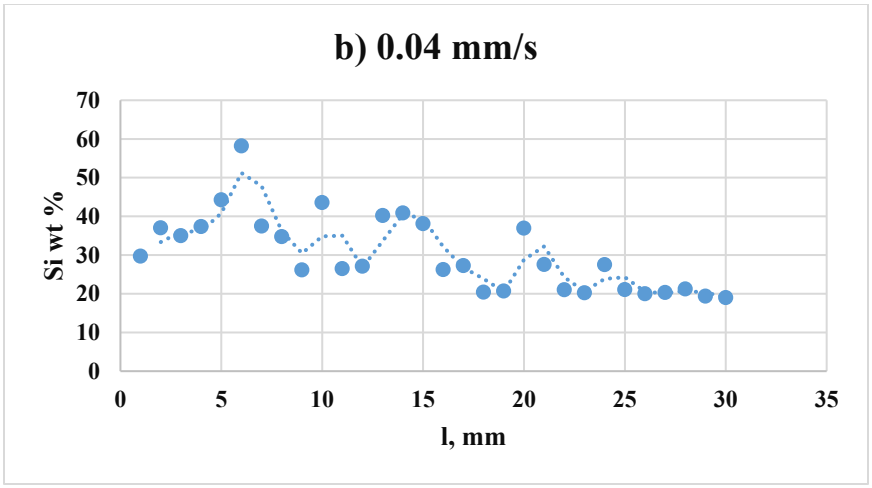
b) 0.04 mm/s
Si wt %
70
60
50
40
30
20
10
0
0
5
10
15
20
25
30
35
l, mm

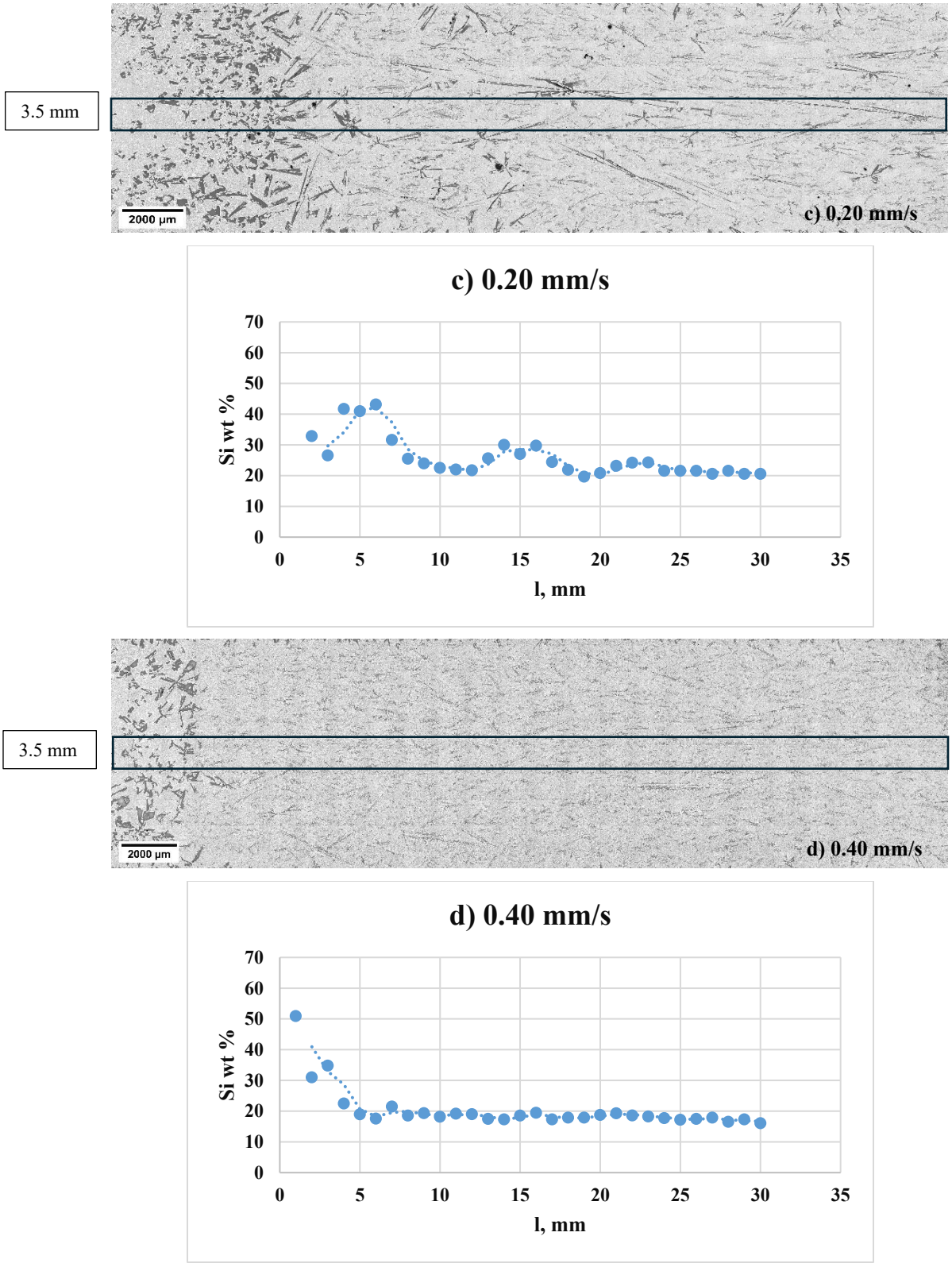

Figure 41. The Si concentration along the length of the non-stirred parts of the Al-18 wt.% Si hypereutectic samples at different s/l front velocities: a) 0.02, b) 0.04, c) 0.2, and d) 0.4 mm/s. The rectangles are the places of the EDX measurements.

The samples used are hypereutectic Al-18wt.% Si exhibits a temperature distribution characterized by eutectic and liquidus temperatures (**Figure 42, b**). Within these samples, the concentration distribution varies as follows: at the eutectic temperature, the concentration is eutectic, whereas at the liquidus temperature, the concentration is higher, approximately 18 (**Figure 42, c**). At the s/l interface, the solidification of primary Si begins, and the silicon particles progressively increase in size through the mushy zone, and the eutectic solidification starts at the eutectic front.

At the beginning of the solidification, the v_{SL} was very low due to the nature of the experiment (**Figure 18**). During the solidification, a mushy zone was built up in which the concentration of Si at the s/l front was almost 18%, and it decreased toward the bottom of the mushy zone, where the eutectic was solidifying. Because of this concentration gradient, a Si diffusion occurred from the upper part of the sample to the bottom of it. The transported Si atoms at the lower and colder part of the mushy zone were solidified on the existing solid Si phases. Because of this phenomenon, the concentration gradient in the mushy zone was almost constant in time, and the Si particles were growing until they were enriched by the eutectic front. Consequently, the silicon particles grow larger, and the concentration can exceed 18.

By the lower sample movement velocities and so by the lower v_{SL}, the diffusion had more time to perform the above-described macro-segregation, so we can see more and bigger Si particles at the bottom of the samples solidified with lower v_{SL}.

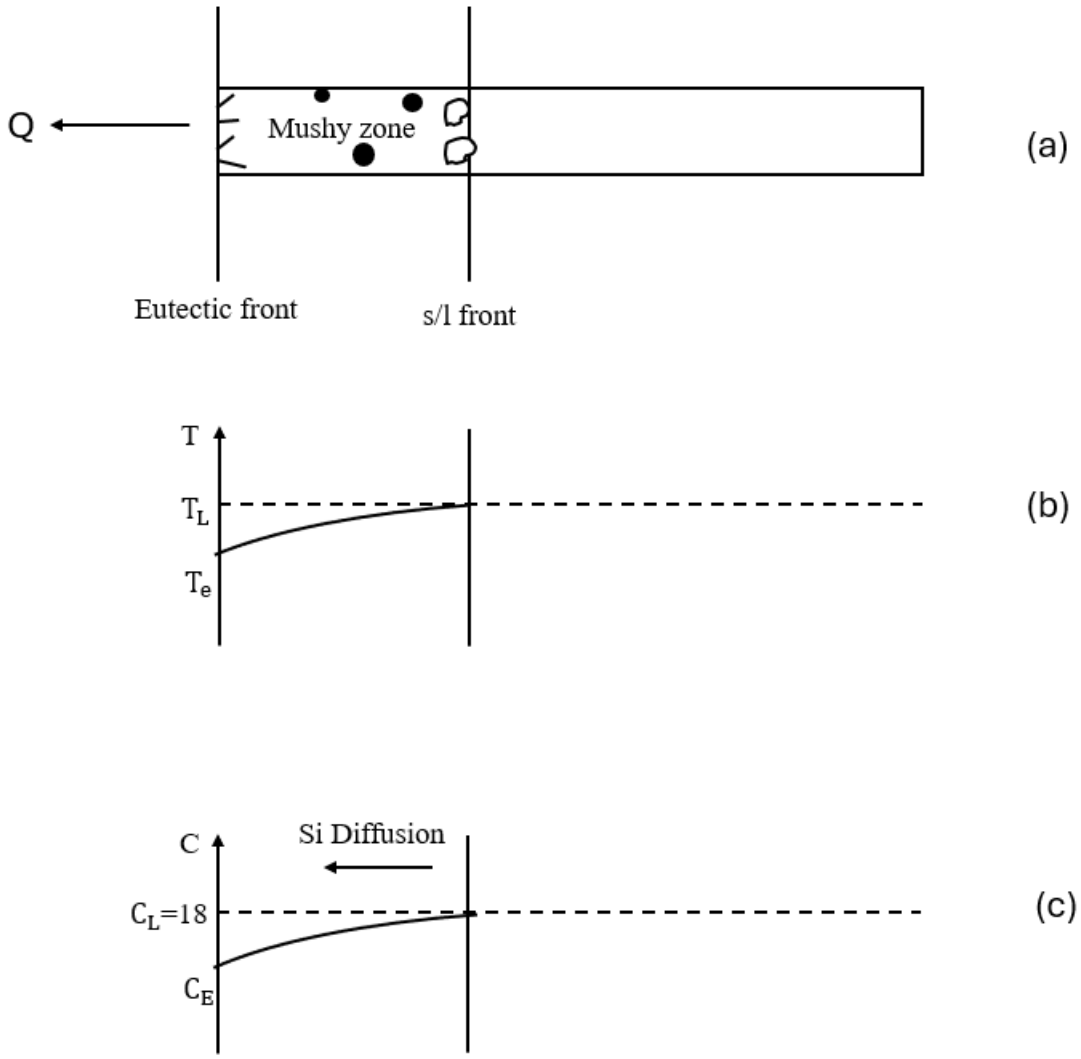

Figure 42. A schematic diagram illustrating a) the sample, b) the temperature distribution, c) the concentration distribution within the Al-18wt.% Si sample.

The summary statistics for Si concentration at different s/l front velocities provide insights into how the distribution of Si varies with changes in velocity (**Table 3**). These statistics illustrate a decrease in mean and median Si concentrations with increasing velocity. The standard deviation decreases as the velocity increases, indicating less variability in Si concentrations at higher velocities. This trend suggests that higher velocities may lead to more homogeneous distributions of Si within the samples.

Table 3. Summary Statistics for Si concentrations in the non-stirred parts across different s/l front velocities.

v_{SL} (mm/s)	Mean Concentration (%)	Median Concentration (%)	Standard Deviation (%)
0.02	31.2	30.3	11.3
0.04	30.2	27.4	9.5
0.20	25.7	24.1	6.2
0.40	20.4	18.4	6.9

- **The Si Concentration distribution in the transition zone between non-stirred and stirred parts**

Figures 43, 44, 45, and 46 show the Si concentrations distribution along the radius of the transition zone between non-stirred and stirred parts of the samples with s/l front velocities of 0.02, 0.04, 0.2, and 0.4. Notably, at the end of the non-stirred part of the sample with a velocity of 0.02 mm/s (at 34.5 mm), the average Si concentration measures 14.9%. At the end of the non-stirred parts of the samples with velocities 0.2 and 0.4 mm/s (at 36.5 and 35 mm), respectively, the average Si concentrations are 18.6% and 18.1% along the radius of the samples. This means that increasing the s/l front velocity increases the concentration of this section of the sample to be almost the same as the alloy's main concentration. This could be attributed to faster solidification, which reduces the presence of primary Si in the initial part of the sample and increases the silicon content in the liquid. When the stirring starts, a solute redistribution occurs through primary and secondary flow. In the first section of the stirred part of the sample, its velocity is 0.02 mm/s (at 52 mm), and most of the primary Si solidified at the edges; because of that, the Si concentration at the edges is higher than the centre of the sample (The peak concentration occurs at r = 2 mm, then decreases towards the sample's centre). A similar pattern is observed at the 56 mm mark and is consistent across samples with higher velocities within their stirred parts. The structure of the stirred parts is likely a result of the rotating spiral flow, which moves the primary solid parts to the edges where they can swim up and melt or get stuck and grow.

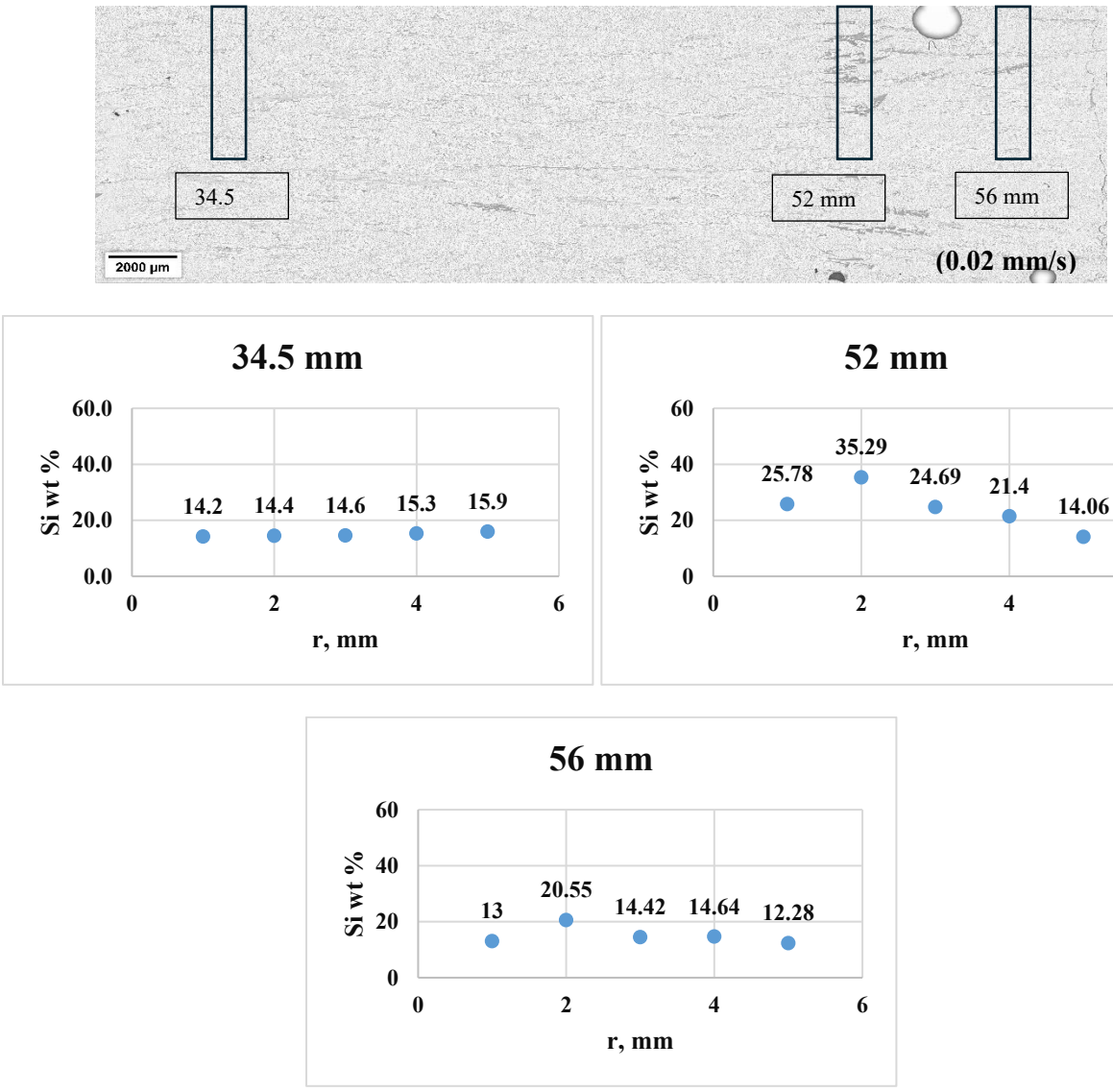

Figure 43. The Si concentration distribution along the radius of the transition zone between non-stirred and stirred parts of the Al-18 wt.% Si hypereutectic sample with the front velocity of 0.02 mm/s at different places.

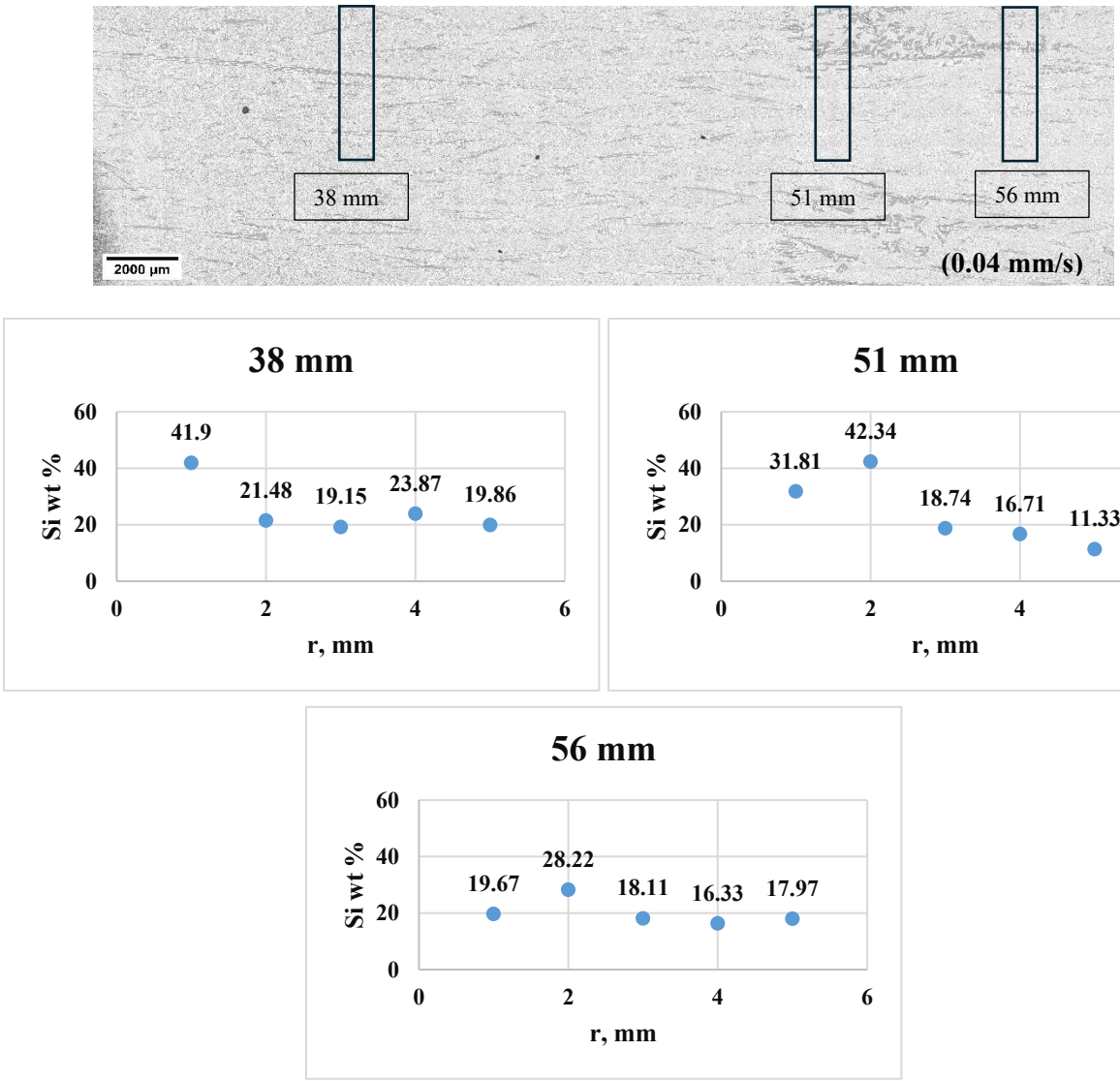

Figure 44. The Si concentration distribution along the radius of the transition zone between non-stirred and stirred parts of the Al-18 wt.% Si hypereutectic sample with the front velocity of 0.04 mm/s at different places.

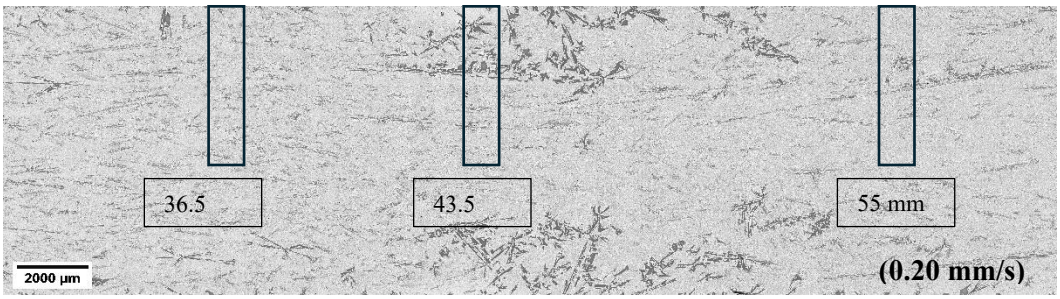

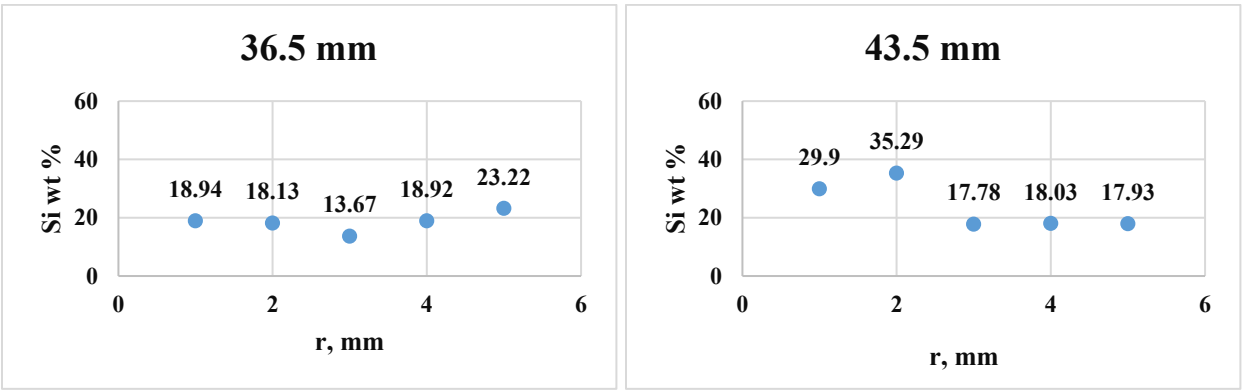

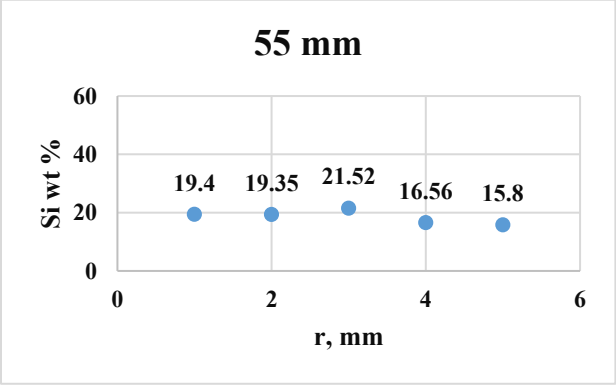

Figure 45. The Si concentration distribution along the radius of the transition zone between non-stirred and stirred parts of the Al-18 wt.% Si hypereutectic sample with the front velocity of 0.20 mm/s at different places.

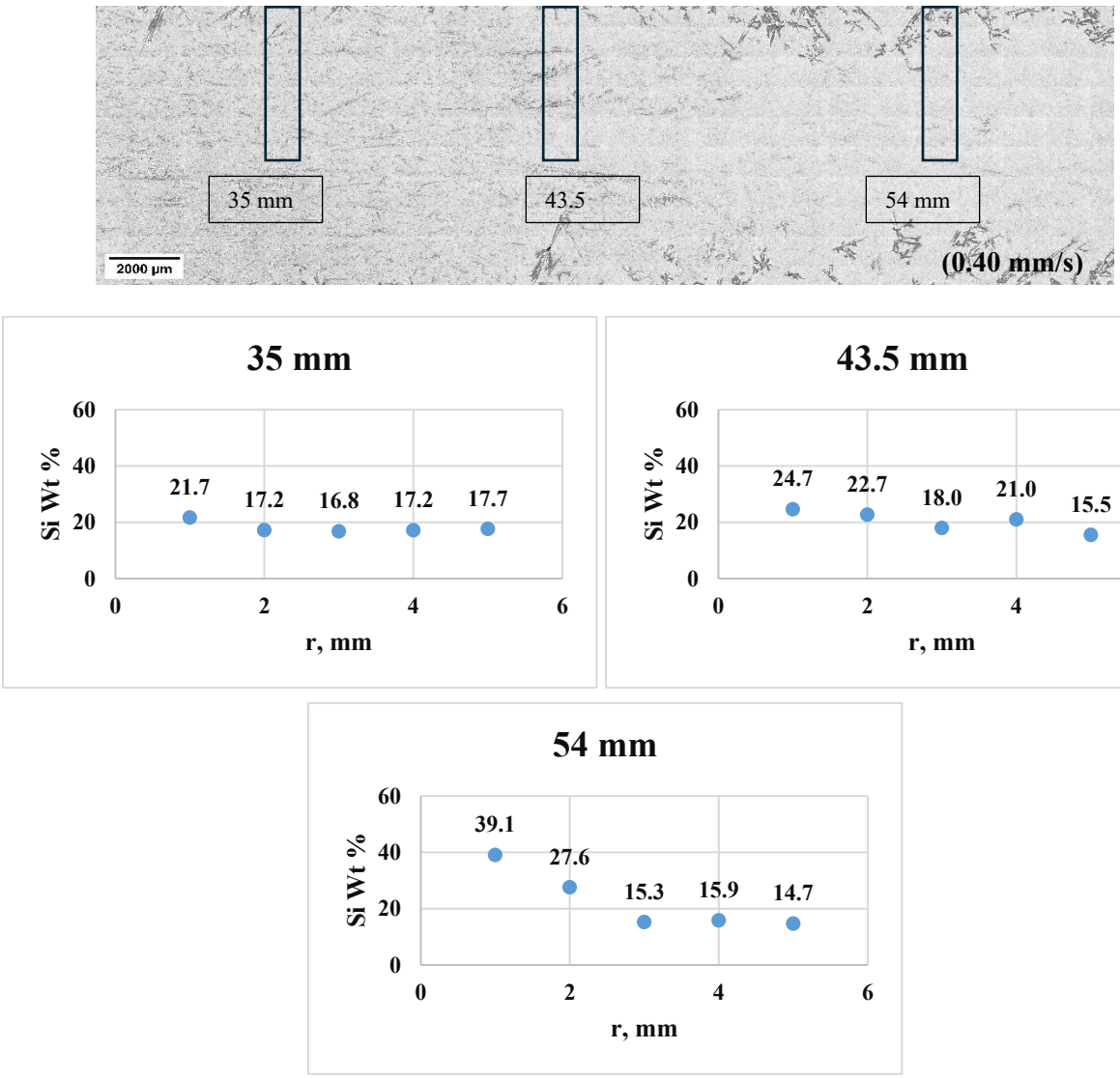

Figure 46. The Si concentration distribution along the radius of the transition zone between non-stirred and stirred parts of the Al-18 wt.% Si hypereutectic sample with the s/l front velocity of 0.40 mm/s at different places.

- **The Si concentration distribution in stirred parts**

Table 4 shows how the Si concentration varies between different parts (at 65 mm and 80 mm) of the stirred parts at each velocity and the corresponding statistical analysis. The places of the EDX measurements in stirred parts are shown in **Figure 21**. Each velocity shows a relatively small standard deviation and a narrow range, indicating moderate variation within the sample parts at each velocity. The concentration is slightly higher in the first part of the samples (at 65 mm) at all velocities. At higher velocities (0.2 and 0.4 mm/s), the variations between the first and last parts

(at 65 mm and 80 mm) tend to be smaller compared to lower velocities, suggesting a trend towards greater uniformity at these higher velocities.

Table 4. displays the concentration values for different places of the stirred parts at each velocity and the corresponding statistical analysis:

v_{SL}(mm/s)	Si Concentration at 65 mm (%)	Si Concentration at 80 mm (%)	Mean Concentration (%)	Standard Deviation (%)	Range (%)
0.02	12.3	11.8	12.1	0.3	0.5
0.04	15.2	14.7	15.0	0.3	0.5
0.20	15.1	14.7	14.9	0.2	0.4
0.40	13.8	13.4	13.6	0.2	0.4

- **The Si concentration distribution along the samples**

The average of Si concentration distribution along the radius of the transition zone between non-stirred and stirred parts of the Al-18 wt.% Si hypereutectic samples with s/l front velocities of 0.02, 0.04, 0.2 and 0.4 mm/s at three different places and the Si concentration distribution in stirred parts at different two places was added to the **Figure 41** to show the Si concentration distribution along all the sample (**Figure 47**). The figure shows that Si concentration in non-stirred parts differs from stirred parts for all velocities. At all velocities, there is a significant decrease in primary Si content from the start to the end of the samples in stirred and non-stirred parts, indicating greater segregation. The overall trend suggests that higher s/l front velocities lead to a decrease in both the average and maximum Si concentration alongside reduced variability in non-stirred parts. This is indicative of a shift towards a more uniform microstructure. This can be attributed to less time available for Si to segregate during the solidification process at higher velocities, leading to a more homogeneous material.

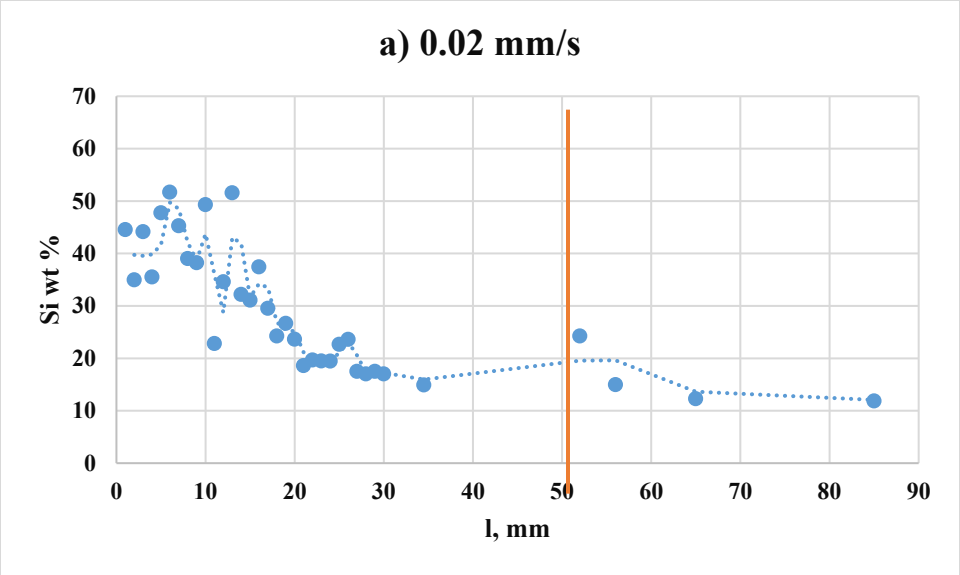
a) 0.02 mm/s
Si wt %
l, mm
0
10
20
30
40
50
60
70
80
90

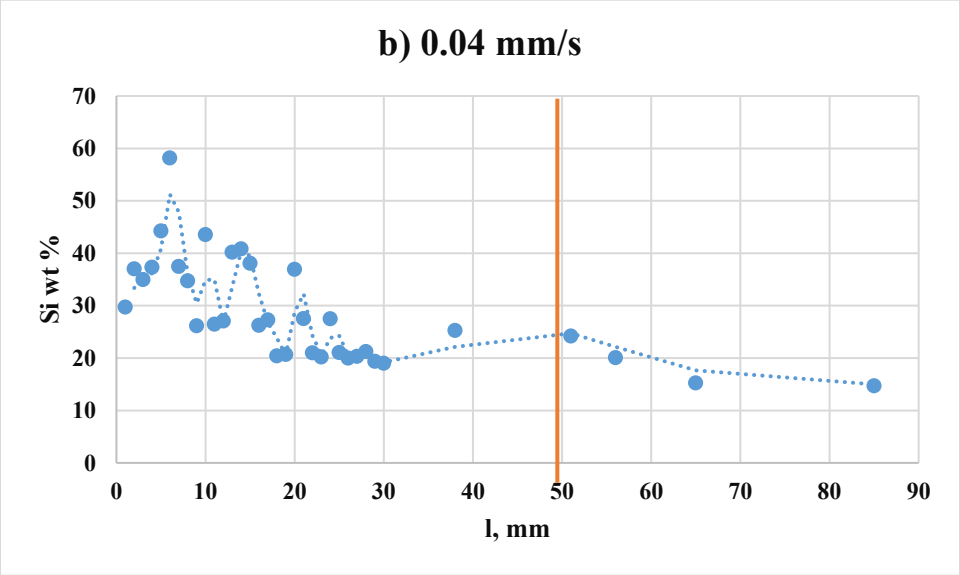
b) 0.04 mm/s
Si wt %
l, mm
0
10
20
30
40
50
60
70
80
90

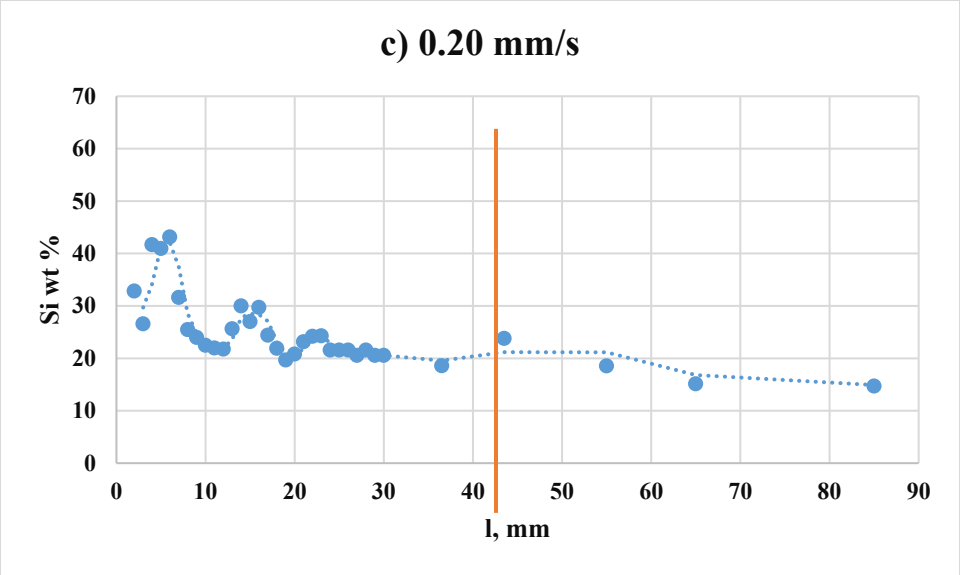

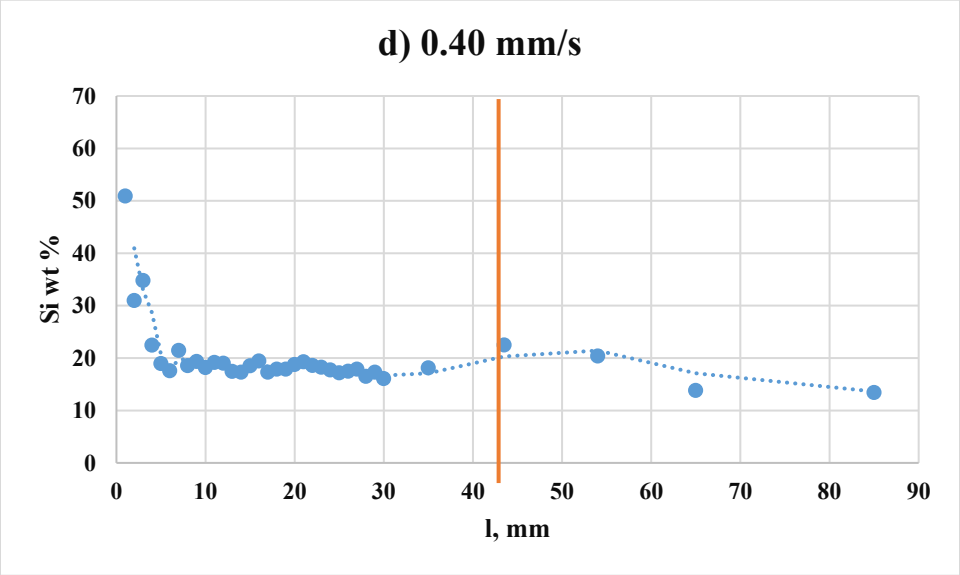

Figure 47. The Si concentration along the Al-18 wt.% Si hypereutectic samples at different s/l front velocities: a) 0.02, b) 0.04, c) 0.2, and d) 0.4 mm/s. The orange line is the dividing line between non-stirred and stirred parts.

5.2.7.2. The area fraction measurement along the samples

- **The area fraction measurement along the non-stirred parts**

The macro segregation was assessed by measuring the area fractions of primary Si and the eutectic structure along the samples as mentioned in the measurement method chapter, heading (4.4.2. Area fraction measurements of the primary Si and eutectic structure along the samples). The area

fraction of the primary Si along the non-stirred parts for each s/l front velocity is shown in **Figure 48**. Here are some key observations:

1- **Decrease in area fraction with length:** The area fraction of primary Si decreases from the 0–3.5 mm segment to the 31.5–35 mm segment across all velocities. This indicates more primary Si forms early in solidification, as confirmed by EDS measurements. The decreasing area fraction of primary Si along the sample length is due to solidification dynamics. At the start, the s/l front velocity was low (**Figure 18**), allowing more time for Si particles to grow. A concentration gradient developed in the mushy zone, driving Si diffusion from top to bottom. In the colder lower region, this Si solidified onto existing particles. As a result, more and larger primary Si formed near the bottom of the sample, while less formed toward the top, where solidification occurred faster and under reduced Si availability.

2- **Effect of s/l front velocity**:

- At lower velocities (0.02 mm/s and 0.04 mm/s), there is a significant decrease in primary Si content from the start to the end of the samples, indicating greater segregation.
- Higher velocities (0.08 mm/s, 0.2 mm/s, 0.4 mm/s) show reduced variability and narrower ranges of primary Si content, suggesting a more consistent distribution across the sample. By the lower s/l front velocities, the diffusion had more time to perform the above-described macro-segregation, so we can see more and bigger Si particles at the bottom of the samples solidified with lower v_{SL}.

The homogenization of the area fraction of primary Si in the samples began at different growth lengths, depending on the s/l front velocity. For a velocity of 0.02 mm/s, homogenization started after 24.5 mm; at 0.04 mm/s and 0.08 mm/s, it began after 10.5 mm. Samples with a front velocity of 0.2 mm/s started to homogenize after 7 mm, whereas those with 0.4 mm/s began after 3.5 mm.

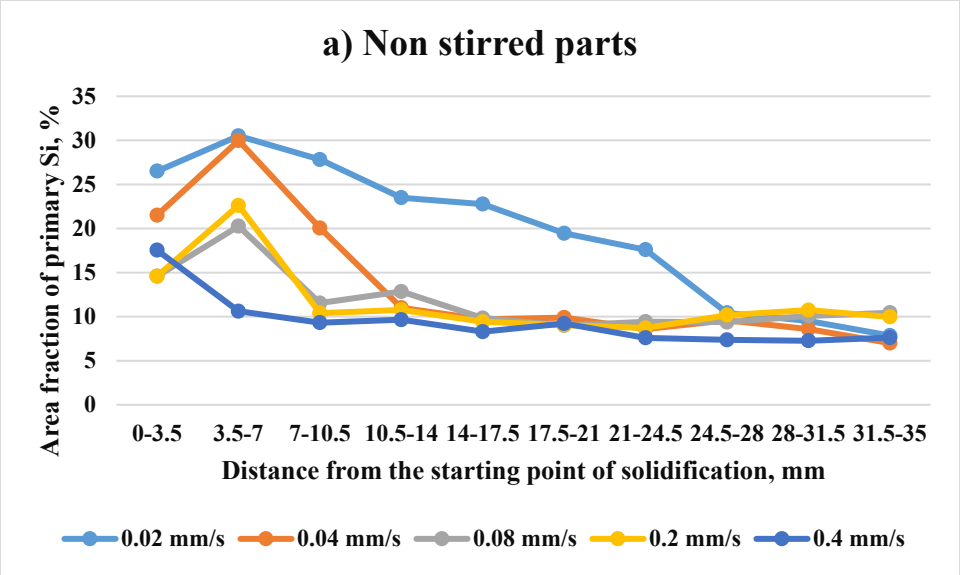

Figure 48. The area fraction of the primary Si along the growth length in the non-stirred sections of the Al-18 wt.% Si hypereutectic samples, measured at different front velocities: 0.02 mm/s, 0.04 mm/s, 0.08 mm/s, 0.20 mm/s, and 0.40 mm/s.

Table 5 shows a comparative statistical analysis summary for the primary Si content across different s/l front velocities in non-stirred parts of the samples. The observations from the analysis lead to several key conclusions about the impact of s/l front velocity on microstructure:

- **0.02 mm/s**: Shows the highest average primary Si content at 19.59% and exhibits the greatest variability (standard deviation of 8.08). This high variability and the range between minimum and maximum values indicate a significant unevenness in primary Si distribution along the sample length, with a tendency for more primary Si to segregate at the start of the solidification process.
- **0.04 mm/s**: With a slightly lower average primary Si content of 13.59% but still considerable variability (standard deviation of 7.59), this velocity suggests that some reduction in primary Si content does not substantially decrease the distribution variability, maintaining a somewhat uneven primary Si distribution similar to the lowest velocity.
- **0.08 mm/s and 0.20 mm/s**: These velocities mark a turning point where both the average and variability of primary Si content begin to decrease more noticeably (to approximately 11.74% and 11.65% with standard deviations of 3.47 and 4.18, respectively). The reduced variability at these velocities indicates a more uniform distribution of primary Si, suggesting improved homogeneity in the microstructure as the s/l front velocity increases.

- **0.4 mm/s**: This velocity demonstrates the lowest average primary Si content at 9.45% and the lowest variability (standard deviation of 3.06). It presents the most uniform distribution across all studied velocities, confirming a trend toward minimal segregation and maximal uniformity at the highest velocity.

The overall trend suggests that higher s/l front velocities lead to a decrease in both the average and maximum primary Si content alongside reduced variability. This indicates a shift towards a more uniform and consistent microstructure with fewer extremes of Si concentration throughout the sample. This can be attributed to less time available for Si to segregate during the solidification process at higher velocities, leading to a more homogeneous material.

In summary, managing s/l front velocity is crucial for controlling the distribution and segregation of primary Si in Al-18 Si alloys. Higher velocities tend to produce a more uniform microstructure with lower and more consistent Si content, which could be beneficial for applications requiring more predictable and uniform material properties.

Table 5. Statistical analysis for the primary Si content across different s/l front velocities in non-stirred parts of the samples.

v_{SL} (mm/s)	Mean %	Standard Deviation %	Minimum %	Maximum %	Range %
0.02	19.59	8.08	7.86	30.50	22.64
0.04	13.59	7.59	7.01	29.98	22.97
0.08	11.74	3.47	8.99	20.26	11.27
0.20	11.65	4.18	8.72	22.62	13.90
0.40	9.45	3.06	7.27	17.54	10.27

The corresponding distribution of the eutectic structure can be observed in **Figure 49**. The plot illustrates how the eutectic structure distribution varies across different sections at different s/l front velocities in Al-18 wt.% Si samples. Here are some key observations, it is opposite of primary Si observations:

- **Trend Consistency**: Across most velocities, the area fraction of the eutectic structure increases as the section progresses toward the end of the sample.
- **Velocity Influence**: Higher s/l front velocities generally show higher eutectic structure percentages towards the end sections.

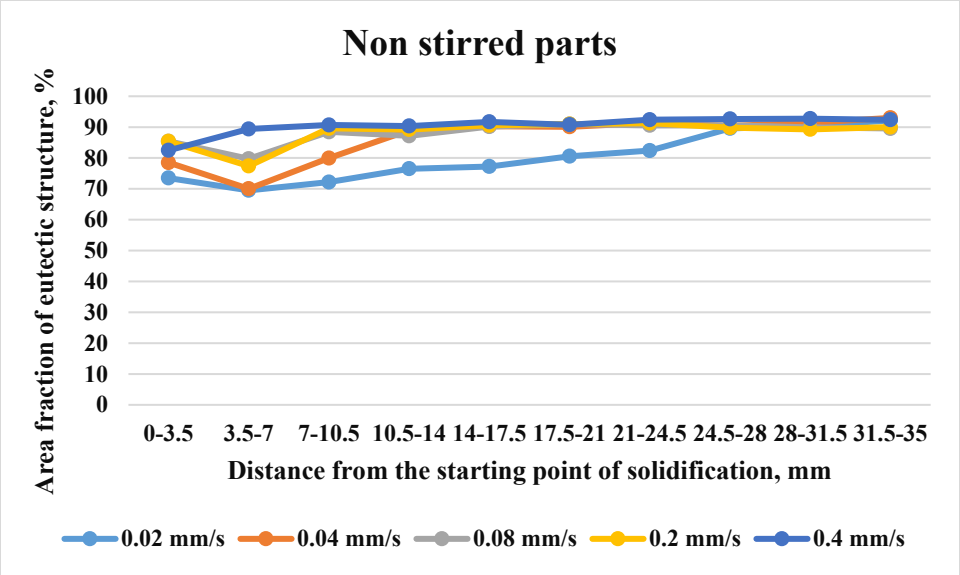

Figure 49. The area fraction of the eutectic structure along the growth length in the non-stirred sections of the Al-18 wt.% Si hypereutectic samples, measured at different front velocities: 0.02 mm/s, 0.04 mm/s, 0.08 mm/s, 0.20 mm/s, and 0.40 mm/s.

- **The area fraction measurement along the stirred parts**

The area fraction of primary Si within stirred parts of each experimental sample is depicted in **Figure 50**. Notably, when subjected to magnetic stirring, there was a significant redistribution of primary Si along the length of the samples. Here are some key observations:

1. **Decrease in area fraction with length**: For all velocities, there's a general trend of decreasing area fraction moving from the 0-3.5 mm segment towards the 31.5-35 mm segment. This suggests that primary Si tends to form more abundantly at the beginning of the solidification process. This agrees with the results of the measurements of Si concentration distribution using EDS in the stirred parts.

2. **Effect of s/l front velocity**:

- At lower velocities (0.02 and 0.04 mm/s), the area fraction decreases more sharply towards zero after the initial segments. This indicates significant macro-segregation at slower solidification rates.

- At higher velocities (0.08, 0.2, and 0.4 mm/s), the decrease in area fraction is more gradual, with primary Si still present even in the final segments. This could suggest a more uniform distribution of Si at faster solidification rates. This could be attributed to faster solidification,

which reduces the presence of primary Si in the initial part of the sample and increases the Si content in the liquid.

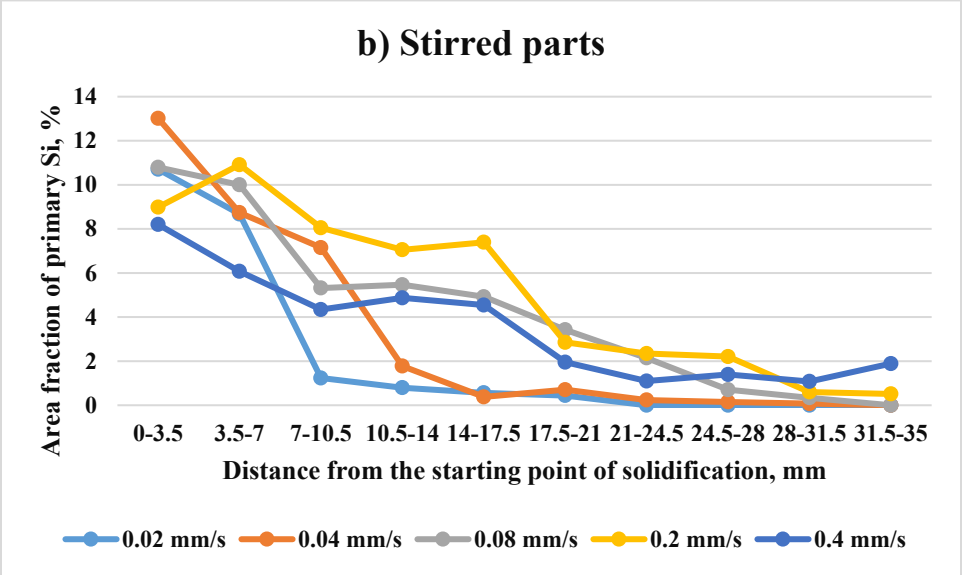

Figure 50. The area fraction of the primary Si along the growth length in the stirred sections of the Al-18 wt.% Si hypereutectic samples, measured at different front velocities: a) 0.02 mm/s, b) 0.04 mm/s, c) 0.08 mm/s, d) 0.20 mm/s, and e) 0.40 mm/s.

Table 6 shows a comparative statistical analysis summary for the primary Si content across different solidification velocities. Here are some key observations:

- **Increasing mean and median with increasing velocity**: There's a general increase in mean and median area fractions as the velocity increases up to 0.2 mm/s, suggesting that higher solidification rates might promote a more uniform and possibly higher concentration of primary Si, particularly noticeable in the median values.
- **Variability**: The standard deviation is relatively high at lower velocities (0.02 and 0.04 mm/s), indicating greater variability in Si distribution at these velocities. This variability decreases significantly at the highest velocity (0.4 mm/s).
- **Range and extremes**: The range of area fractions decreases as the velocity increases, suggesting more uniform solidification at higher velocities. The minimum values also increase with velocity, showing less drastic drops in Si content at higher solidification rates.

These observations can provide insight into the effectiveness of different s/l front velocities for achieving desired microstructural characteristics in Al-18 Si alloys. The data imply that managing s/l front velocity can be critical in controlling the distribution of primary Si in these samples.

Table 6. Statistical analysis for the primary Si content across different s/l front velocities in stirred parts of the samples.

v_{SL} (mm/s)	Mean %	Median %	Standard Deviation %	Minimum %	Maximum %	Range %
0.02	2.24	0.5	3.98	0	10.7	10.7
0.04	3.22	0.54	4.68	0	13.02	13.02
0.08	4.30	4.15	3.81	0	10.8	10.8
0.20	5.10	5.0	3.80	0.5	10.9	10.4
0.40	3.55	3.15	2.43	1.1	8.2	7.1

The corresponding distribution of the eutectic structure can be observed in **Figure 51.** The data shows a clear trend of increasing eutectic structure towards the end of the growth length in all samples. Increasing front velocity led to a decrease in the content of the eutectic structure.

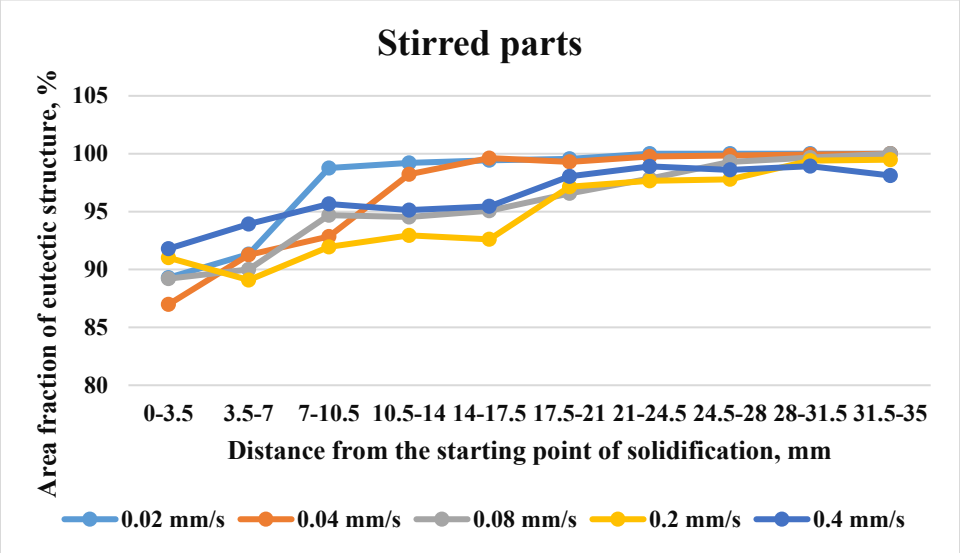

Figure 51. The area fraction of the eutectic structure along the growth length in the stirred sections of the Al-18 wt.% Si hypereutectic samples, measured at different front velocities: 0.02 mm/s, 0.04 mm/s, 0.08 mm/s, 0.20 mm/s, and 0.40 mm/s.

5.2.8. Morphology of Primary Si

Figure 52 shows the percentage of the dendritic, polyhedral, and star primary Si along the growth length of the non-stirred parts of the hypereutectic samples. The analysis shows that in the initial 0–10.5 mm segment of the non-stirred sample with a front velocity of 0.02 mm/s, dendritic primary Si is absent, appearing only as polyhedral and star-shaped forms. In samples with a 0.04 mm/s front velocity, dendritic Si is absent up to 7 mm, with only polyhedral and star-shaped forms present; beyond 7 mm, dendritic Si appears and persists to the end of the segment. Similar behaviour is observed for samples with front velocities of 0.04, 0.08, and 0.20 mm/s, where dendritic Si appears after 7 mm. For a 0.40 mm/s front velocity, dendritic Si is absent up to 3.5 mm and begins to appear afterward.

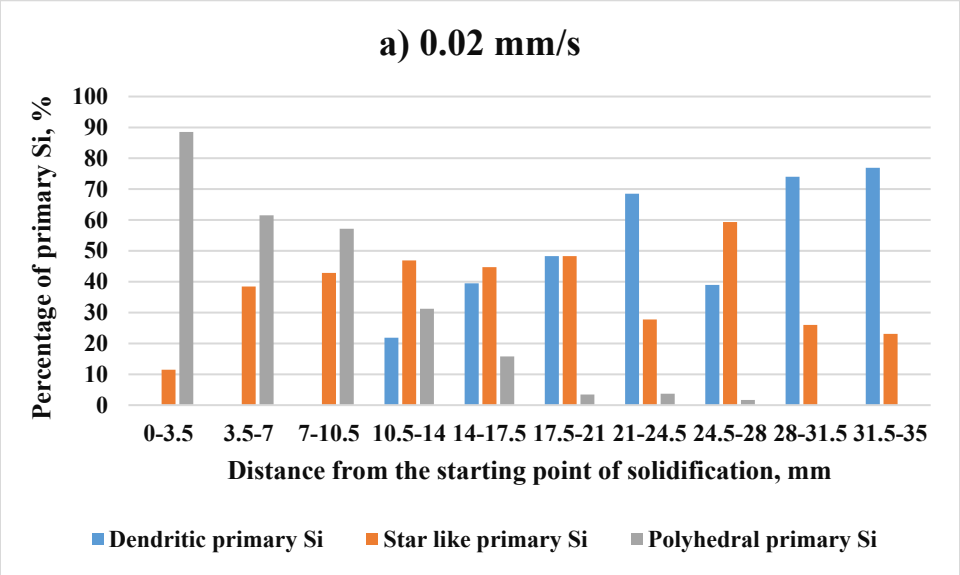

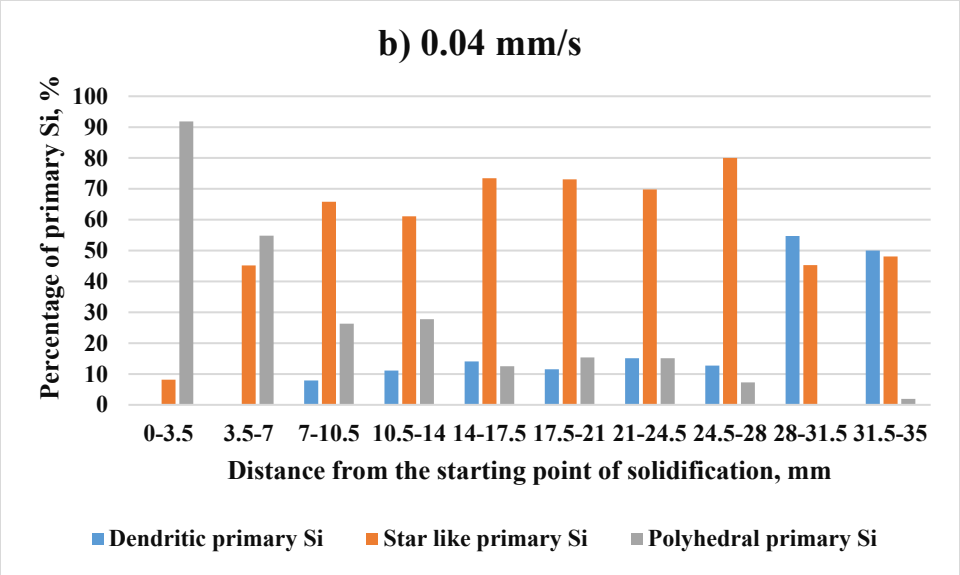
b) 0.04 mm/s
Percentage of primary Si, %
100
90
80
70
60
50
40
30
20
10
0
0-3.5
3.5-7
7-10.5
10.5-14
14-17.5
17.5-21
21-24.5
24.5-28
28-31.5
31.5-35
Distance from the starting point of solidification, mm
Dendritic primary Si
Star like primary Si
Polyhedral primary Si

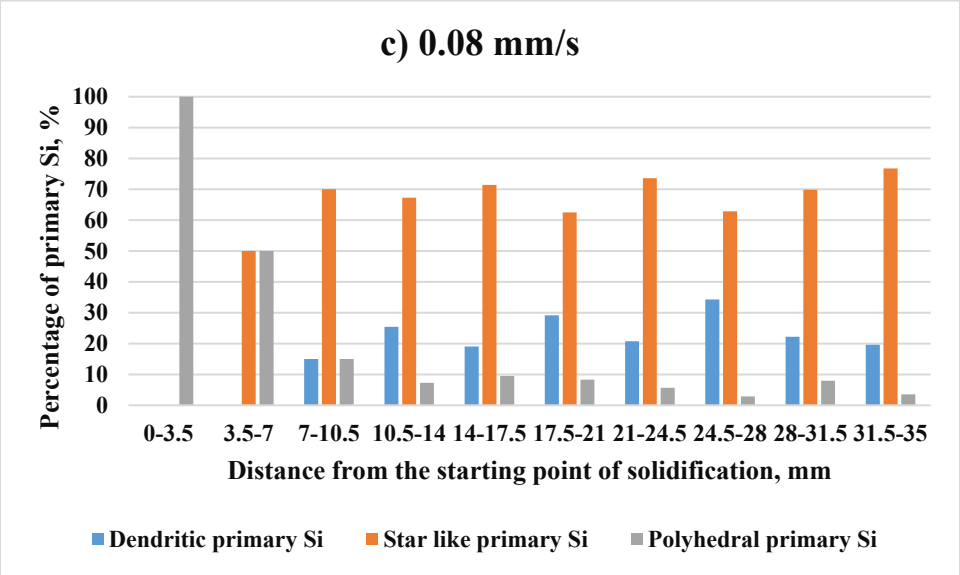
c) 0.08 mm/s
Percentage of primary Si, %
100
90
80
70
60
50
40
30
20
10
0
0-3.5
3.5-7
7-10.5
10.5-14
14-17.5
17.5-21
21-24.5
24.5-28
28-31.5
31.5-35
Distance from the starting point of solidification, mm
Dendritic primary Si
Star like primary Si
Polyhedral primary Si

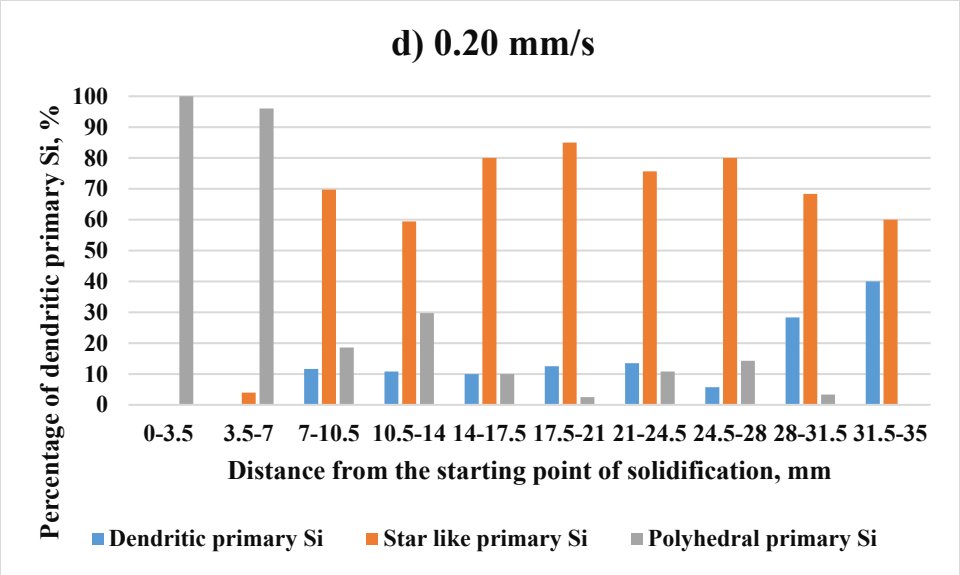

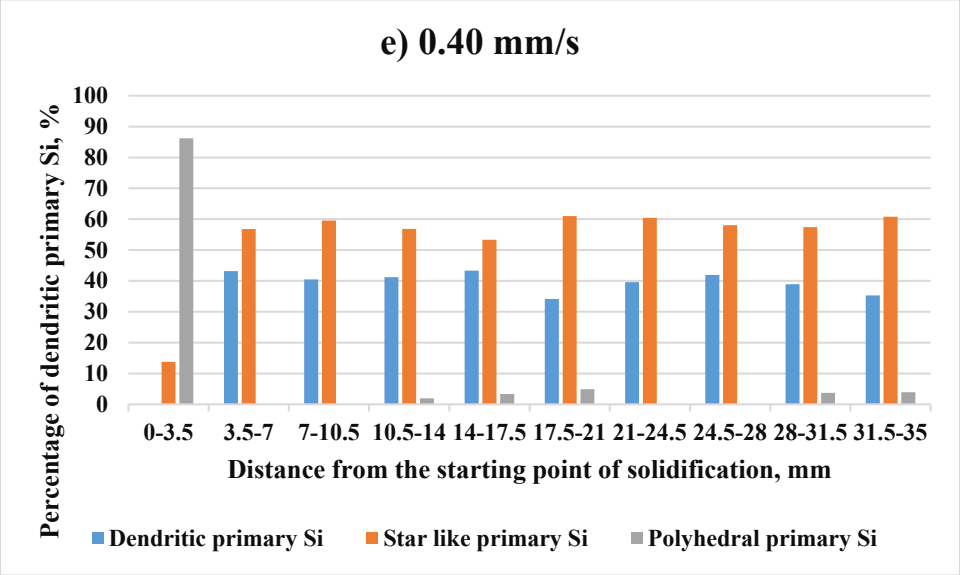

Figure 52. The percentage of the dendritic, polyhedral, and star primary Si along the growth length of the non-stirred parts of the hypereutectic samples, measured at different front velocities: a) 0.02 mm/s, b) 0.04 mm/s, c) 0.08 mm/s, d) 0.20 mm/s, and e) 0.40 mm/s.

5.3. Conclusion

The effect of forced melt flow by an RMF, s/l front velocity, and eutectic front velocity on hypereutectic Al - 18 wt.% Si alloy was studied by solidifying samples with various movement velocities at a temperature gradient of G = 8 K/mm. Each sample was solidified unidirectionally into two parts, one part without stirring and the other with stirring by RMF at a magnetic intensity of B = 7.2 mT. The study involved measuring the length, angular orientation, and distance between

the eutectic Si lamellas, the equivalent diameter and shape factors of primary Si. In addition, the macro-segregation, Si concentration distribution, and area fraction of the primary Si phase and eutectic structure were also studied. The main results can be summarised as follows:

- Increasing the eutectic front velocity during solidification refines the length of eutectic Si lamellas by raising the percentage of fine eutectic lamellas (less than 10 μm) and reducing the percentage of coarse eutectic lamellas (greater than 10 μm).
- Based on the angle measurements, the smallest eutectic Si lamellas (0–2 μm in length) are most oriented at a 45° angle. In contrast, larger eutectic lamellas tend to grow more parallel to the solidification direction. Increasing the eutectic front velocity during solidification decreases the maximum percentage of eutectic lamellas at their preferred angles and increases the percentage of lamellas at other angles, resulting in greater scattering of the eutectic Si lamellas.
- Increasing the eutectic front velocity during solidification reduces the distance between eutectic lamellas.
- The final alloy's microstructural evolution is also significantly altered due to RMF, which creates a spiral flow in the melt. The spiral flow modifies heat and mass transfer conditions within the melt and limits the solute diffusion in front of the eutectic interface. It, therefore, leads to refining the eutectic Si lamellas, increasing their diversity, and decreasing the distance between them.
- Increasing the s/l front velocity during solidification resulted in an increased percentage of fine primary Si particles (<200 μm) and a decreased percentage of coarse primary Si particles (>200 μm) in stirred and non-stirred parts, leading to the refinement of primary Si particles.
- Increasing s/l front velocity during solidification in non-stirred sections reduces dendritic percentages and increases star-like particles, while polyhedral percentages remain constant. In stirred parts, the percentages of dendritic, star-like, and polyhedral Si shapes are relatively stable across different front velocities.
- Higher s/l front velocities decrease elongated dendritic and polyhedral primary Si while increasing their equiaxed forms in both stirred and non-stirred parts.

- Increasing s/l front velocity reduces the primary phase area fraction and raises the eutectic structure amount in non-stirred parts. Conversely, higher front velocity in stirred parts boosts the primary Si area fraction while decreasing the eutectic structure amount.
- Increasing the front velocity tends to reduce macro segregation across the length of the samples.

6. Claims

The study is based on a series of unidirectional solidification experiments conducted using a hypereutectic Al-18wt.% Si alloy. These experiments were carried out in a vertical Bridgman-type tube furnace equipped with a Magnetohydrodynamic (MHD) inductor. Cylindrical samples measuring ∅ 8.1 mm × 90 mm were solidified under varying conditions.

Five hypereutectic samples were solidified at different movement velocities. The average solid/liquid (s/l) front velocities (v_{SL}) were: 0.02 mm/s, 0.04 mm/s, 0.08 mm/s, 0.20 mm/s, and 0.40 mm/s. Corresponding average eutectic front velocities (v_e): 0.02 mm/s, 0.05 mm/s, 0.09 mm/s, 0.20 mm/s, and 0.40 mm/s. The average temperature gradient (G) during the experiments was 8 K/mm (**Table 7**).

Each sample was solidified in two parts: the first half without magnetic stirring and the second half under a rotating magnetic field (RMF) with an intensity of B=7.2 mT. The samples were sectioned and prepared through a process of grinding, polishing, and etching using an aqueous solution of hydrogen fluoride (HF) acid. All claims made in relation to these solidification parameters are valid and supported by the experimental/analytical evidence provided.

Table 7. The solidification experimental parameters.

Name of sample	v_m [mm/s]	v_{SL} [mm/s]	v_e [mm/s]	B [mT]	G [K/mm]
A	0.02	0.02	0.02	0__7.2	8
B	0.05	0.04	0.05	0__7.2	8
C	0.10	0.08	0.09	0__7.2	8
D	0.20	0.20	0.20	0__7.2	8
E	0.50	0.40	0.40	0__7.2	8

6.1. Claim 1: Refinement of eutectic structure and reduction in inter-lamellar distance through increased eutectic front velocity and application of RMF during solidification

Claim 1a. Impact of the eutectic front velocity on the length of eutectic Si lamellas

Increasing the eutectic front velocity from 0.02 mm/s to 0.40 mm/s (as shown in **Table 7**) leads to a significant refinement of the eutectic lamellas. This refinement is characterised by:

- An increase in the percentage of fine lamellas (length < 10 μm) from 60.3% to 86.4% in non-stirred parts is described by the expression (Lamellas % = 1126.8v_{ens}^3 - 978.57v_{ens}^2 + 288.33v_{ens} + 55.577), where Lamellas % is the percentage of the eutectic lamellas, and v_e is the eutectic front velocity. In stirred parts, the increase from 63.2% to 87.9% is described by the expression (Lamellas % = 1108.2v_{es}^3 - 938.42v_{es}^2 + 269.53v_{es} + 59.299)
- A corresponding decrease in the percentage of coarse lamellas (length > 10 μm) from 39.7% to 13.6% in non-stirred parts, and from 36.8% to 12.1% in stirred parts (**Figure 53**).

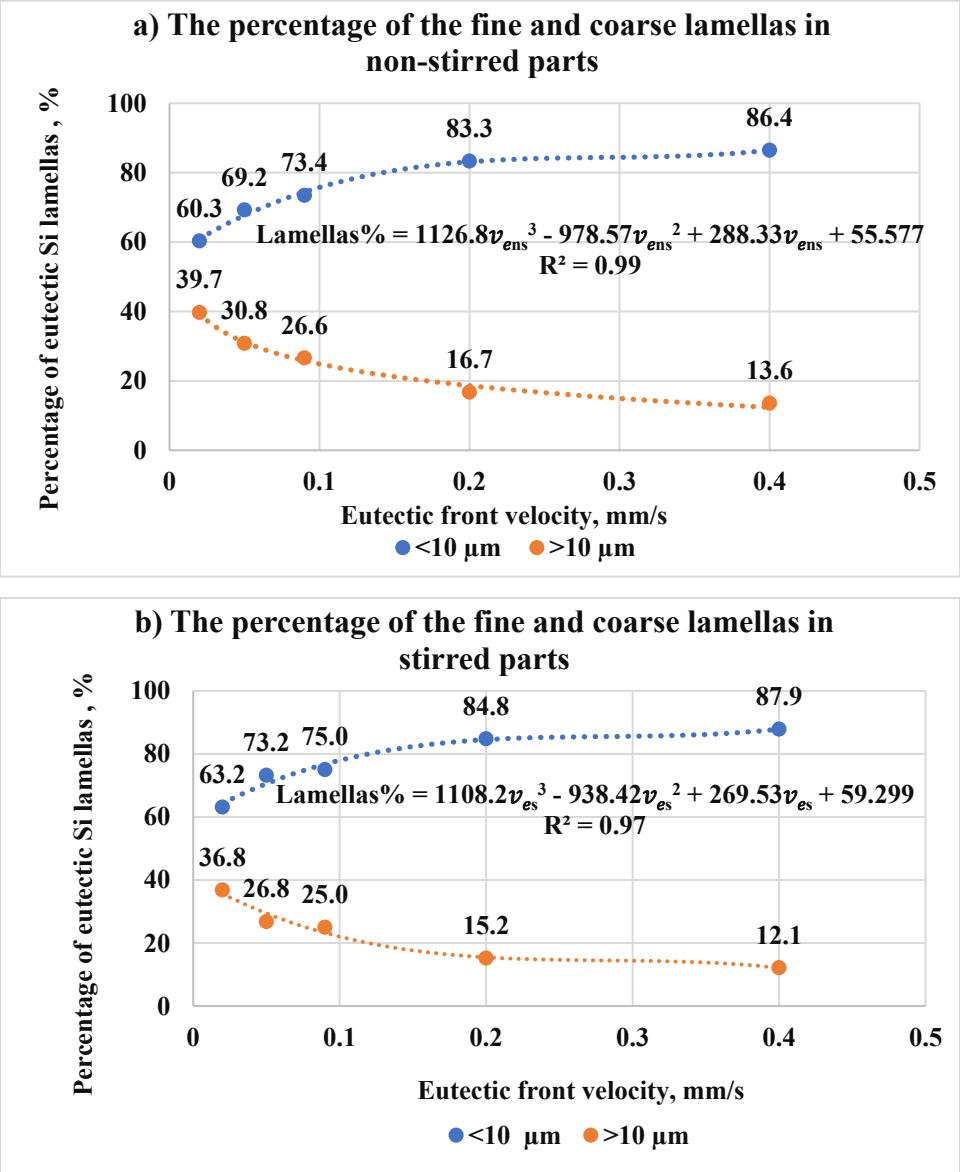

Figure 53. The percentages of the fine and coarse eutectic Si lamellas as a function of eutectic front velocity in both a) non-stirred and b) stirred sections.

Claim 1b. Impact of RMF on the length of eutectic Si lamellas

A comparative analysis between non-stirred and stirred parts reveals that the application of a RMF at B=7.2 contributes to the refinement of eutectic lamellas. At 0.02 mm/s, the percentage of fine eutectic lamellas increased by about 3%, while the percentage of coarse eutectic lamellas decreased correspondingly (**Figure 53**). The same trend was observed for other velocities.

Claim 1c. Impact of the eutectic front velocity on average inter-lamellar distance

Increasing the eutectic front velocity from 0.02 mm/s to 0.40 mm/s significantly reduces the average eutectic inter-lamellar distance from 5.7 µm to 2.1 µm in non-stirred parts, and from 5.0 µm to 1.8 µm in stirred parts (**Figure 54**). The reduction in the average inter-lamellar distance followed the formula:

- For non-stirred parts: $\lambda = 14.1 v_{ens}^{-0.31}$
- For stirred parts: $\lambda = 12 v_{es}^{-0.31}$

Where, λ is the average inter-lamellar distance, v_{ens} is the eutectic front velocity in non-stirred parts, and v_{es} is the eutectic front velocity in stirred parts.

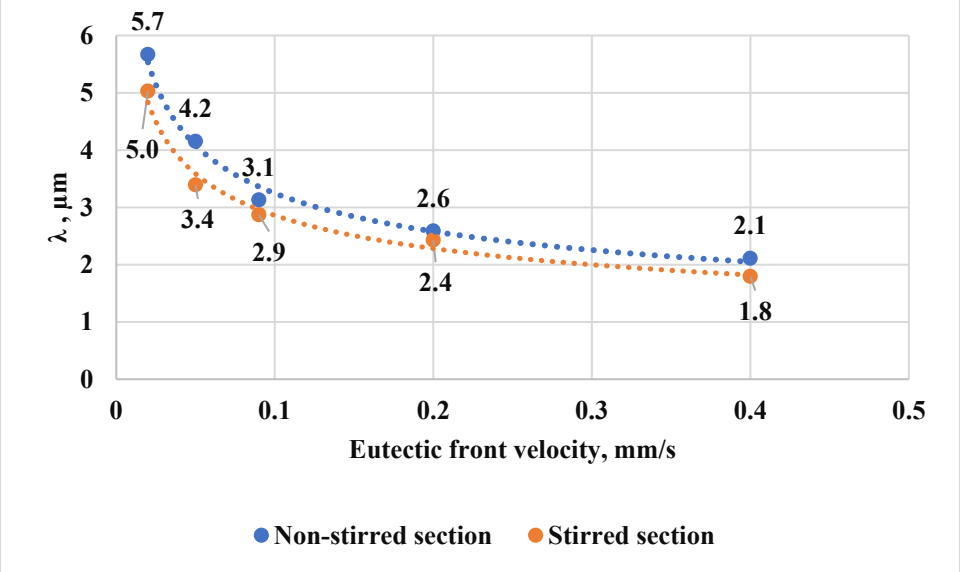

Figure 54. Distance between eutectic Si lamellas (λ) as a function of eutectic front velocity in stirred and non-stirred sections of the samples.

Claim 1d. Impact of RMF on average inter-lamellar distance

A comparative analysis of non-stirred and stirred parts demonstrates that applying an RMF at B=7.2 mT decreases the spacing between eutectic lamellas. At 0.02 mm/s, the distance decreased by about 0.7 µm (**Figure 54**). The same trend was observed for other velocities.

6.2. Claim 2. The lengths of eutectic Si lamellas vary with their growth angles. Increasing eutectic front velocities and applying an RMF enhance the diversity of these growth angles.

Claim 2a. Influence of growth angles on eutectic Si lamellas lengths

Eutectic lamellas that are more parallel to the solidification direction are more likely to achieve greater lengths (**Figure 55**). In contrast, when the eutectic lamellas grow at high angles relative to the solidification direction, their growth is limited, resulting in shorter lengths.

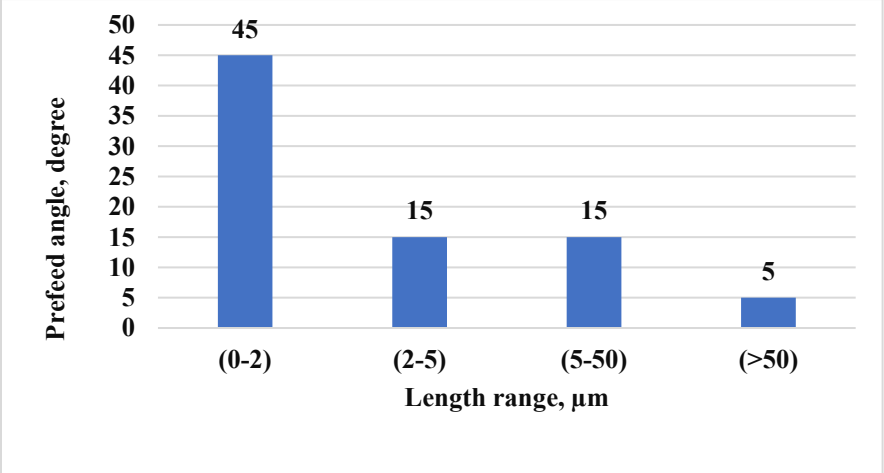

Figure 55. The preferred angle of eutectic Si lamellas in the hypereutectic alloy for different length ranges.

Claim 2b. Effect of the eutectic front velocity on the growing angles of the eutectic Si lamellas

When the eutectic front moves faster, the eutectic Si lamellas are less likely to grow at their preferred angles. For example, as the eutectic front velocity increases from 0.02 mm/s to 0.40 mm/s, the percentage of short lamellas (0–2 µm) aligned at the preferred angle decreases from 31.0% to 25.7% in non-stirred parts, and from 29.7% to 20.3% in stirred regions. This results in a wider variety of growth angles. The same trend is also observed for longer lamellas (**Figure 56**).

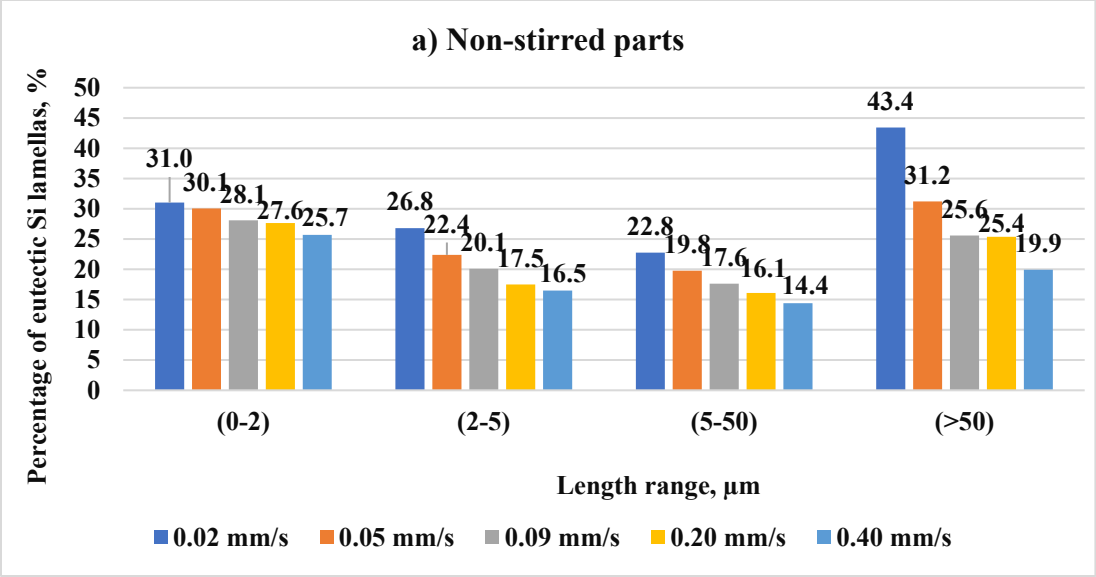

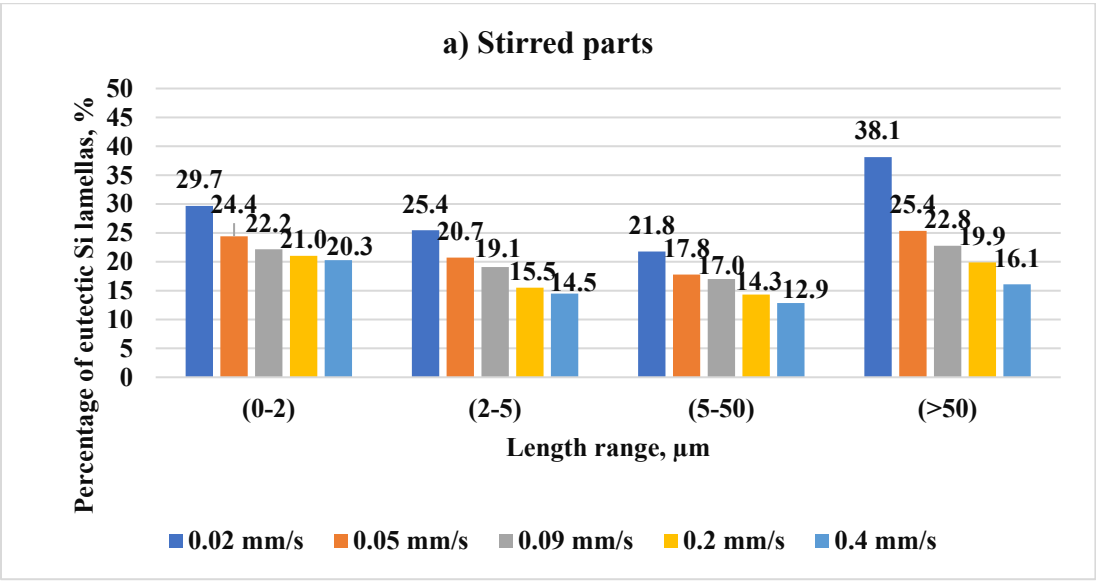

Figure 56. The highest percentages of eutectic Si lamellas oriented at the preferred angle for different length ranges at different eutectic front velocities: 0.02, 0.05, 0.09, 0.2, and 0.4 mm/s in a) non-stirred sections and b) stirred parts of the samples.

Claim 2c. Effect of RMF on the growing angles of the eutectic Si lamellas

Applying a RMF during solidification makes the eutectic Si lamellas less likely to align at their preferred angles. Instead, their growth angles become more diverse. This effect is visible when comparing the stirred (RMF applied) and non-stirred parts of the samples (**Figure 56**).

6.3. Claim 3: Characterisation of Primary Si particles

Novel characterisation methods are investigated to analyse the primary Si in the hypereutectic Al-18 wt.% Si alloy. The characterisation of the primary Si particles is based on two key factors: size and shape.

Claim 3a. Size of primary Si

The primary Si particle size in the hypereutectic Al-18 wt.% Si alloy is assumed to equal the equivalent diameter. Using this approach, a size distribution figure can be generated (**Figure 57**). Additionally, the primary Si equivalent diameter measurements can be used to describe the effect of changing the solidification parameters on the size of the primary Si.

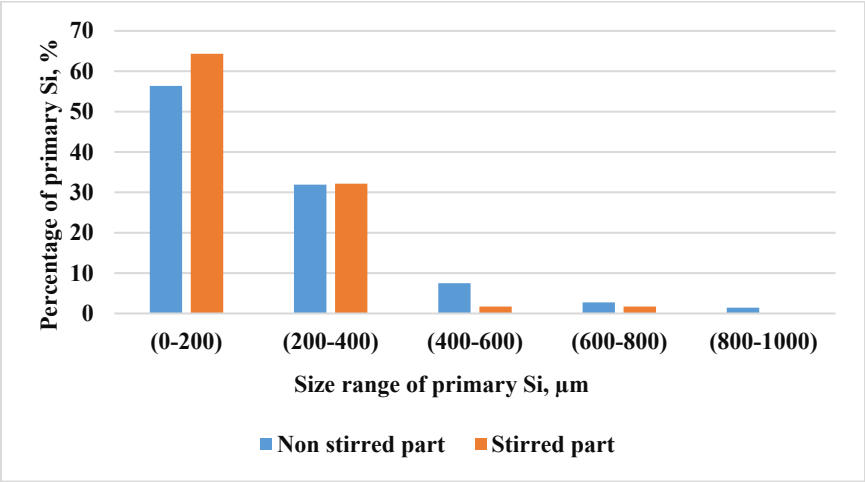

Figure 57. The percentage of primary Si particles as a function of their size range in the stirred and non-stirred parts of the sample that solidify at $v_{S/L}$ = 0.02 mm/s.

Claim 3b. Shape of primary Si

Circularity and roundness have been proposed as key parameters for characterizing the shape of primary Si particles. Based on circularity (C), the particles can be classified into three main shape categories: primary Si particles have a dendritic shape when C < 0.1, a star-like shape when 0.1 < C < 0.2, and a polyhedral shape when C > 0.2. Further classification can be made by including roundness (R). Primary Si particles have an elongated dendritic shape when C < 0.1 and R < 0.1, and an equiaxed dendritic shape when C < 0.1 and R > 0.1. They have an elongated polyhedral shape when C > 0.2 and R < 0.1, and an equiaxed polyhedral shape when C > 0.2 and R > 0.1 (**Table 8**).

Table 8. Dimensionless shape factors of various shapes of primary Si.

Shape Description	Shape Description	Average of circularity	Standard deviation	Average of roundness	Standard deviation
Polyhedral	Equiaxed polyhedral	0.59	0.1	0.58	0.2
	Elongated polyhedral (Plate like)	0.22	0.1	0.07	0.0
Dendritic	Equiaxed dendritic	0.08	0.0	0.33	0.1
	Elongated dendritic (Feathery)	0.05	0.0	0.07	0.0
Star like	Star like	0.12	0.0	0.43	0.2

6.4. Claim 4: Refinement of primary Si through increased s/l front velocity during solidification

Increasing the s/l front velocity from 0.02 mm/s to 0.40 mm/s effectively refines primary Si particles. This refinement is characterized by:

- An increase in the percentage of fine particles (less than 200 μm) from 56.4% to 82.2% in non-stirred parts is described by the expression (Primary Si % = 7.5578ln(v_{SLns}) + 84.552), where primary Si % is the percentage of primary Si, and v_{SL} is the s/l front velocity. In stirred parts, the increase from 64.3% to 69.4% is described by the expression (Primary Si % = 1.8517ln(v_{SLs}) + 71.791).
- A corresponding decrease in the percentage of coarse particles from 43.6 to 17.7% in non-stirred parts, and from 35.7% to 30.6% in stirred parts (**Figure 58**).

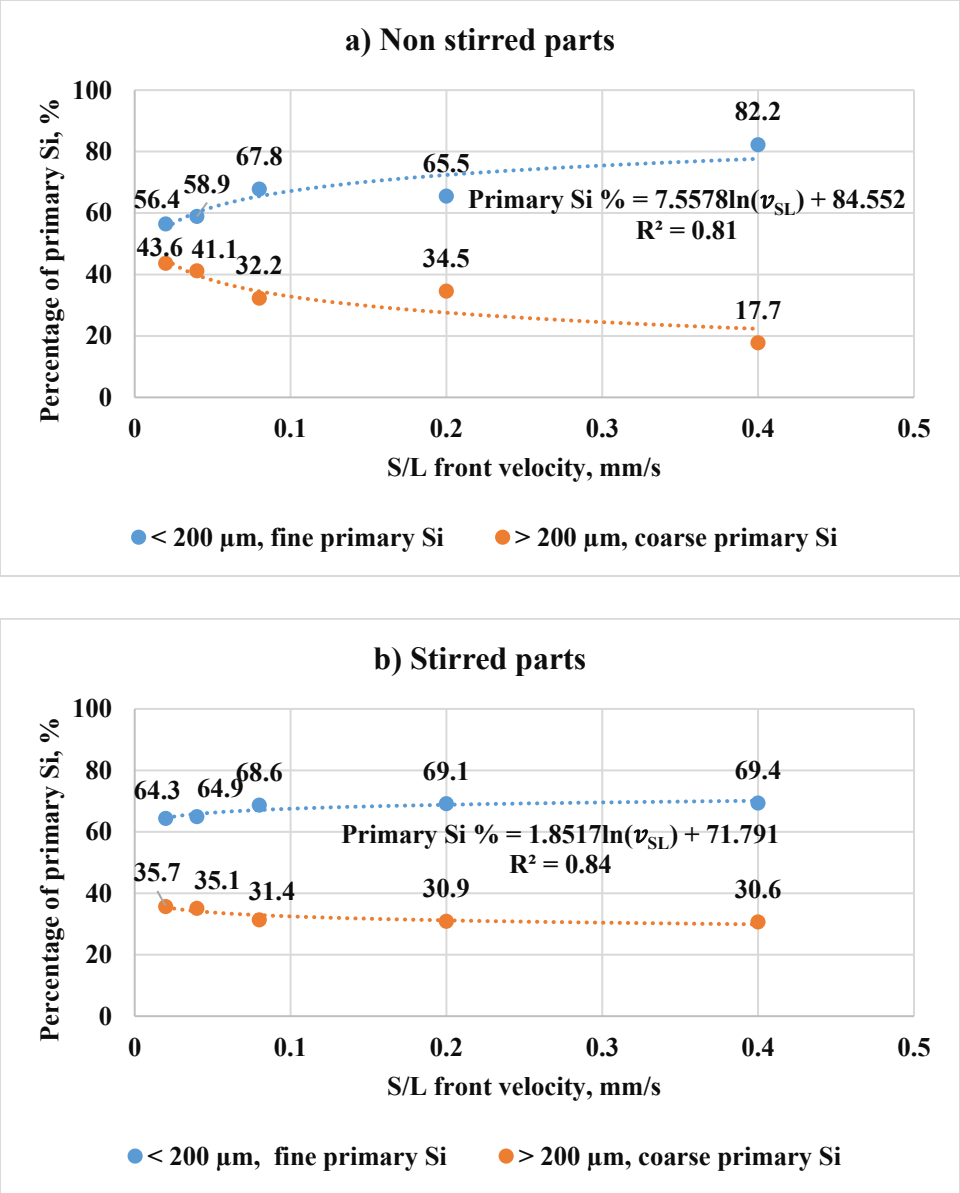

Figure 58. The percentages of the fine and coarse primary Si particles as a function of s/l front velocity in both a) non-stirred and b) stirred parts of the samples.

6.5. Claim 5. The impact of the s/l front velocity on the primary Si morphology

Claim 5.a. Effect of s/l front velocity on dendritic, star-like like and polyhedral primary Si

In the non-stirred parts, increasing the s/l front velocity from 0.02 mm/s to 0.40 mm/s leads to a decrease in dendritic primary Si particles from 51.4% to 15.7%, while the percentage of star-like particles increases from 34.6% to 73.5%. The percentage of polyhedral particles is almost the same, around 12% ± 2. In the stirred parts, the percentages of dendritic, star-like, and polyhedral

primary Si are almost the same at all s/l front velocities, with approximately 29% ± 2 for dendritic particles, 56% ± 1 for star-like particles, and 29% ± 2 for polyhedral particles (**Figure 59).**

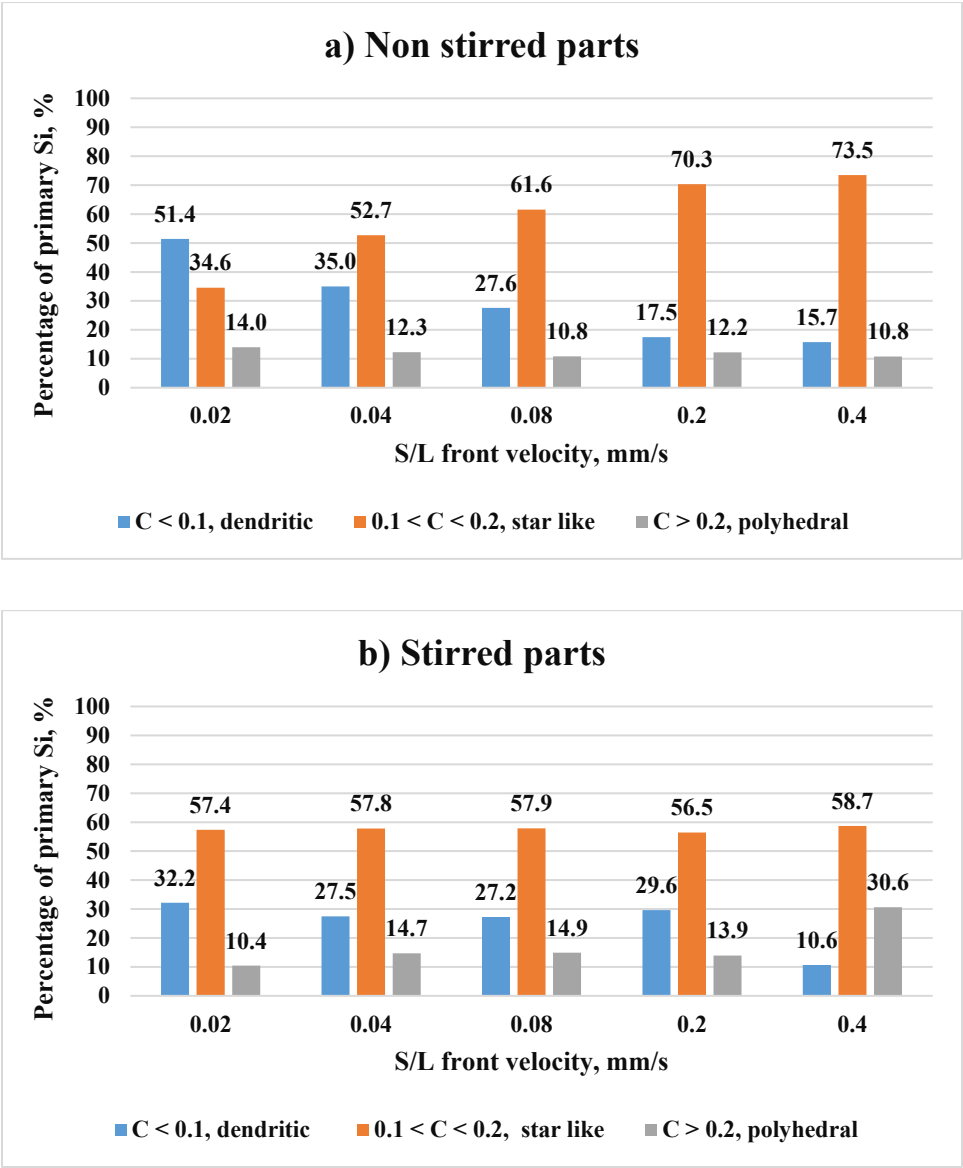

Figure 59. The percentages of the primary Si in terms of their circularity as a function of s/l front velocity in both a) non-stirred and b) stirred parts of the samples.

Claim 5.b. Effect of s/l front velocity on elongated dendritic and polyhedral primary Si

An increase in s/l front velocity leads to a reduction in elongated dendritic primary Si particles from 26.6% to 6.9% and in elongated polyhedral particles from 6.8% to 0.0%. Conversely, the percentage of equiaxed dendritic particles increases from 73.4% to 93.1%, and equiaxed polyhedral particles from 93.2% to 100% in non-stirred parts (**Figures 60 and 61**). In stirred parts,

an increase in s/l front velocity results in a reduction in elongated dendritic primary Si from 35.1% to 0.0%, and elongated polyhedral particles from 16.7% to 0.0%, while equiaxed dendritic particles increases from 64.9% to 100%, and equiaxed polyhedral particles from 83.3% to 100%.

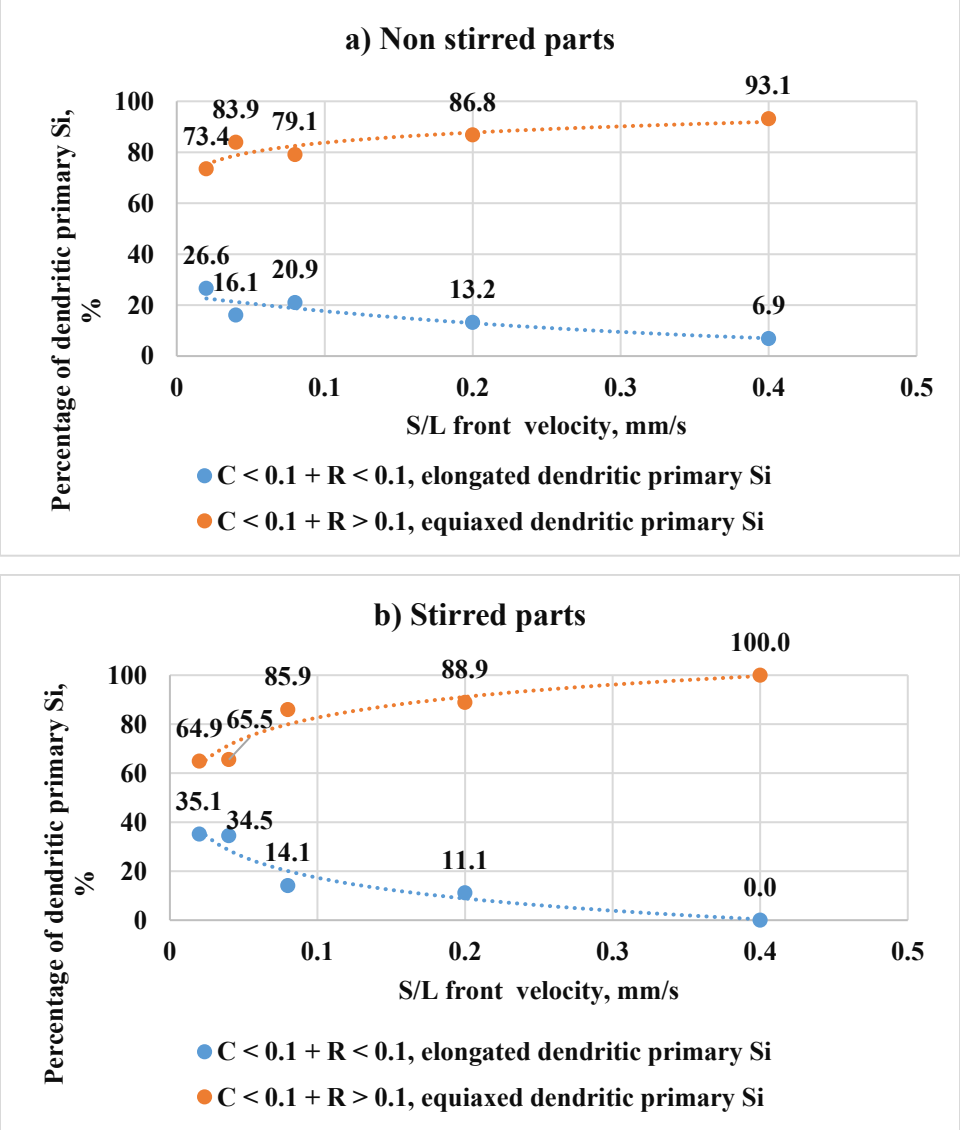

Figure 60. The percentages of the elongated and equiaxed dendritic primary Si as a function of s/l front velocity in a) non-stirred and b) stirred parts of the samples.

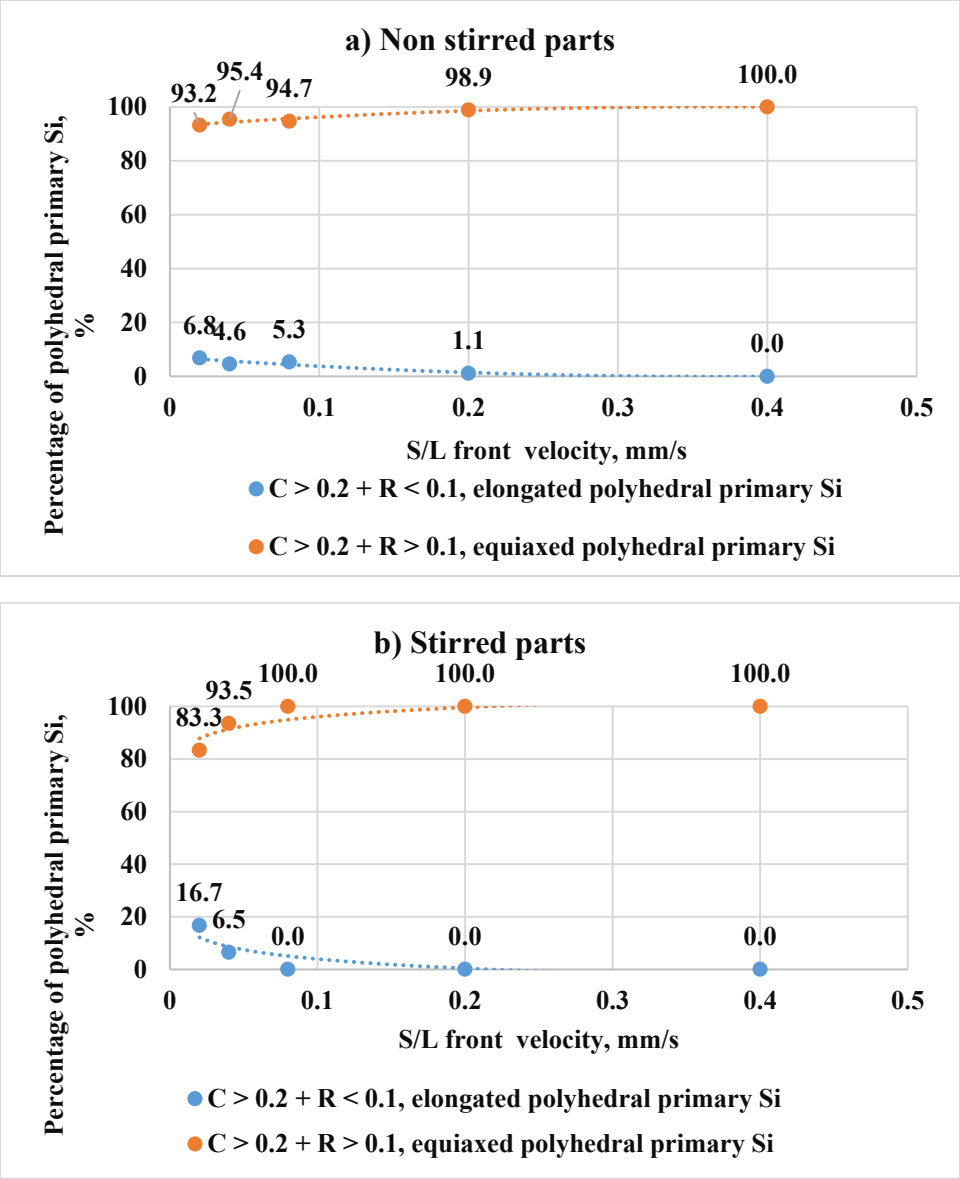

Figure 61. The percentages of the elongated and equiaxed polyhedral primary Si as a function of s/l front velocity in a) non-stirred and b) stirred parts of the samples.

6.6. Clim 6: The s/l front velocity and RMF affect the macro segregation

Claim 6.a. Macro segregation patterns under RMF and increasing s/l front velocity

In hypereutectic Al-Si alloys, macro-segregation patterns are strongly influenced by s/l front velocity and RMF. Lower velocities promote Si diffusion, producing larger primary Si at the bottom. Early solidified regions contain more and larger primary Si than later-solidified ones, with

size and volume decreasing as velocity increases (**Figure 62**). RMF-driven azimuthal and axial flows redistribute primary Si toward sample edges, altering the macrostructure (**Figure 63**).

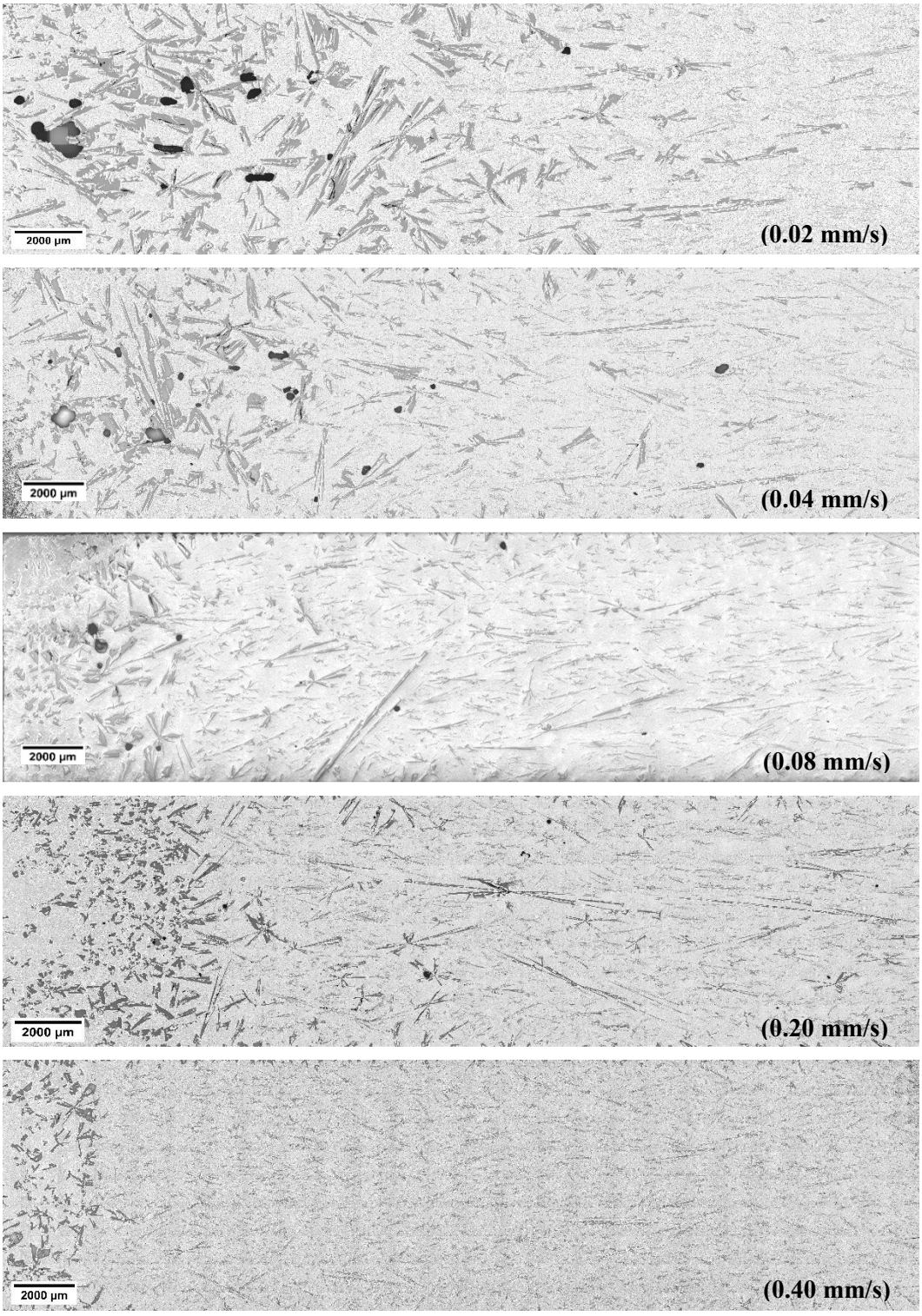

Figure 62. The macrostructure of the non-stirred parts of the Al-18 wt.% Si hypereutectic samples at different s/l front velocities: a) 0.02 mm/s, b) 0.04 mm/s, c) 0.08 mm/s, d) 0.20 mm/s and e) 0.40 mm/s.

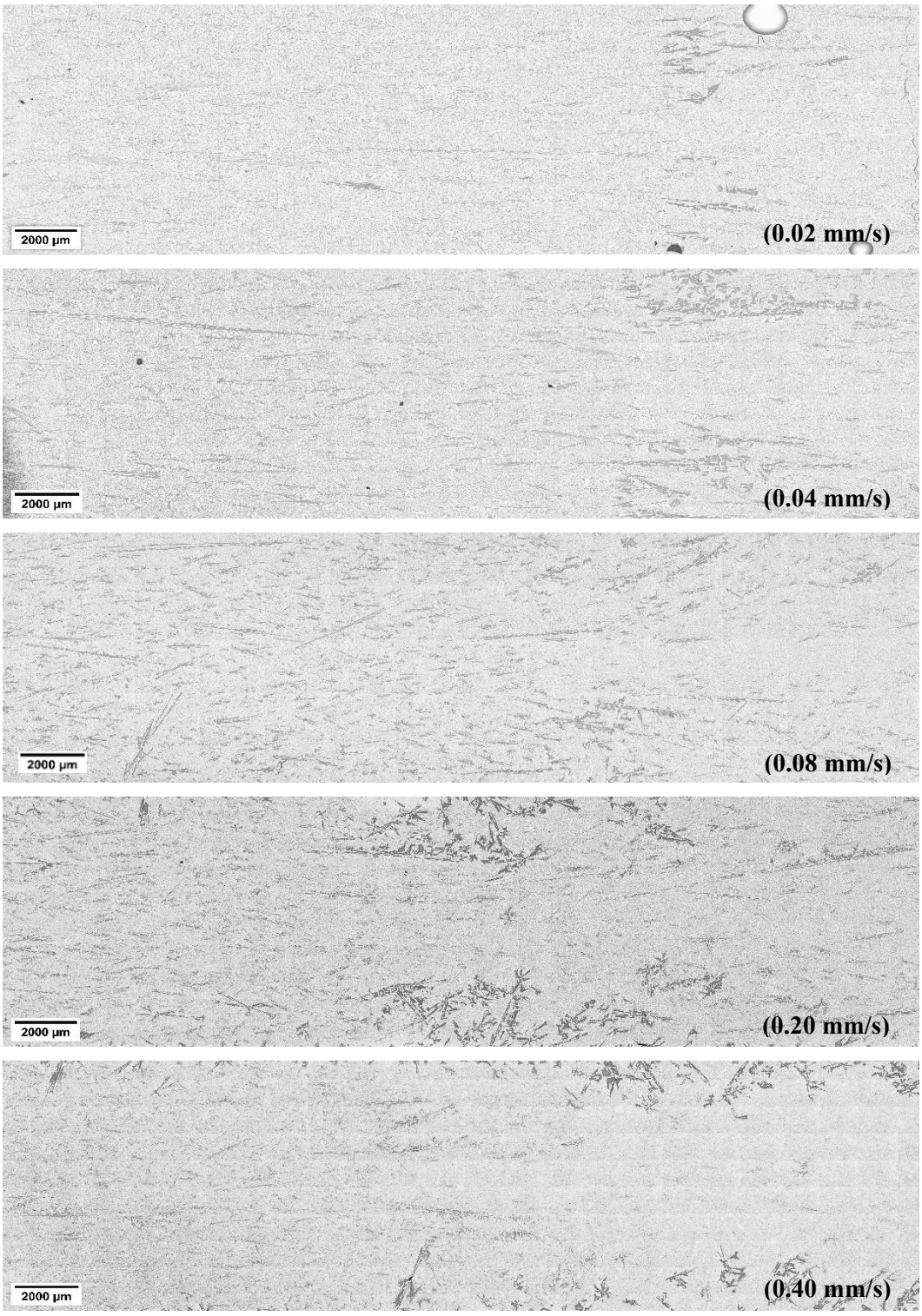

Figure 63. The macrostructure of the area of starting to stir of the Al-18 wt.% Si hypereutectic samples at different s/l front velocities: a) 0.02 mm/s, b) 0.04 mm/s, c) 0.08 mm/s, d) 0.20 mm/s and e) 0.40 mm/s.

Claim 6. b. Increasing the s/l front velocity affects the volume fraction of the eutectic structure and the primary Si phase.

Increasing s/l front velocity from 0.02 mm/s to 0.40 mm/s during solidification decreases the primary Si area fraction and increases eutectic structure area fraction in non-stirred parts, while in stirred parts, it raises the primary Si area fraction and reduces eutectic structure (**Figure 64**).

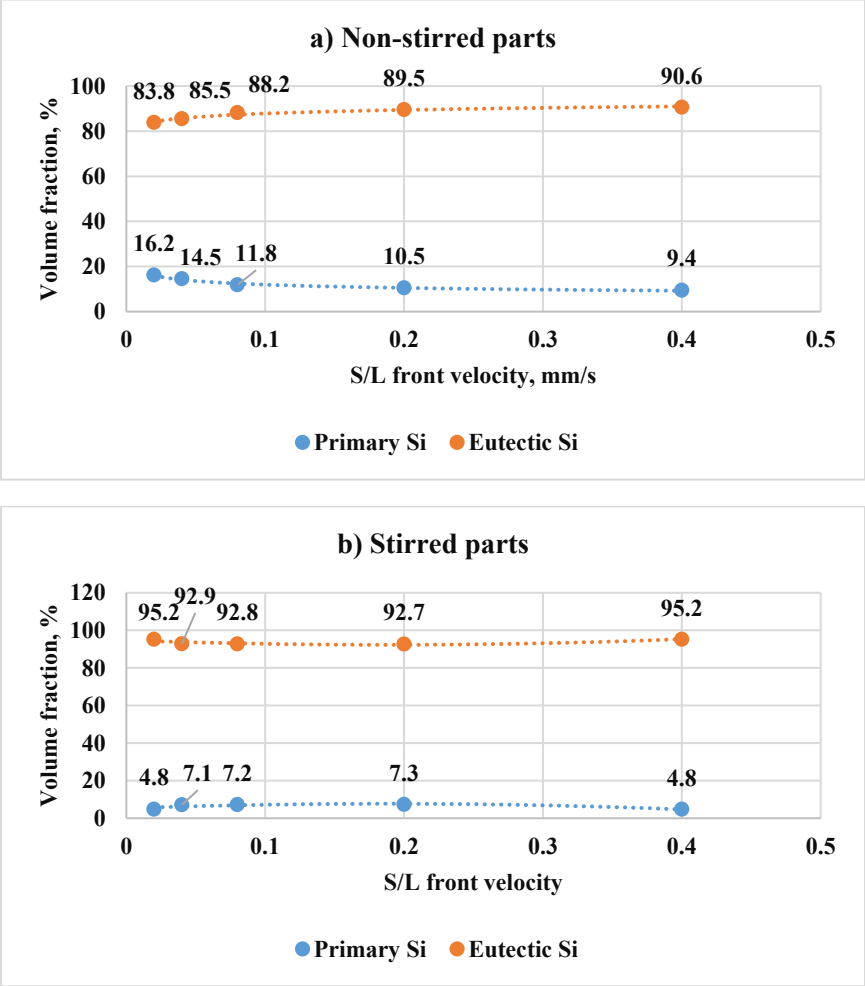

Figure 64. The area fraction of the eutectic structure and primary Si phase as a function of s/l front velocity in a) non-stirred and b) stirred parts of the samples.

Clim 6.c: Increasing the s/l front velocity decreases the macro segregation percentage in the hypereutectic Al-18 wt.% Si alloy.

Increasing the s/l front velocity from 0.02 mm/s to 0.40 mm/s reduces the macro segregation of primary Si in the hypereutectic Al–18 wt.% Si alloy, as evidenced by a decrease in the variation of primary Si area fraction across the solidification path.

For low velocities (0.02 mm/s and 0.04 mm/s), the area fraction of primary Si varies widely, from ~30% near the start of solidification to below 10% at the end—a range of approximately 20 percentage points, indicating strong macro segregation (**Figure 65**).

At higher velocities (0.08 mm/s to 0.4 mm/s), the variation is significantly reduced. For example, at 0.4 mm/s, the area fraction decreases modestly from ~16% to ~11%, resulting in a range of just 5 percentage points, reflecting a more uniform distribution.

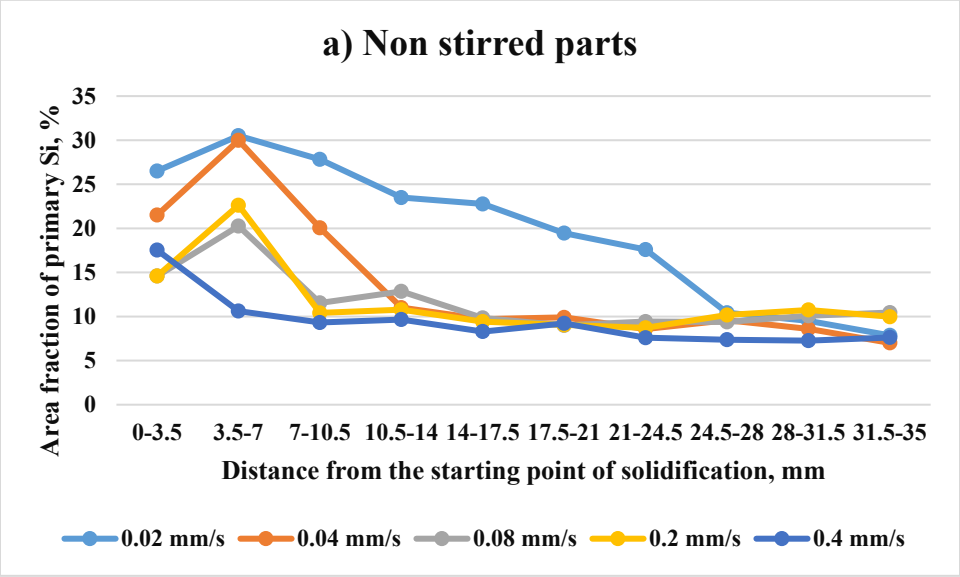

Figure 65. The area fraction of the primary Si along the growth length in the non-stirred sections of the Al-18 wt.% Si hypereutectic samples, measured at different front velocities: 0.02 mm/s, 0.04 mm/s, 0.08 mm/s, 0.20 mm/s, and 0.40 mm/s.

7. Author's Publications

- **Journals Articles**

1. D. Zakaraia, A. Roósz, A. Rónaföldi, and Z. Veres, "Influence of Magnetic Stirring and Eutectic Front Velocity on the Solidified Microstructure of Al-18 wt.% Si Alloy," *Materials (Basel).*, vol. 17, no. 24, 2024, doi: 10.3390/ma17246029.
2. D. Zakaraia, A. Roósz, A. Rónaföldi, and Z. Veres, "The Effect of Forced Melt Flow by a Rotating Magnetic Field and Solid/Liquid Front Velocity on the Size and Morphology of Primary Si in a Hypereutectic Al-18 wt.% Si Alloy," *Materials (Basel).*, vol. 18, no. 11, pp. 1–17, 2025, doi: 10.3390/ma18112581.
3. D. Zakaraia, A. Roósz, A. Rónaföldi, and Z. Veres, "The effect of rotating magnetic field on the microstructure of hypereutectic Al-Si alloy," PhD Students Alm., vol. 1, pp. 283–288, 2022, doi: https://avk.uni-miskolc.hu/kerpely-antal-doktori-iskola/kerpely-almanach/.
4. D. Zakaraia, A. Roósz, A. Rónaföldi, and Z. Veres, "An Overview of Structure, Characteristics, and Applications of Al-Si Alloys," PhD Students Alm., vol. 1, 2023, doi: https://avk.uni-miskolc.hu/kerpely-antal-doktori-iskola/kerpely-almanach/.
5. D. Zakaraia, A. Roósz, A. Rónaföldi, and Z. Veres, "Review of Morphologies of Primary Silicon in Hypereutectic Al-Si Alloys," PhD Students Alm. 1, vol. 1, pp. 71–75, 2024, doi: https://avk.uni-miskolc.hu/kerpely-antal-doktori-iskola/kerpely-almanach/.

- **Oral and Poster Presentations**

1. D. Zakaraia, A. Roósz, A. Rónaföldi, and Z. Veres, "A new qualification method of the primary Si in Al-Si alloys," The 8th International Conference on Solidification and Gravity., 2024.
2. D. Zakaraia, A. Roósz, A. Rónaföldi, and Z. Veres, "Effect of forced melt flow on hypereutectic Al-Si alloys," Hungarian Science Day., 2022.

8. References

[1] H. R. Kotadia and A. Das, "Modification of solidification microstructure in hypo- and hyper-eutectic Al-Si alloys under high-intensity ultrasonic irradiation," *J. Alloys Compd.*, vol. 620, pp. 1–4, 2015, doi: 10.1016/j.jallcom.2014.09.089.

[2] A. G. Rao, V. P. Deshmukh, N. Prabhu, and B. P. Kashyap, "Enhancing the machinability of hypereutectic Al-30Si alloy by friction stir processing," *J. Manuf. Process.*, vol. 23, pp. 130–134, 2016, doi: 10.1016/j.jmapro.2016.06.008.

[3] K. Al-helal, "New Approaches to Casting Hypereutectic Al-Si Alloys to Achieve New Approaches to Casting Hypereutectic Al-Si Alloys to Achieve Simultaneous Refinement of Primary Silicon and Modification of Eutectic Silicon A thesis submitted for the degree of Doctor of ," no. November, 2020, doi: 10.13140/RG.2.2.32471.70561.

[4] M. Haghshenas and J. Jamali, "Assessment of circumferential cracks in hypereutectic Al-Si clutch housings," *Case Stud. Eng. Fail. Anal.*, vol. 8, pp. 11–20, 2017, doi: 10.1016/j.csefa.2016.11.003.

[5] N. Tenekedjiev and J. E. Gruzleski, "Hypereutectic Aluminium-Silicon Casting Alloys—A Review," *Cast Met.*, vol. 3, no. 2, pp. 96–105, 1990, doi: 10.1080/09534962.1990.11819026.

[6] S. Hegde and K. N. Prabhu, "Modification of eutectic silicon in Al-Si alloys," *J. Mater. Sci.*, vol. 43, no. 9, pp. 3009–3027, 2008, doi: 10.1007/s10853-008-2505-5.

[7] J. Chang, I. Moon, and C. Choi, "Refinement of cast microstructure of hypereutectic Al-Si alloys through the addition of rare earth metals," *J. Mater. Sci.*, vol. 33, no. 20, pp. 5015–5023, 1998, doi: 10.1023/A:1004463125340.

[8] H. Ye, "An overview of the development of Al-Si-alloy based material for engine applications," *J. Mater. Eng. Perform.*, vol. 12, no. 3, pp. 288–297, 2003, doi: 10.1361/105994903770343132.

[9] V. S. Zolotorevsky, N. A. Belov, M. V. Glazoff, V. S. Zolotorevsky, N. A. Belov, and M. V. Glazoff, *Chapter one – Alloying Elements and Dopants: Phase Diagrams*. 2007.

[10] V. V. K. N. Prabhu, “Review of Microstructure Evolution in Hypereutectic Al – Si Alloys and its Effect on Wear Properties,” vol. 67, pp. 1–18, 2014, doi: 10.1007/s12666-013-0327-x.

[11] D. Zakaraia, A. Roósz, A. Rónaföldi, and Z. Veres, “An Overview of Structure, Characteristics, and Applications of Al-Si Alloys,” *PhD Students Alm.*, vol. 1, 2023, doi: https://avk.uni-miskolc.hu/kerpely-antal-doktori-iskola/kerpely-almanach/.

[12] M. W. Ullah and T. Carlberg, “Silicon crystal morphologies during solidification refining from AlSi melts,” *J. Cryst. Growth*, vol. 318, no. 1, pp. 212–218, 2011, doi: 10.1016/j.jcrysgro.2010.10.084.

[13] C. L. Xu and Q. C. Jiang, “Morphologies of primary silicon in hypereutectic Al-Si alloys with melt overheating temperature and cooling rate,” *Mater. Sci. Eng. A*, vol. 437, no. 2, pp. 451–455, 2006, doi: 10.1016/j.msea.2006.07.088.

[14] M. H. and N. L. H.Fredriksson, “The modification of Aluminium-Silicon Alloys by Sodium,” *J. Inst. Met.*, vol. 101, pp. 285–299, 1973.

[15] J. Liu and R. Elliott, “Irregular eutectic solidification,” *Mater. Sci. Eng. A*, vol. 173, no. 1–2, pp. 129–132, 1993, doi: 10.1016/0921-5093(93)90201-O.

[16] D. Zakaraia, A. Roósz, A. Rónaföldi, and Z. Veres, “Influence of Magnetic Stirring and Eutectic Front Velocity on the Solidified Microstructure of Al-18 wt.% Si Alloy,” *Materials (Basel).*, vol. 17, no. 24, 2024, doi: 10.3390/ma17246029.

[17] D. Lu, Y. Jiang, G. Guan, R. Zhou, Z. Li, and R. Zhou, “Refinement of primary Si in hypereutectic Al-Si alloy by electromagnetic stirring,” *J. Mater. Process. Technol.*, vol. 189, no. 1–3, pp. 13–18, 2007, doi: 10.1016/j.jmatprotec.2006.12.008.

[18] K. Tiwari, G. Gautam, N. Kumar, A. Mohan, and S. Mohan, “Effect of Primary Silicon Refinement on Mechanical and Wear Properties of a Hypereutectic Al-Si Alloy,” *Silicon*, vol. 10, no. 5, pp. 2227–2239, 2018, doi: 10.1007/s12633-017-9755-2.

[19] W. J. Kyffin, W. M. Rainforth, and H. Jones, “Effect of phosphorus additions on the spacing between primary silicon particles in a Bridgman solidified hypereutectic Al-Si alloy,” *J. Mater. Sci.*, vol. 36, no. 11, pp. 2667–2672, 2001, doi: 10.1023/A:1017904627733.

[20] F. Yilmaz, O. A. Atasoy, and R. Elliott, “Growth structures in aluminium-silicon alloys II. The influence of strontium,” *J. Cryst. Growth*, vol. 118, no. 3–4, pp. 377–384, 1992, doi: 10.1016/0022-0248(92)90086-X.

[21] D. H. Xiao, M. Song, B. Y. Huang, J. H. Yi, Y. H. He, and Y. M. Li, “Effect of Sc addition on microstructure and mechanical properties of Al-Cu-Mg-Ag-Zr alloy,” *Mater. Sci. Technol.*, vol. 25, no. 6, pp. 747–752, 2009, doi: 10.1179/174328408X326101.

[22] X. Liu, Y. Wu, and X. Bian, “The nucleation sites of primary Si in Al-Si alloys after addition of boron and phosphorus,” *J. Alloys Compd.*, vol. 391, no. 1–2, pp. 90–94, 2005, doi: 10.1016/j.jallcom.2004.09.003.

[23] Q. Wang, C. J. Wang, T. Liu, K. Wang, and J. C. He, “Control of solidified structures in aluminum-silicon alloys by high magnetic fields,” *J. Mater. Sci.*, vol. 42, no. 24, pp. 10000–10006, 2007, doi: 10.1007/s10853-007-2050-7.

[24] D. Zakaraia, A. Roósz, A. Rónaföldi, and Z. Veres, “The Effect of Forced Melt Flow by a Rotating Magnetic Field and Solid/Liquid Front Velocity on the Size and Morphology of Primary Si in a Hypereutectic Al-18 wt.% Si Alloy,” *Materials (Basel).*, vol. 18, no. 11, pp. 1–17, 2025, doi: 10.3390/ma18112581.

[25] C. E. Suarez, “Formation of Microstructure in Al-Si Alloys under Ultrasonic Melt Treatment,” *Light Met. 2012*, pp. 1–1407, 2012, doi: 10.1002/9781118359259.

[26] Z. Veres, A. Roósz, A. Rónaföldi, A. Sycheva, and M. Svéda, “The effect of melt flow induced by RMF on the meso- and micro-structure of unidirectionally solidified Al–7wt.% Si alloy Benchmark experiment under magnetic stirring,” *J. Mater. Sci. Technol.*, vol. 103, no. October, pp. 197–208, 2022, doi: 10.1016/j.jmst.2021.06.060.

[27] Y. Xu, Y. Deng, D. Casari, R. H. Mathiesen, and Y. Li, “In-situ X-radiographic study of nucleation and growth behaviour of primary silicon particles during solidification of a hypereutectic Al-Si alloy,” *J. Alloys Compd.*, vol. 832, p. 154948, 2020, doi: 10.1016/j.jallcom.2020.154948.

[28] D. Zakaraia, A. Roósz, A. Rónaföldi, and Z. Veres, “Review of Morphologies of Primary Silicon in Hypereutectic Al-Si Alloys,” *PhD Students Alm.*, vol. 1, pp. 71–75, 2024, doi:

https://avk.uni-miskolc.hu/kerpely-antal-doktori-iskola/kerpely-almanach/.

[29] J.]. C. Weiss and C. R. Loper, “Primary Silicon in Hypereutectic Aluminum-Silicon Casting Alloys,” *AFS Trans*, vol. 1987.

[30] V. Vijeesh and K. N. Prabhu, “Review of microstructure evolution in hypereutectic Al-Si alloys and its effect on wear properties,” *Trans. Indian Inst. Met.*, vol. 67, no. 1, pp. 1–18, 2014, doi: 10.1007/s12666-013-0327-x.

[31] H. S. Kang, W. Y. Yoon, K. H. Kim, M. H. Kim, and Y. P. Yoon, “Microstructure selections in the undercooled hypereutectic Al-Si alloys,” *Mater. Sci. Eng. A*, vol. 404, no. 1–2, pp. 117–123, 2005, doi: 10.1016/j.msea.2005.05.041.

[32] Y. T. Pei and J. T. M. De Hosson, “Five-fold branched Si particles in laser clad AlSi functionally graded materials,” *Acta Mater.*, vol. 49, no. 4, pp. 561–571, 2001, doi: 10.1016/S1359-6454(00)00364-5.

[33] H. Yi and D. Zhang, “Morphologies of Si phase and La-rich phase in as-cast hypereutectic Al-Si-xLa alloys,” *Mater. Lett.*, vol. 57, no. 16–17, pp. 2523–2529, 2003, doi: 10.1016/S0167-577X(02)01305-8.

[34] D. Liang, Y. Bayraktar, and H. Jones, “Formation and segregation of primary silicon in Bridgman solidified Al-18.3 wt% Si alloy,” *Acta Metall. Mater.*, vol. 43, no. 2, pp. 579–585, 1995, doi: 10.1016/0956-7151(94)00287-R.

[35] C. L. Xu, H. Y. Wang, C. Liu, and Q. C. Jiang, “Growth of octahedral primary silicon in cast hypereutectic Al-Si alloys,” *J. Cryst. Growth*, vol. 291, no. 2, pp. 540–547, 2006, doi: 10.1016/j.jcrysgro.2006.03.044.

[36] K. Jackson, “Liquid metals and solidification,” Cleveland, Ohio: American Society for Metals, 1958.

[37] D. F. W. Kurz, *Fundamentals of Solidification*. Aedermannsdorf, Switzerland: Trans Tech Publications, 1989.

[38] D. Stefanescu, *Science and Engineering of Casting Solidification*. Switzerland: Springer, 2015.

[39] C. Zener, “Kinetics of the decomposition of austenite,” *Trans. Metall. Soc. AIME*, vol. 167, pp. 550–595, 1946.

[40] K. A. Jackson and J. D. Hunt, “Lamellar and Rod Eutectic Growth,” *Trans. Metall. Soc.*, vol. 236, pp. 1129–1142, 1966.

[41] K. Al-omari and Z. Veres, “Complex characterization of irregular eutectic structure,” no. May 2022, 2020.

[42] K. Al-Omari, A. Roósz, A. Rónaföldi, and Z. Veres, “Effect of Forced Melt Flow on Al–Si Eutectic-Alloy Microstructures,” *Crystals*, vol. 12, no. 5, 2022, doi: 10.3390/cryst12050731.

[43] G. Zimmermann and A. Weiss, “Directional solidification of dendritic microstructures in microgravity and with forced melt flow,” *Microgravity Sci. Technol.*, vol. 16, no. 1, pp. 143–147, 2005, doi: 10.1007/bf02945965.

[44] S. Eckert *et al.*, “Electromagnetic melt flow control during solidification of metallic alloys,” *Eur. Phys. J. Spec. Top.*, vol. 220, no. 1, pp. 123–137, 2013, doi: 10.1140/epjst/e2013-01802-7.

[45] K. Al-Omari, A. Roósz, A. Rónaföldi, M. Svéda, and Z. Veres, “Macrosegregation Evolution in Eutectic Al-Si Alloy under the Influence of a Rotational Magnetic Field,” *Metals (Basel).*, vol. 12, no. 11, 2022, doi: 10.3390/met12111990.

[46] Z. Yan, X. Li, Z. Cao, X. Zhang, and T. Li, “Grain refinement of horizontal continuous casting of the CuNi10Fe1Mn alloy hollow billets by rotating magnetic field (RMF),” *Mater. Lett.*, vol. 62, no. 28, pp. 4389–4392, 2008, doi: 10.1016/j.matlet.2008.07.010.

[47] D. Zakaraia, A. Roósz, A. Rónaföldi, and Z. Veres, “The effect of rotating magnetic field on the microstructure of hypereutectic Al-Si alloy,” *PhD Students Alm.*, vol. 1, pp. 283–288, 2022, doi: https://avk.uni-miskolc.hu/kerpely-antal-doktori-iskola/kerpely-almanach/.

[48] X. Zuo, C. Zhao, L. Zhang, and E. Wang, “Influence of growth rate and magnetic field on microstructure and properties of directionally solidified Ag-Cu eutectic alloy,” *Materials (Basel).*, vol. 9, no. 7, 2016, doi: 10.3390/MA9070569.

[49] Y. Koçak, S. Engin, U. Böyük, and N. Maraşli, “The influence of the growth rate on the eutectic spacings, undercoolings and microhardness of directional solidified bismuth-lead eutectic alloy,” *Curr. Appl. Phys.*, vol. 13, no. 3, pp. 587–593, 2013, doi: 10.1016/j.cap.2012.10.005.

[50] P. Yan, W. Mao, J. Fan, and B. Wang, “Simultaneous refinement of primary Si and modification of eutectic Si in A390 alloy assisting by Sr-modifier and Serpentine Pouring Channel Process,” *Materials (Basel).*, vol. 12, no. 19, 2019, doi: 10.3390/ma12193109.

[51] J. C. Jie, Q. C. Zou, J. L. Sun, Y. P. Lu, T. M. Wang, and T. J. Li, “Separation mechanism of the primary Si phase from the hypereutectic Al-Si alloy using a rotating magnetic field during solidification,” *Acta Mater.*, vol. 72, pp. 57–66, 2014, doi: 10.1016/j.actamat.2014.03.031.

[52] A. Abdallah and Z. Veres, “Effect of Solid/Liquid and Eutectic Front Velocities on Microstructure Evolution in Al-20%Cu Alloys,” no. July, 2024, doi: 10.3390/cryst14070638.

[53] D. G. Eskin, R. Nadella, and L. Katgerman, “Effect of different grain structures on centerline macrosegregation during direct-chill casting,” *Acta Mater.*, vol. 56, no. 6, pp. 1358–1365, 2008, doi: 10.1016/j.actamat.2007.11.021.

[54] S. Boden, S. Eckert, and G. Gerbeth, “Visualization of freckle formation induced by forced melt convection in solidifying GaIn alloys,” *Mater. Lett.*, vol. 64, no. 12, pp. 1340–1343, 2010, doi: 10.1016/j.matlet.2010.03.044.

[55] L. Yuan and P. D. Lee, “A new mechanism for freckle initiation based on microstructural level simulation,” *Acta Mater.*, vol. 60, no. 12, pp. 4917–4926, 2012, doi: 10.1016/j.actamat.2012.04.043.

[56] G. Zimmermann, A. Weiss, and Z. Mbaya, “Effect of forced melt flow on microstructure evolution in AlSi7Mg0.6 alloy during directional solidification,” *Mater. Sci. Eng. A*, vol. 413–414, pp. 236–242, 2005, doi: 10.1016/j.msea.2005.09.049.

[57] K. Zaïdat *et al.*, “Directional solidification of refined Al-3.5 wt% Ni under natural convection and under a forced flow driven by a travelling magnetic field,” *J. Cryst. Growth*,

vol. 275, no. 1–2, 2005, doi: 10.1016/j.jcrysgro.2004.11.182.

[58] A. Noeppel *et al.*, “Influence of forced/natural convection on segregation during the directional solidification of Al-based binary alloys,” *Metall. Mater. Trans. B Process Metall. Mater. Process. Sci.*, vol. 41, no. 1, pp. 193–208, 2010, doi: 10.1007/s11663-009-9311-6.

[59] B. Willers *et al.*, “Efficient melt stirring using pulse sequences of a rotating magnetic field: Part II. Application to solidification of Al-Si alloys,” *Metall. Mater. Trans. B Process Metall. Mater. Process. Sci.*, vol. 39, no. 2, pp. 304–316, 2008, doi: 10.1007/s11663-008-9126-x.

[60] S. Hu *et al.*, “Effect of a magnetic field on macro segregation of the primary silicon phase in hypereutectic Al-Si alloy during directional solidification,” *J. Alloys Compd.*, vol. 722, pp. 108–115, 2017, doi: 10.1016/j.jallcom.2017.06.084.

[61] Q. Zou *et al.*, “Controlling segregation behavior of primary Si in hypereutectic Al-Si alloy by electromagnetic stirring,” *Metals (Basel).*, vol. 10, no. 9, pp. 1–13, 2020, doi: 10.3390/met10091129.

[62] A. Rónaföldi, J. Kovács, and A. Roósz, “Solidification Facility Equipped with a Magnetohydrodynamic Stirrer,” no. May, 2006.

[63] C. Shanthi, R. Kingsley Porpatham, and N. Pappa, “Image analysis for particle size distribution,” *Int. J. Eng. Technol.*, vol. 6, no. 3, pp. 1340–1345, 2014.

[64] F. Tiago and W. Rasband, “ImageJ User Guide.”

[65] X. Bai, B. Ban, J. Li, Z. Peng, and J. Chen, “Distribution Behavior of B and P during Al-Si Melt Directional Solidification with Open-Ended Crucible,” *High Temp. Mater. Process.*, vol. 37, no. 3, pp. 201–208, 2018, doi: 10.1515/htmp-2016-0127.

[66] D. Jie, C. Jianzhong, and D. Wenjiang, “Theoretical discussion of the effect of a low-frequency electromagnetic vibrating field on the as-cast microstructures of DC Al-Zn-Mg-Cu-Zr ingots,” *J. Cryst. Growth*, vol. 295, no. 2, pp. 179–187, 2006, doi: 10.1016/j.jcrysgro.2006.07.025.

[67] H. Kaya, U. Böyük, E. Çadirli, and N. Maraşli, “Unidirectional solidification of aluminium-nickel eutectic alloy,” *Kov. Mater.*, vol. 48, no. 5, pp. 291–300, 2010, doi: 10.4149/km_2010_5_291.

[68] X. Li, Y. Fautrelle, A. Gagnoud, Z. Ren, and R. Moreau, “EBSD Study of the Influence of a High Magnetic Field on the Microstructure and Orientation of the Al-Si Eutectic During Directional Solidification,” *Metall. Mater. Trans. A Phys. Metall. Mater. Sci.*, vol. 47, no. 6, pp. 2952–2963, 2016, doi: 10.1007/s11661-016-3432-8.

[69] B. Korojy and H. Fredriksson, “On solidification of hypereutectic Al-Si alloys,” *Trans. Indian Inst. Met.*, vol. 62, no. 4–5, pp. 361–365, 2009, doi: 10.1007/s12666-009-0066-1.

[70] K. Kobayashi and L. M. Hogan, “Fivefold twinned silicon crystals grown in an A1–16 wt.% Si melt,” *Philos. Mag. A Phys. Condens. Matter, Struct. Defects Mech. Prop.*, vol. 40, no. 3, pp. 399–407, 1979, doi: 10.1080/01418617908234848.

[71] W. Wang, X. Bian, J. Qin, and S. I. Syliusarenko, “The atomic-structure changes in AI-16 Pct Si alloy above the liquidus,” *Metall. Mater. Trans. A Phys. Metall. Mater. Sci.*, vol. 31, no. 9, pp. 2163–2168, 2000, doi: 10.1007/s11661-000-0134-y.

9. Appendix

9.1. Determination of s/l and eutectic front velocities

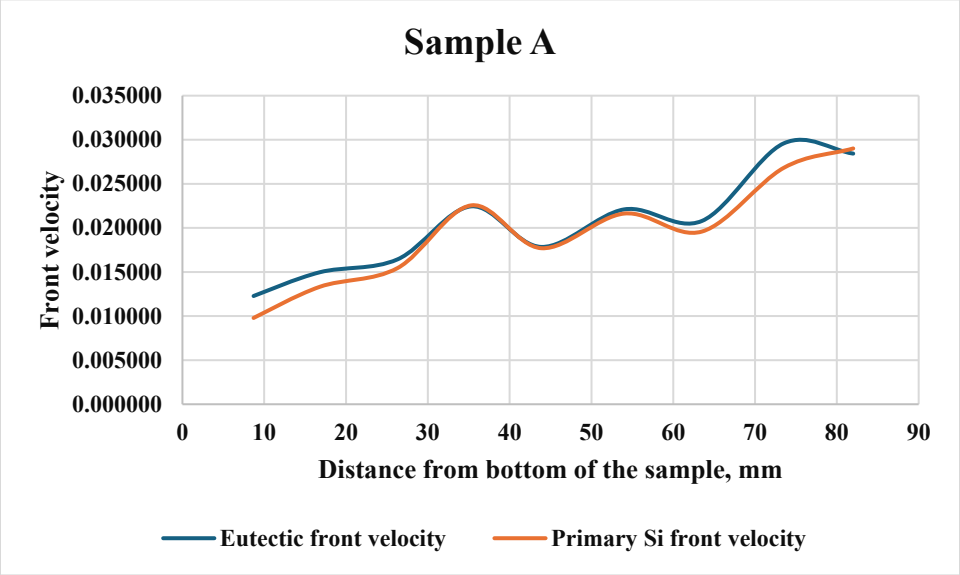

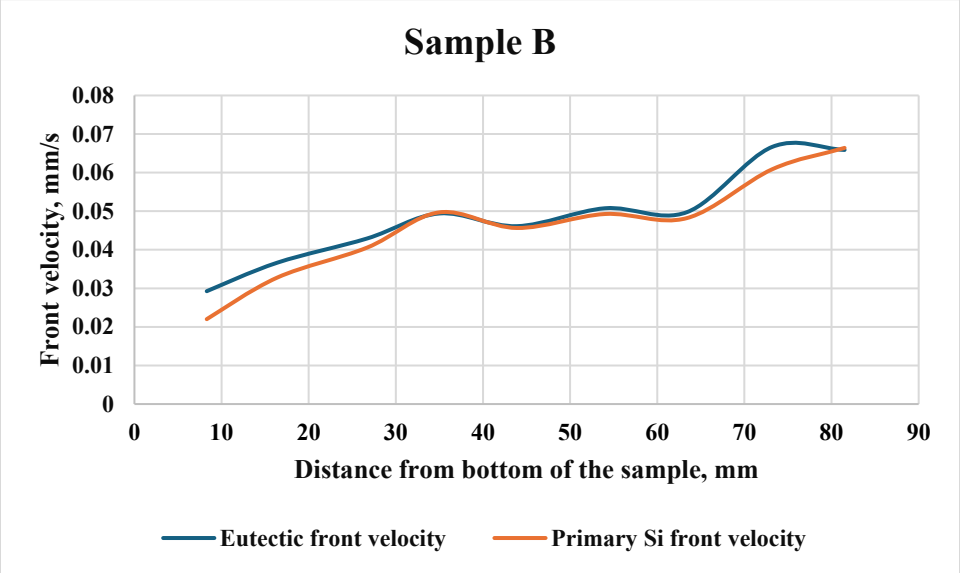

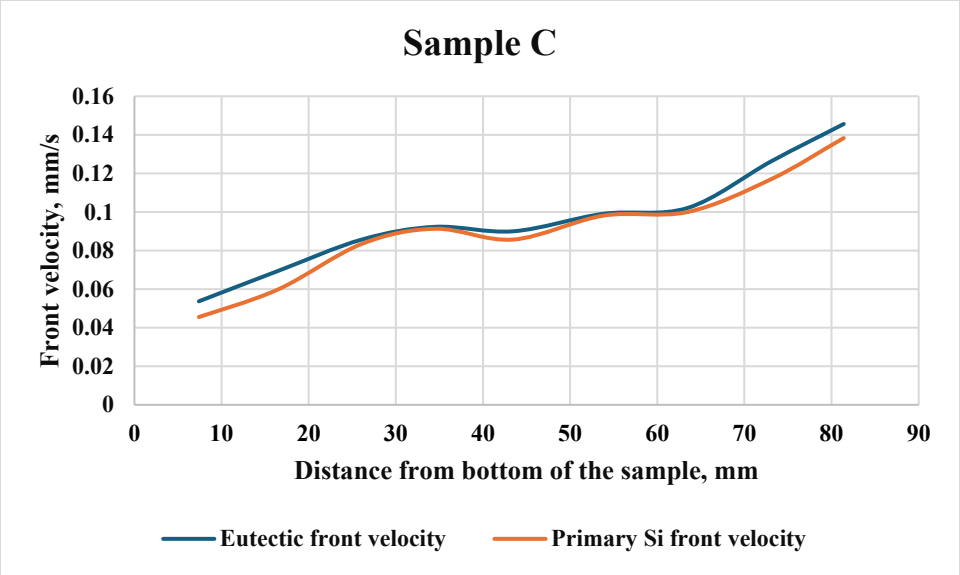

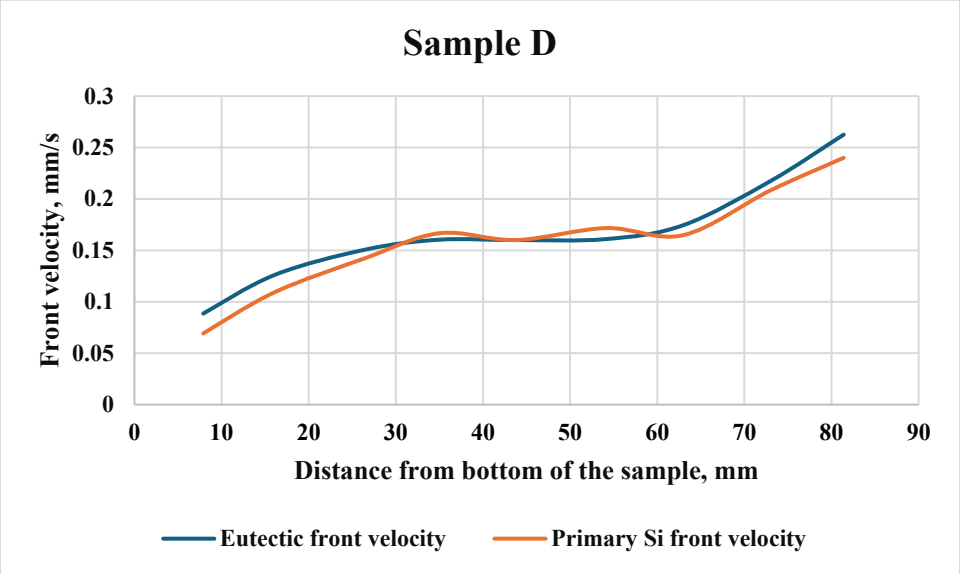

Figure 66. The velocities of solid/liquid and eutectic fronts as a function of distance from the bottom of the sample for samples A, B, C, and D.

9.2. Curves of Eutectic Lamellas Length

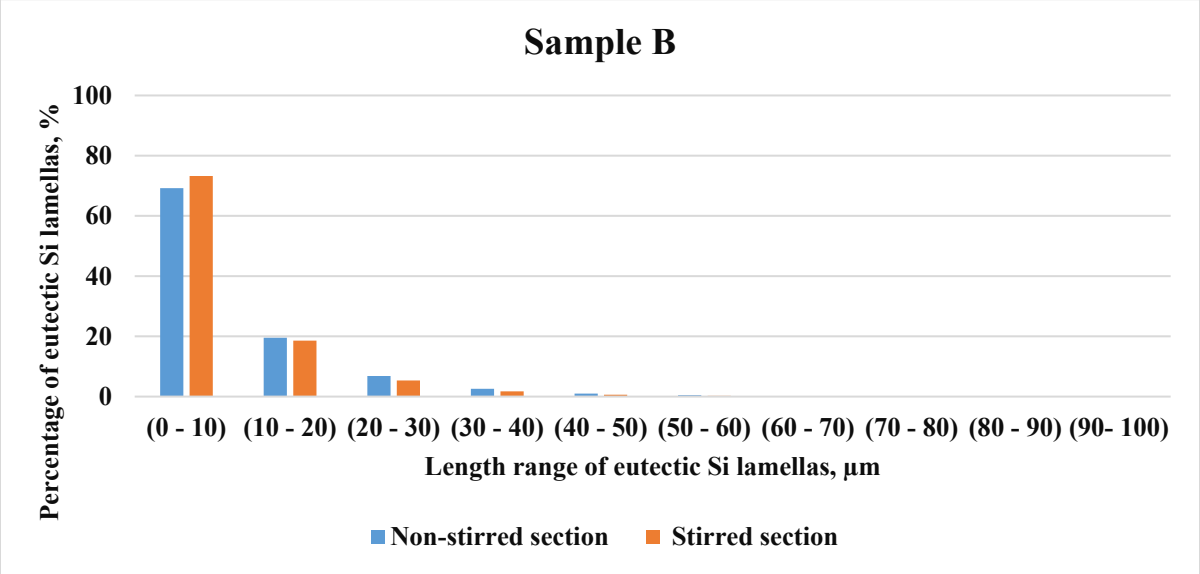

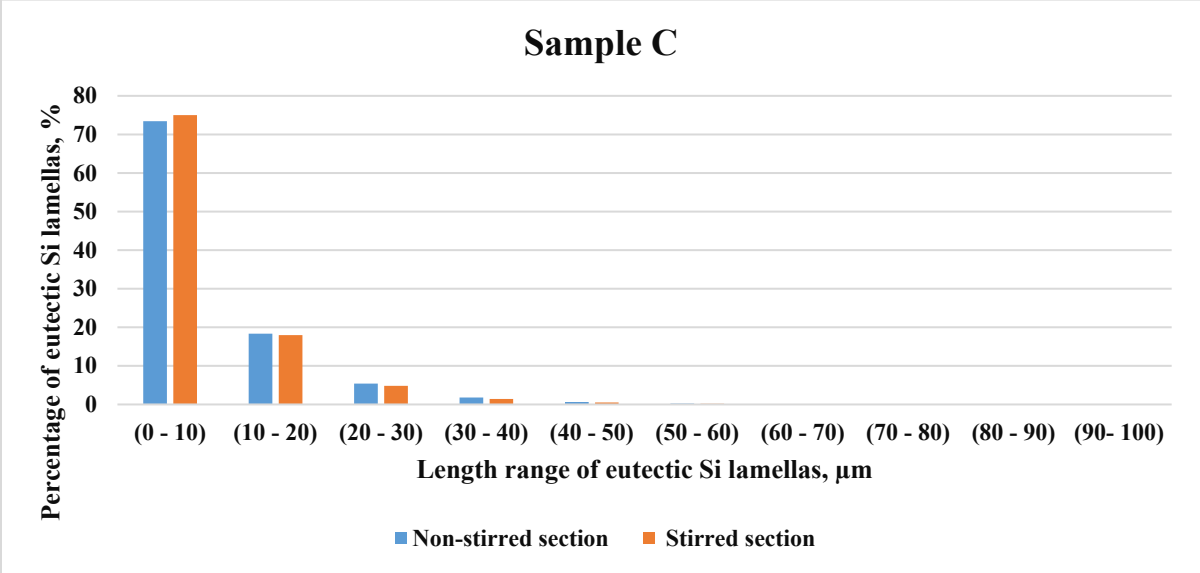

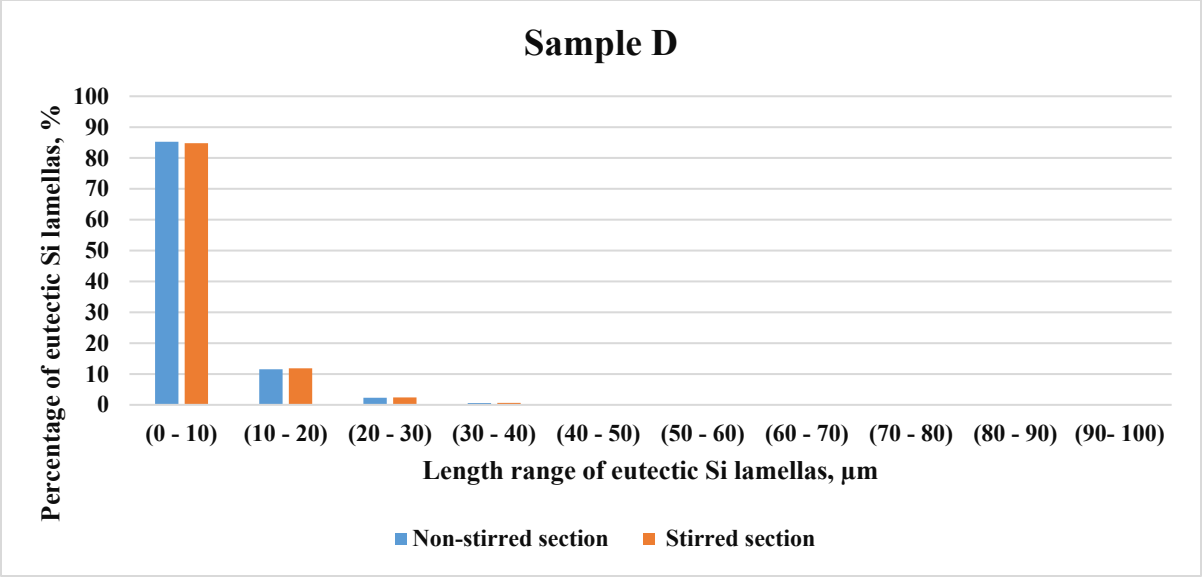

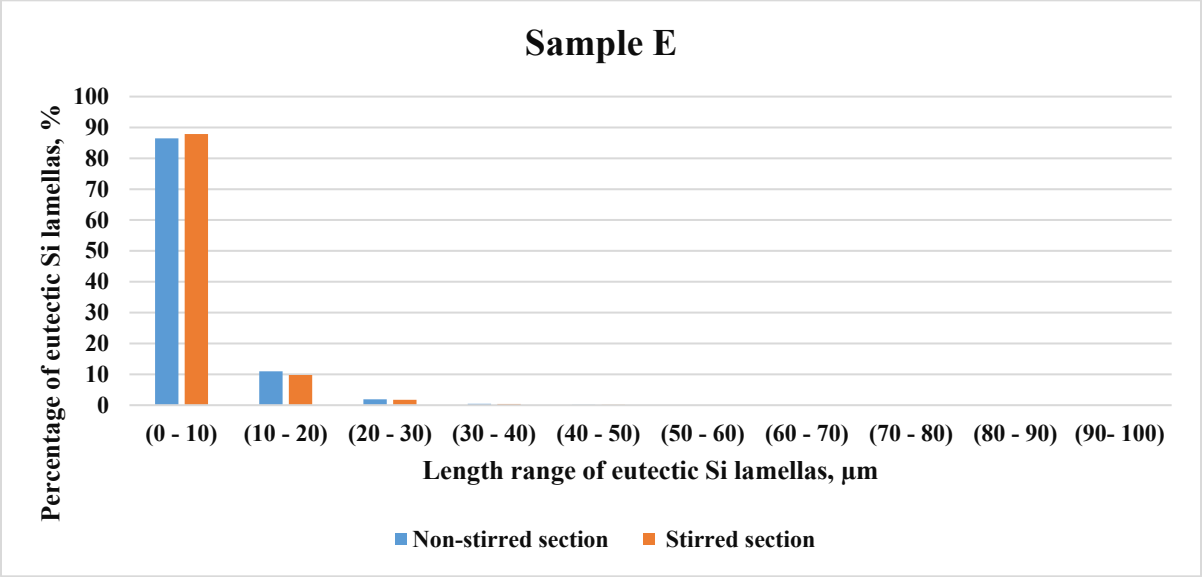

Figure 67. The percentage of the eutectic Si lamellas as a function of their length range in the stirred and non-stirred parts of the samples B, C, D, and E.

9.3. Angle distribution curves

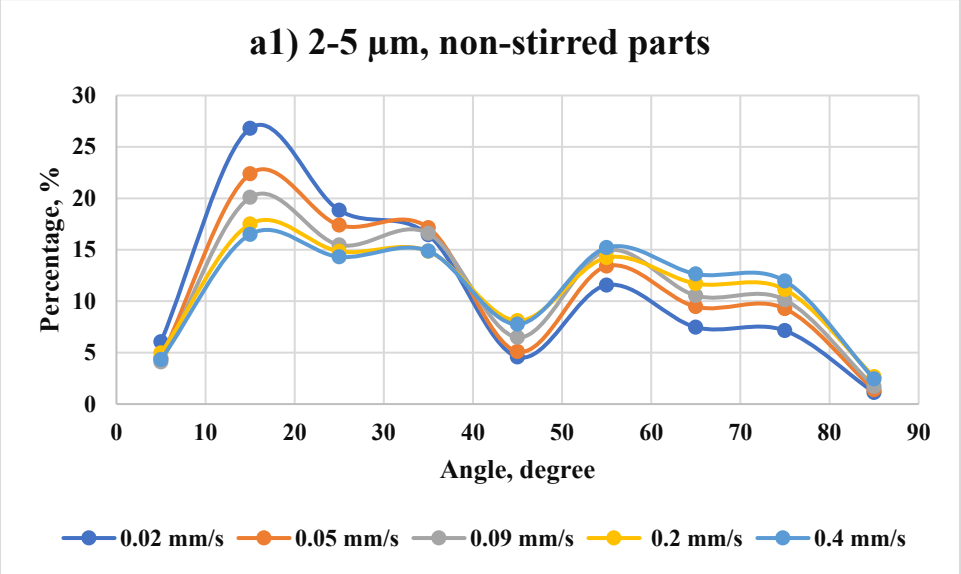

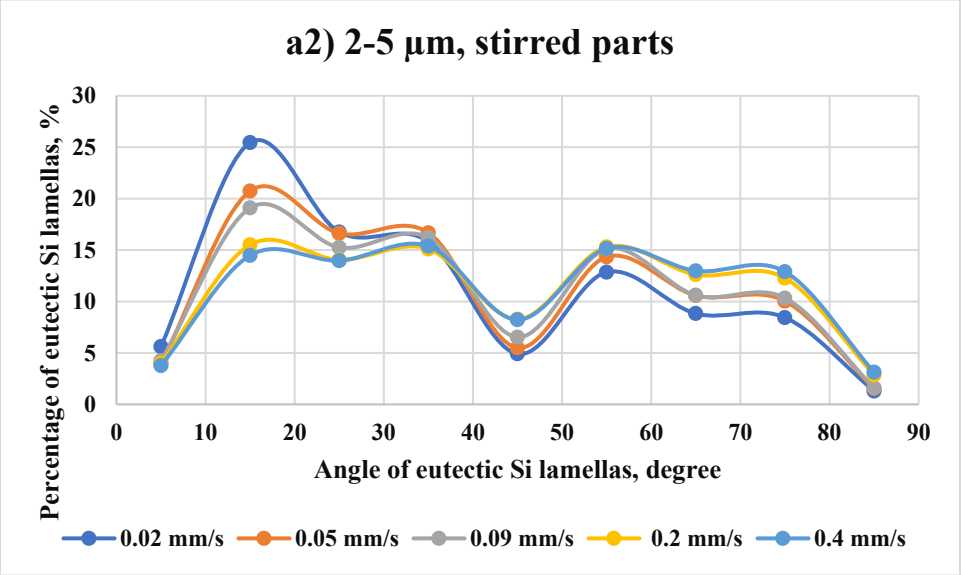

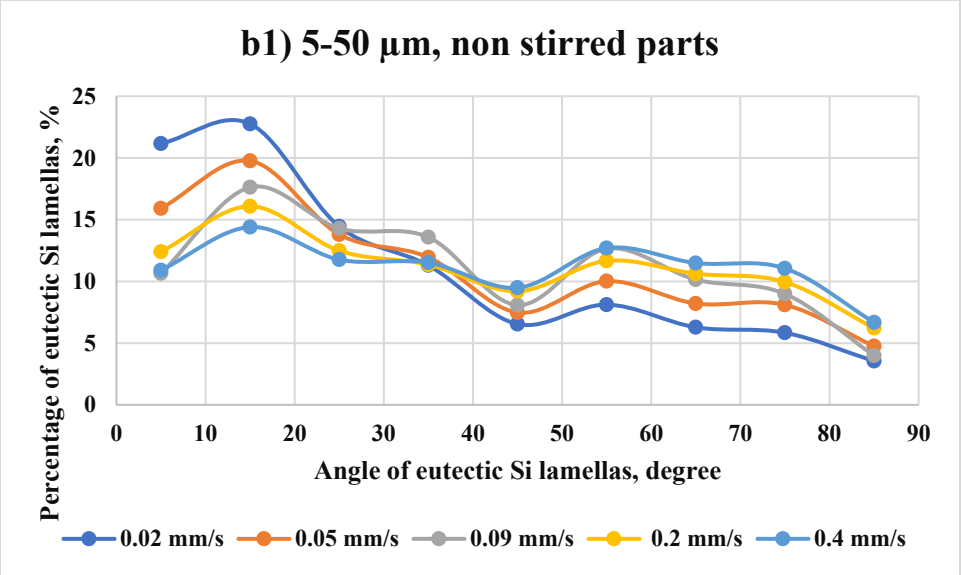
b1) 5-50 µm, non stirred parts
Percentage of eutectic Si lamellas, %
25
20
15
10
5
0
0
10
20
30
40
50
60
70
80
90
Angle of eutectic Si lamellas, degree
0.02 mm/s
0.05 mm/s
0.09 mm/s
0.2 mm/s
0.4 mm/s

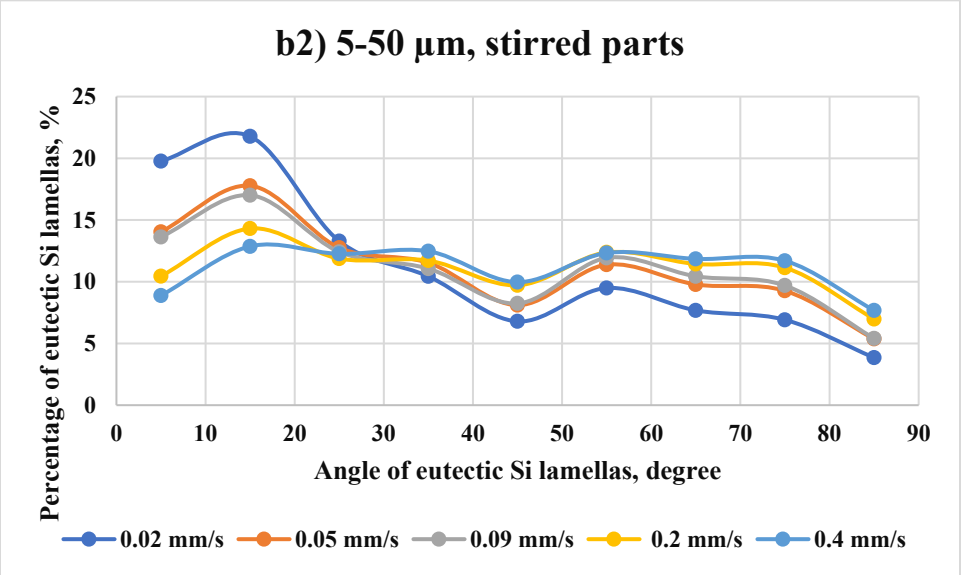
b2) 5-50 µm, stirred parts
Percentage of eutectic Si lamellas, %
25
20
15
10
5
0
0
10
20
30
40
50
60
70
80
90
Angle of eutectic Si lamellas, degree
0.02 mm/s
0.05 mm/s
0.09 mm/s
0.2 mm/s
0.4 mm/s

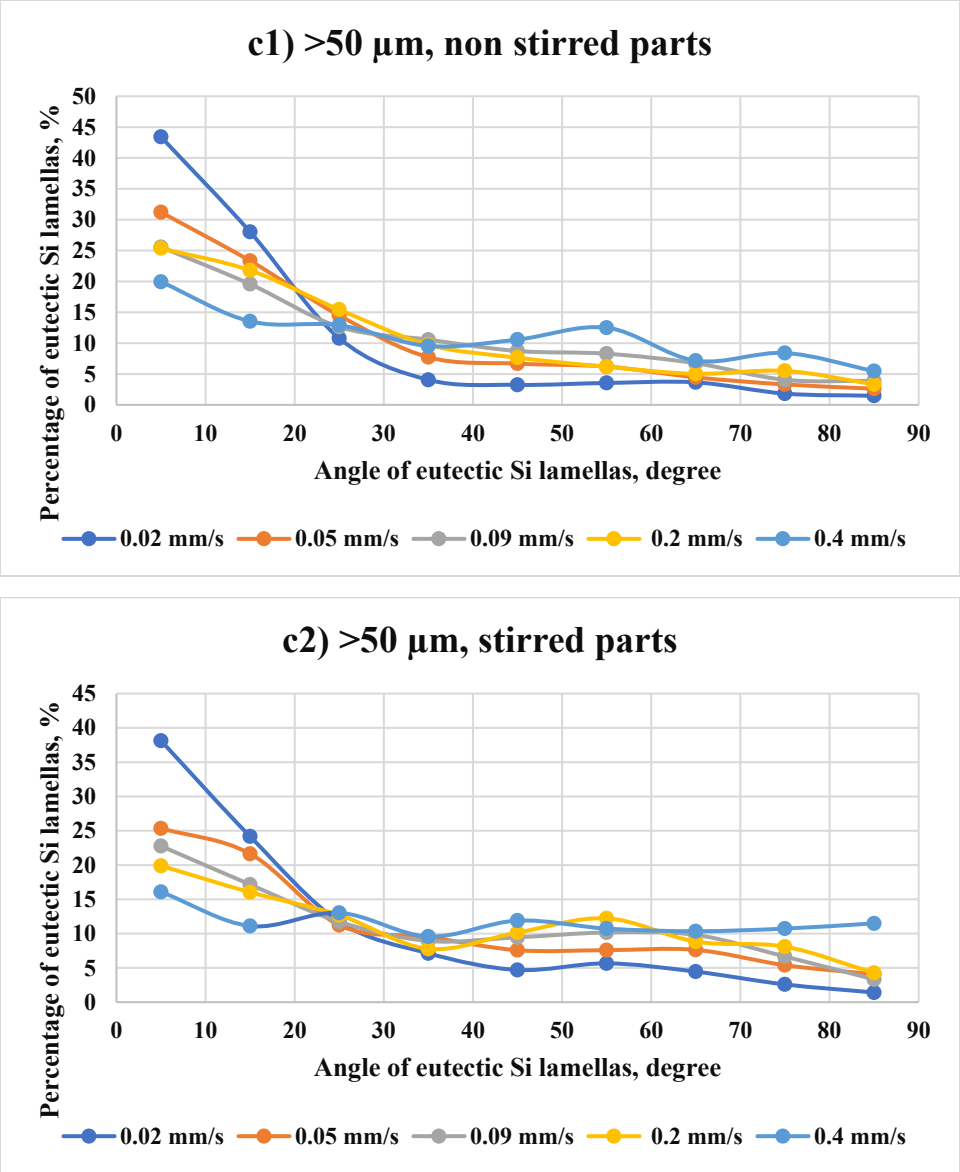

Figure 68. The angle distribution of eutectic Si lamellas at different eutectic front velocities for different length ranges, (a) 2-5 µm, (b) 5-50 µm, (c) >50 µm in stirred and non-stirred parts of the samples.

9.4. Size of primary Si particles

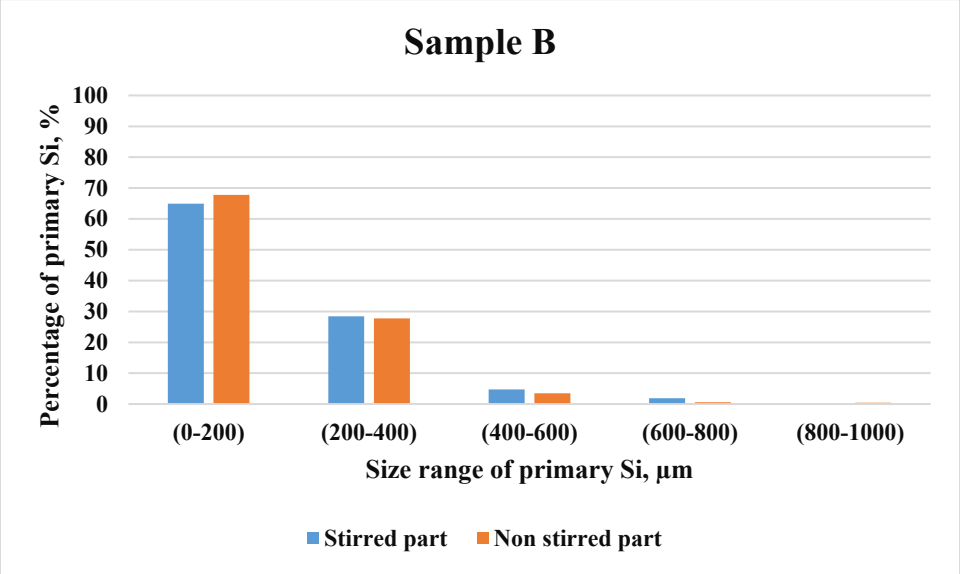

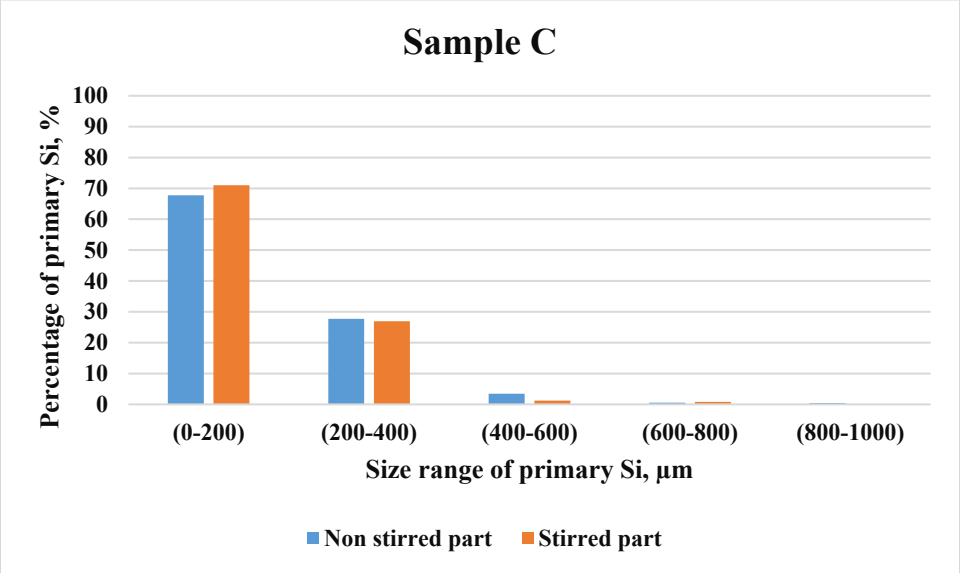

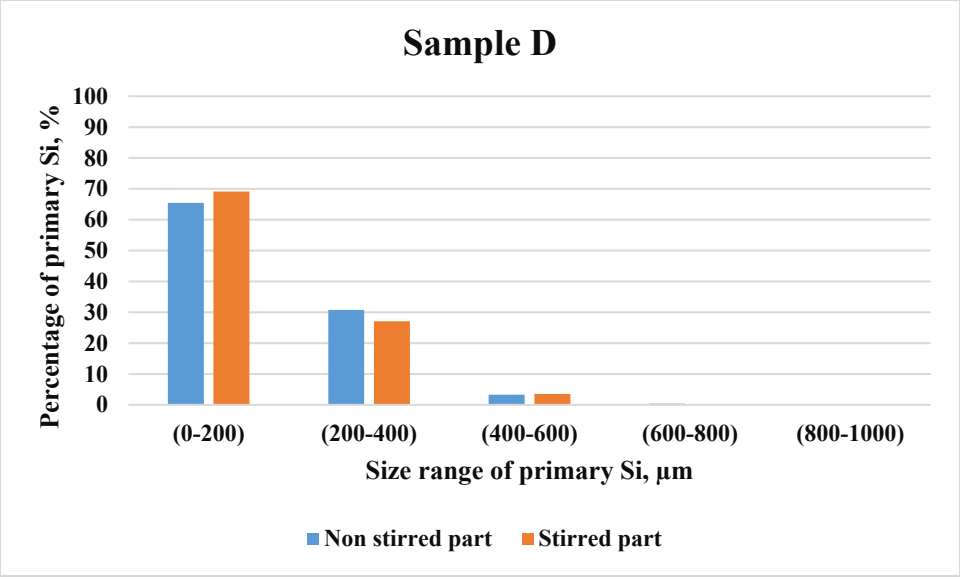

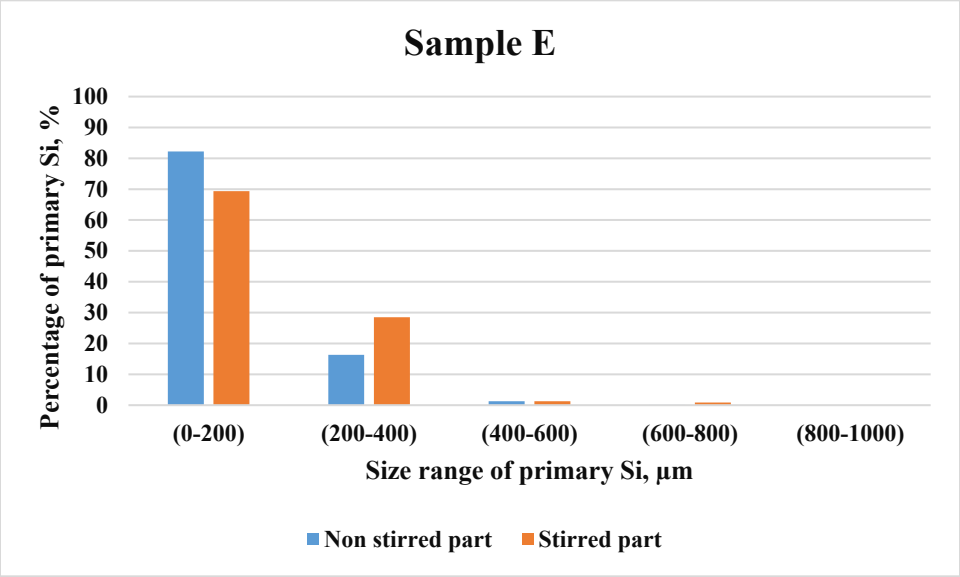

Figure 69. The percentage of primary Si as a function of their size range in the stirred and non-stirred parts of the samples B, C, D, and E.